Australian Government
Bureau of Meteorology

The Centre for Australian Weather and Climate Research
A partnership between CSIRO and the Bureau of Meteorology

CSIRO

Assessing the impact of climate change on extreme fire weather in southeast Australia

CAWCR Technical Report No. 007

A.E.A. Hasson, G.A. Mills, B. Timbal and K. Walsh

December 2008

www.cawcr.gov.au

Assessing the impact of climate change on extreme fire weather in southeast Australia

CAWCR Technical Report No. 007

A.E.A. Hasson[1], G.A. Mills[1,3], B. Timbal[1] and K. Walsh[2]

December 2008

[1] Centre for Australian Weather and Climate Research, Bureau of Meteorology, Melbourne GPO Box 1289, Melbourne Victoria 3001, Australia.

[2] School of Earth Sciences, University of Melbourne, Victoria 3010, Australia.

[3] Bushfire Cooperative Research Centre, Australia

PREFACE

This report comprises an edited version of the senior author's (AH) thesis submitted in support of a BSc (Honours) degree with the School of Earth Sciences at the University of Melbourne in November 2007.

Enquiries should be addressed to:

Dr Graham Mills
Bureau of Meteorology
GPO Box 1289K, Melbourne
Victoria 3001, Australia
g.mills@bom.gov.au

Phone: 61 3 9669 4582

ISSN: 1836-019X

ISBN: 978-1-921424-84-7

Series: Technical report (Centre for Australian Weather and Climate Research.) ; no. 7.
Also issued in print.

Copyright and Disclaimer

Contents

Abstract

Extreme fire weather events have major socio-economic impacts on the Australian population, and therefore trends in the frequency of such events in the future are of great interest to planning authorities. While traditional fire danger indices calculated from climate model projections can be used to estimate these trends, their approach does not adequately resolve the most extreme events usually leading to the greatest damage. Recently it was shown that many of the most extreme fire weather events over southeastern Australia during the last 40 years were associated with the passage of strong, deep cold fronts, and that these events could be identified in NCEP/NCAR reanalyses (NNR) using relatively simple diagnostics based on 850 hPa temperature and temperature gradient. The robustness of this relationship is demonstrated by applying it to an independent set of reanalyses, the ERA40 data, and comparing the results with those from the NNR. The diagnostic approach is then applied to the output of 10 models taken from the Coupled Model Intercomparison Project of the Intergovernmental Panel on Climate Change fourth Assessment Report. The uncertainty and reliability of the approach are examined for simulations of the twentieth century climate for each model as well as in the reanalyses. The model results for two contrasting emissions scenarios: low (SRES B1) and high (SRES A2) over two twenty-year periods centred on 2050 and 2090 are analysed. The models are evaluated against the reanalyses and ranked according to their ability to reproduce the reanalysis temperature distribution over southeast Australia during the 20th century. A marked increase in the occurrence of these unusual synoptic situations was found over the whole twenty-first century for both scenarios. However, the rate of change of the increase varies between the scenarios, and through the century. All the models, which were selected as better able to match the reanalyses for the 20th century, show an increase in the seasonal frequency of events to the middle of the 21st century for the B1 scenario, levelling out in the latter half of that century. The projections under the A2 emissions scenario show a greater increase by the middle of the 21st century, continuing until the end of it, although the spread between the different models is very high.

1) Introduction

Wildfires have shaped Australia's environment for millions of years. South-east Australia, along with Mediterranean Europe and California, is one of the most bushfire-prone regions in the world. Many severe fire events have marked the Australian memory during the last century, such as the Black Friday fires in 1939, the Tasmanian fires in 1967 (Bond et al. 1967), the Ash Wednesday fires in 1983 (Bureau of Meteorology 1984) and more recently, the Alpine fires in 2003 (Bureau of Meteorology 2003), the Black Tuesday fires in 2005 (Bureau of Meteorology 2005) and the fires in Victoria in December 2006-January 2007.

While all parts of the Australian continent can experience bushfires, the seasons of greatest risk vary according to the rainfall and temperature regimes; the north of the country experiences the highest fire danger in winter ("the dry"), and the high risk areas moving progressively south as the season advances into late summer (Fig. 1).

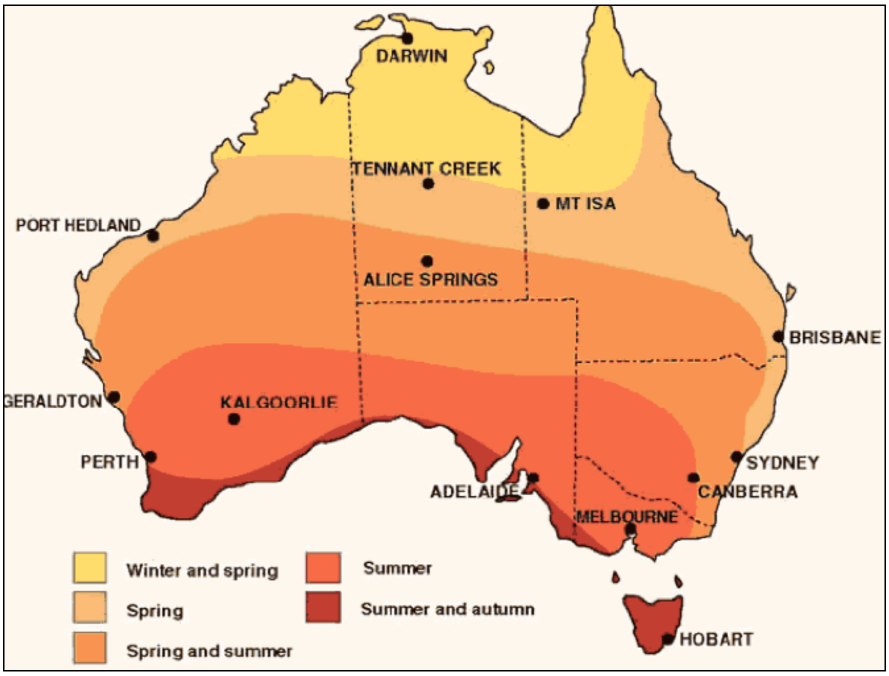

Figure 1: *Seasonal pattern of fire danger in Australia (as depicted in* ***www.bom.gov.au/climate/c20thc/fire.shtml***)

During the last century a general warming of about 0.8ºC has been observed in Australia, along with associated regional trends in rainfall (Hughes 2003), and these changes have also been simulated by the latest generation of coupled climate models (IPCC 2007 and Fig. 2). With the expectation that wildfire activity or frequency may be affected by changes in climate, there is considerable interest in assessing these possible changes into the future, as indicated in the fire weather reports by Hennessy et al (2005) and Lucas et al. (2007).

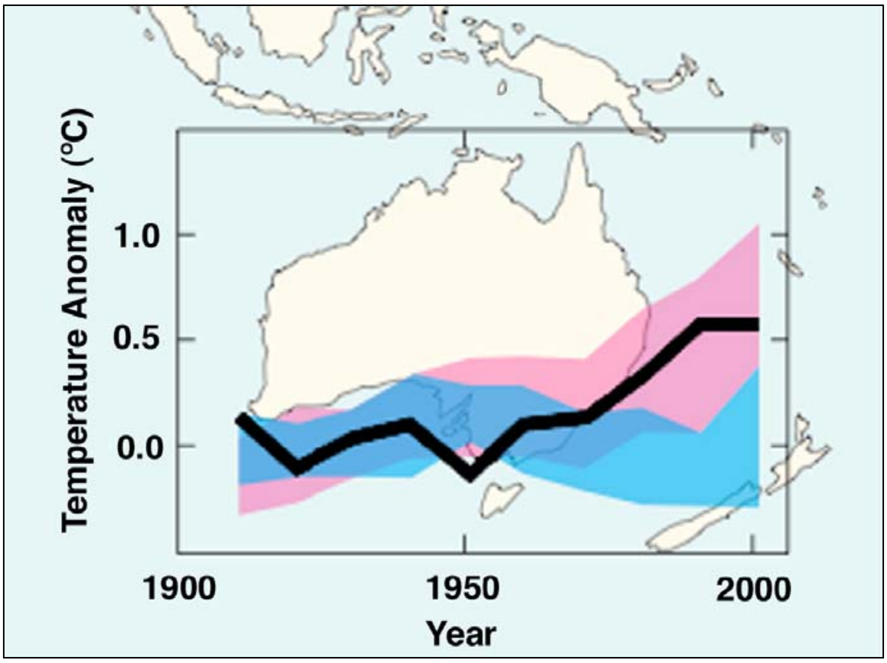

Figure 2: *Comparison of Australia-wide observed continental changes in surface temperature (black line) with results simulated by climate models using natural only (blue shaded band) and natural plus anthropogenic forcing (pink shaded band). Both shaded bands show the 5–95% range (from Fig. 4 from the Summary for Policymakers; IPCC 2007).*

Global climate models (GCM), though, are not well suited for the assessment of small-scale, rare events due to their limited spatial and temporal resolution; outputs are typically archived once a day and on a resolution of 200 to 300 km. Mills (2005) proposed a diagnostic based on 850 hPa temperature fields from the NCEP/NCAR reanalyses (hereafter NNR, Kalnay et al. 1996) associated with many of the most extreme fire events over southeastern Australia in the last 40 years. He suggested that a field such as 850 hPa temperature would be expected to be well forecast by medium-range global NWP models, and that prediction of such extreme fire weather events could be possible for several days into the future.

Taking this reasoning a stage further, it may be possible to apply a similar analysis to climate models, and thus calculate trends in the frequency of such extreme fire weather events under climate change scenarios. In this paper we address this issue. Mills' methodology is first evaluated for the late 20th century by comparing the results from NNR analyses with those from the ERA40 reanalysis data set (Kallberg et al. 2005). We then apply the methodology to 10 GCMs from the Couple Model Intercomparison Project (CMIP3) used in the recent Intergovernmental Panel on Climate Change 4th assessment (IPCC, 2007), by first evaluating their climate of the 20th century against the reanalysis climates. We then apply the techniques to two climate change scenarios to assess the possible changes in frequency of these synoptic environments over southeastern Australia in the middle and latter parts of the 21st century.

2) Fire weather background

a) Fire weather and fire danger indices

Fire Weather is not a term that has a precise definition. It is usually used to describe the weather that contributes to enhanced fire activity. Fire Danger Indices (FDI) has been developed to quantify the likely effects of weather on fire behaviour and difficulty of fire suppression for use in community and fire management planning.

Fire behaviour and spread is mainly influenced by three groups of parameters. The first one is the fuel characteristics, such as the vegetation density, the species of trees or grass, and the distribution of the vegetation and so on. The second one is the regional topography which can have great impact on fire behaviour. For instance, fire spreads approximately three times faster up slope than it does down slope (Xiao-Rui et al. 2005). The last but not least important group of parameters are the weather elements that contribute to fire activity, and it is this group of parameters that is addressed in this report.

Fire Weather is traditionally represented by five main meteorological variables: the temperature, the relative humidity, wind speed and direction, and antecedent precipitation. Depending on the particular functional form of the different fire danger indices, the data needed may vary in detail, but are usually derived from these variables.

There are three widely used Fire Danger Indices (Xiao-Rui et al. 2005). Perhaps the most widely used is the Canadian Forest Fire Danger Rating System (FFDRS; Stocks et al. 1989). It has been operational in Canada since 1971, and was adapted for use in other parts of the world, including New Zealand (Dudfield 2004), the south-eastern Asian nations (de Groot et al. 2005) and Portugal (Viegas et al. 1999). In the United States, the National Fire Danger Rating System (NFDRS; Deeming et al. 1977) has been used by different agencies since 1972. The NFDRS is based on laboratory-developed constants derived from the physics of combustion under different environmental forcing parameters. In Australia the Forest Fire

Danger Index (FFDI) (McArthur 1967) has been widely used in southern Australia since 1967, and modified to include a Drought Factor that takes into account antecedent rainfall, it is now called the Mk4 Forest Fire Danger Metre. Its constants were empirically based on observations from 800 experimental and wild fires. It "is based on the expected behaviour of fires burning for an extended period in dry eucalypt forests carrying a fine fuel load of 12.5 tonnes /ha and travelling over level to undulating topography" (Xiao-Rui et al. 2005). The original calculations of this index were made using a circular slide rule (Luke and McArthur 1978) and was adapted to a functional form by Noble et al. (1980) (displayed below).

$$FFDI = 2*\exp(0.987*\log D - 0.45 + 0.0338*T + 0.0234*V - 0.0345*H)$$

where:

T = air temperature (screen temperature) in degrees Celsius

V = mean wind-speed 10 metres above the ground, in meters per second, averaged over at least five minutes in open large area of above tree top in the case of a forest.

H = relative humidity from 0-100%, calculated from the screen temperature T.

D = drought factor in the range 0-10. (DF)

The drought factor (DF) is a broad measure of the fuel moisture, and includes a weighting of recent rainfalls and seasonal (long-term) precipitation. The Bureau of Meteorology uses the Griffith modification to the DF (Griffith 1999). These calculations are also described in Finkele et al. (2006).

While it was originally considered that a FFDI of 100 would indicate "the near worst-possible fire weather conditions that are likely to be experienced in Australia" (Luke and McArthur, 1978, P114), the equation is open-ended. Different thresholds of FFDI are used to define five levels of increasing fire danger: low, moderate, high, very high and extreme - in order to simplify its use by the public who are asked to modify their activities accordingly. There also exists a separate FDI specific to grassland - the McArthur Mark 4 Grassland Fire Danger Index (GFDI; Purton 1982). The GFDI includes the same input parameters as the FFDI above, but with a different functional form, and with the DF replaced by a curing factor which specifies “the proportion of cured and/or dead material in a grassland fuel complex” (Cheney and Sullivan 1997).

b) *Synoptic situations linked with extreme fire weather*

A number of studies have been undertaken to link the rare very high and extreme fire danger events to synoptic systems, rather than just to the simple FDI input variables, in order that meteorological agencies might to alert the fire services to the likelihood of those extreme conditions with greater confidence and lead-time.

Long (2006) investigated the synoptic patterns and wind directions linked to extreme fire weather days in Victoria and their frequencies. Her study used a period of 29-seasons from 1970 to 1999 and four observing stations in the Victorian region, and confirmed forecasting experience that in Victoria extreme fire danger occurs in strong and gusty pre-frontal north-westerly flow. This can be partly explained by the very dry and extremely hot air from central Australia being advected to the south-eastern part of the continent. Long also assessed the Haines Index (Haines 1988), developed in the United States of America, which provides a measure of the lower tropospheric instability and dryness. While it provides some correlation with extreme fire weather days, under mainland Australian conditions it does not provide strong discrimination of those days. This result was also found by McCaw et al. (2007).

A particular paradigm of extreme fire danger occurs in southern Australia when a cold front passing over the region induces a strong change of wind direction, which converts the flank of the fire into the leading edge, and therefore generates a larger area under fire risk (Fig. 3). The danger posed by this particular situation was stressed by Cheney et al. (2001).

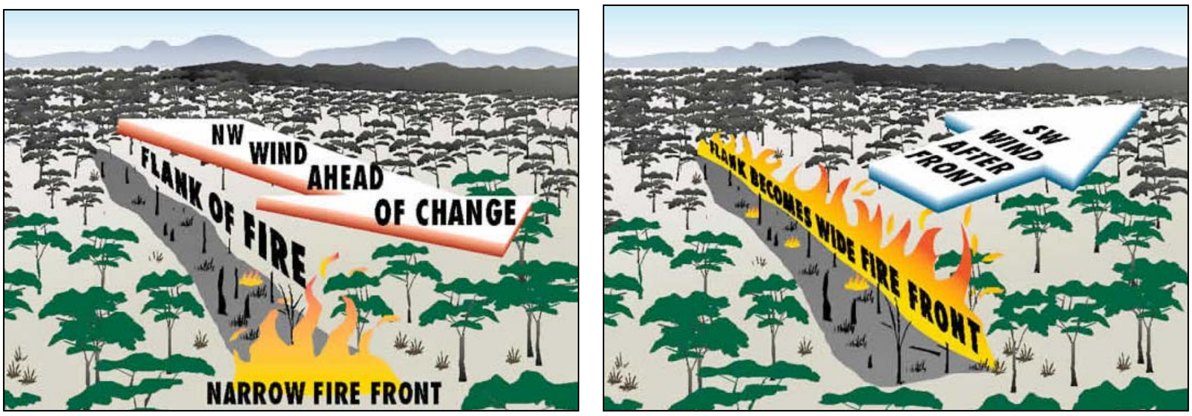

Figure 3: *Schematic effect of a wind direction change during a fire event (as depicted in* ***http://www.bom.gov.au/inside/services_policy/fire_ag/bushfire/anatomy.htm*** *).*

Similarly, Crimmins (2006) reported on the "synoptic climatology of extreme fire-weather across the southwest United States". He found that 80% of very high fire weather days studied was associated with strong westerly flow and deep fronts identified with large geopotential height gradients.

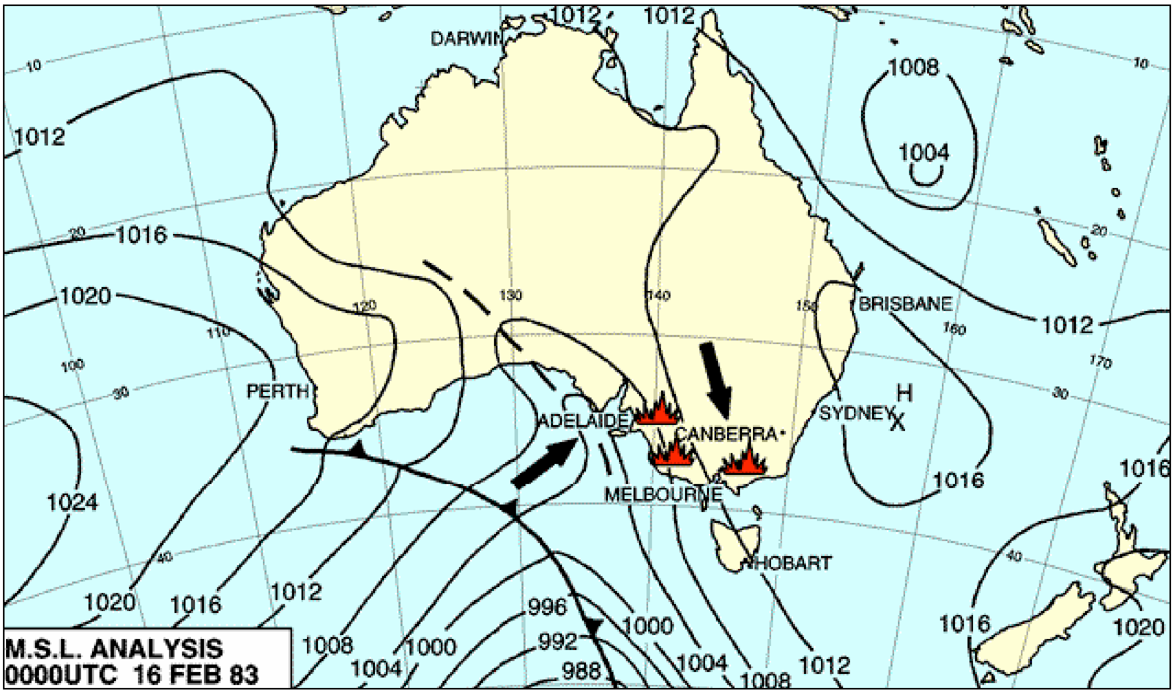

Figure 4: *Mean sea level pressure analysis of the 16th of February 1983 at 0000UTC (as depicted in* ***http://www.bom.gov.au/inside/services_policy/fire_ag/bushfire/highse.htm*** *)*

A study of the disastrous fires of Ash Wednesday 16 February 1983 (Bureau of Meteorology 1984) stated that this extreme event was exacerbated by a severe drought which affected south-eastern Australia that summer due to the on-going El Niño phase of the ENSO phenomenon, and also speculated on the role of the existing mobile upper trough and of the occurrence of a long episode of strong winds following the abrupt wind change along the southeast Australian coastline associated with the passage of a strong cold front (Fig. 4).

Mills (2005) reinvestigated the synoptic dynamics of the Ash Wednesday 1983 cold front, and noted that the strength and depth of the cold front contributed to the sustained period of strong winds that followed the front, producing the situation shown schematically in Fig. 3, and suggested that the existence during the event of a very strong thermal gradient (T_G) at the 850 hPa level may be an indicator of such a deep cold front. To assess the uniqueness of the wind structures and the associated cold front passing through Victoria on the 16th of February 1983, Mills (2005) used the Australian National Meteorological and Oceanographic Centre operational objective analyses from 1979-1993 (Seaman et al. 1977), and the NNR data over 40 summers from 1964 to calculate the magnitude of the 850 hPa temperature gradient ($|\nabla T_{850}|$, hereafter T_G) over a sub-area of southeastern Australia every 12 hours. It was argued in that study that using temperature data from the 850hPa level assured that such systems have a "sufficient depth of cool air to their west" to generate a strong post-frontal pressure gradient. Ordering these values of T_G by magnitude, and comparing the dates of the highest values with reported fire events showed that a large proportion of the most extreme fire events over southeastern Australia occurred on the days in which T_G was in the upper 0.05% of its distribution. It was also shown that there appears to be some relation between the orientation of the isotherms and these extreme fire events, with more meridionaly oriented isotherms leading to strong northerly prefrontal winds as observed during the Ash Wednesday fire event. As this situation is also one in which the maximum temperature in the sub-area is also high, Mills (2005) proposed that a phase space in which both high temperatures and high T_G at 850 hPa are both satisfied may indicate the potential for an extreme fire weather event over southeastern Australia, as shown in Fig. 5.

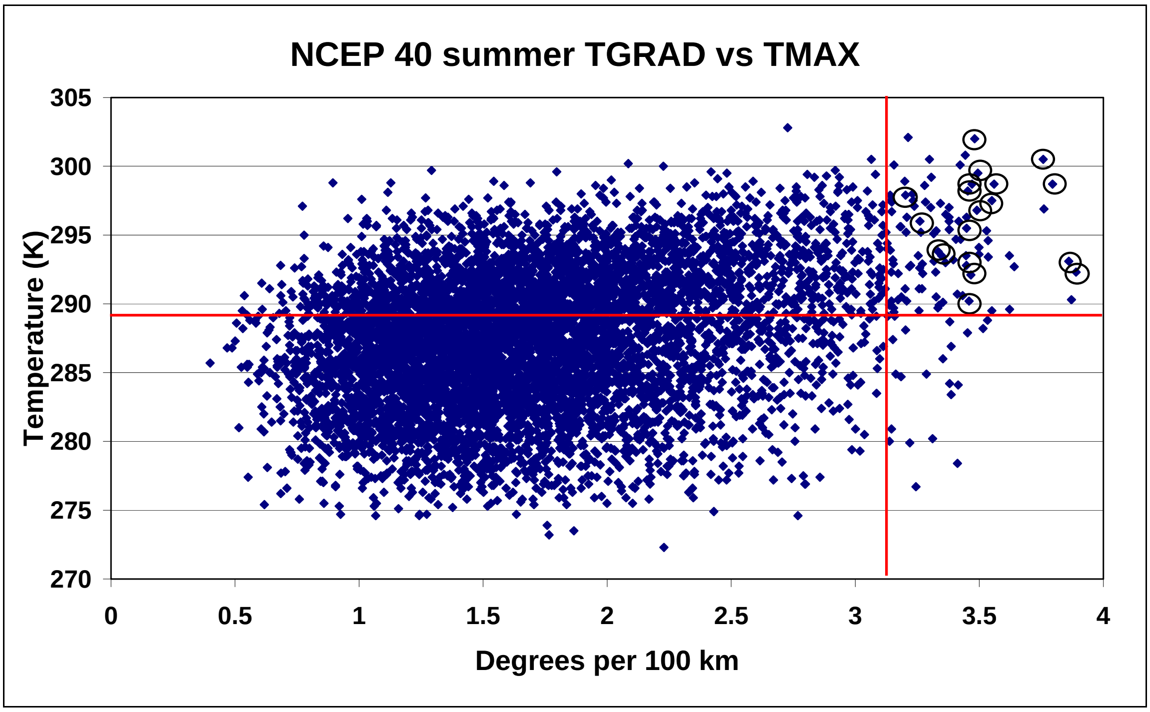

Figure 5: *Scatter-plot of 850hPa T_G versus the maximum temperature at 37.5ºS over the region and period examined by Mills (2005). Red lines show a suggested minimum T_G and temperature thresholds associated with extreme fire danger. The circles indicate the fire events listed in Mills' paper; adapted from Mills (2005).*

Mills (2005) surmised that the orientation and depth of the thermal gradient coupled with temperature could provide a diagnostic tool for the forecast of extreme fire danger days, particularly as these fields are expected to be well predicted by operational medium and short-range Numerical Weather Prediction (NWP) models. This could potentially provide greater lead-time to the fire fighting agencies of unusually extreme fire weather. In the context of the current report, it also poses the intriguing question of whether this technique applied to climate change model projections might show changes in the frequency of such events in the future.

3) Climate change background

In 1988 the World Meteorological Organisation (WMO) and the United Nations Environment Program (UNEP) created the Intergovernmental Panel on Climate Change (IPCC) to study "the scientific, technical and socio-economic information relevant for the understanding of climate change, its potential impacts and options for adaptation and mitigation" (IPCC, 2007). However, long before the IPCC delivered its first report in 1990; signs of climate change and its link with greenhouse gases such as carbon dioxide were diagnosed. As early as 1970, the first reliable three-dimensional climate model simulated an increase of more than 2 degrees Celsius if the concentration of carbon dioxide was doubled from pre-industrial concentrations (Manabe and Wetherald 1970).

The IPCC has released four assessment reports since its creation - in 1990, 1995, 2001 and 2007. The first report triggered international concern on the possible effect of climate change and resulted in the signing of the international treaty called the "United Nations Framework Convention on Climate Change" in 1992 during the Rio de Janeiro "Earth Summit". The major update of this treaty is the Kyoto Protocol of 1997. The later reports of the IPCC consist of three sections written by three working groups focusing separately on the "physical science basis", the "impact, adaptation and vulnerability" and the "mitigation of climate change" issues.

We used for this project some of the model simulations and scenarios used by the first working group for the 2007 IPCC assessment report (IPCC-AR4) and available as part of the CMIP3 data set. Those models and scenarios will be presented in the following sections.

a) Models

Coupled GCMs are based on the physical principles that govern the Earth's atmosphere and ocean, including Newton's laws of motion and laws of fluid dynamics and thermodynamics. These equations are then approximated and mathematically discretized. The main constraint on the increase of accuracy in the approximations made to create the models is computational capacity. As the power of computers increases, there is no general consensus on the way to improve the models' output precision (Randall et al. 2007). Three complementary ways of increasing confidence in or accuracy of the model projections are used: increase the number of independent models to increase the statistical confidence, increase the spatial and temporal resolutions of the models in order to simulate smaller but not less important features, and incorporate more physical processes that thus better represent more of the feedback mechanisms in the earth-atmosphere system. We had available to us for this study 10 Atmosphere-Ocean General Circulation Models (AOGCMs), listed in Table 1. All have relatively coarse resolution compared to contemporary NWP models, but represent at the time of the IPCC-AR4 report the capability of contemporary global climate change models.

Acronym	Nation	Resolution
CCM	Canada	3.8º x 3.8º
CNRM	France	2.8º x 2.8º
CSIRO	Australia	1.9º x 1.9º
GFDL1	U.S.A.	2.5º x 2.0º
GFDL2	U.S.A.	2.5º x 2.0º
GISSR	U.S.A.	5.0º x 4.0º
IPSL	France	3.7º x 2.5º
MIROC	Japan	2.8º x 2.8º
MPI	Germany	1.9º x 1.9º
MRI	Japan	2.8º x 2.8º

Table 1: *List of the acronyms used for IPCC-AR4 coupled models, the nation where they were developed and their resolution.*

Before using the model projections into the future to assess possible climate change, each model is used to simulate the climate of the twentieth century and compared to reanalysis sets to evaluate their ability to reproduce the past and present climate. Any conclusions drawn based on the forecast climate can then be predicated on the performance of the model in simulating the recent past climate. Figure 6 shows the surface temperature anomaly calculated by the models over the last century up to now, featuring the observed values and models mean, as well as the four main volcanic eruptions: the models reproduce the broad characteristics of the temperature trends during the twentieth century reasonably well.

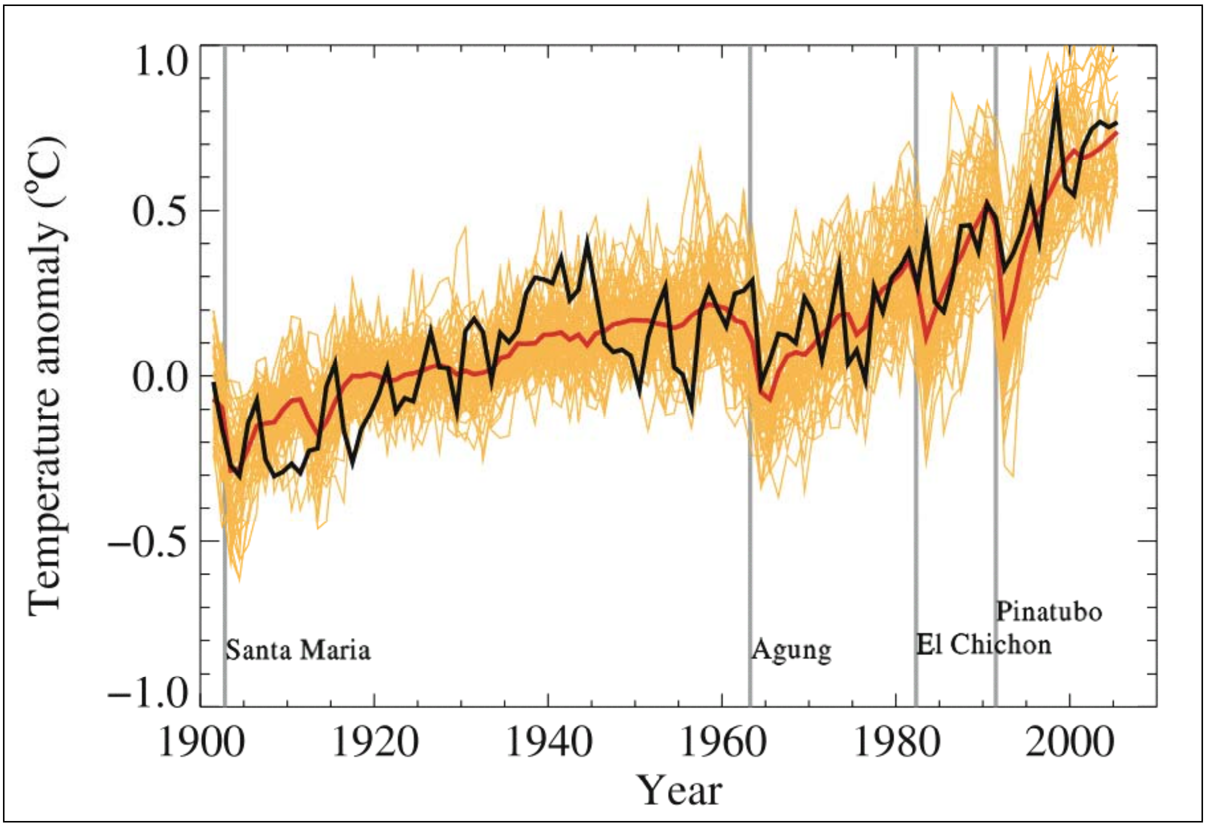

Figure 6: *Global mean near-surface temperatures over the 20th century from observations (black) and as obtained from 58 simulations produced by 14 different climate models driven by both natural and human-caused factors that influence climate (yellow). The mean of all these runs is also shown (thick red line). Temperature anomalies are shown relative to the 1901 to 1950 mean. Vertical grey lines indicate the timing of major volcanic eruption (from Randall et al, 2007).*

The IPCC-AR4 assessed the uncertainties in the projections and classified them in two main categories. The behavioural uncertainty includes the possible errors in projected gas and aerosol concentrations due to unknowns in the evolution of socio-economic behaviour. The scientific uncertainty comprises the possible output errors in the models. Both uncertainties increase with time (Hennessy et al, 2005). The previous IPCC assessment (IPCC, 2001) noted that the previous generation of GCMS used to project the global climate changes over the next century poorly forecast extreme events. However in the most recent assessment (IPCC, 2007), the evaluation of extreme events simulations of the coupled models in the current climate revealed an interesting improvement: the state of the art coupled models are able to reproduce surprisingly well the statistics of extreme temperatures of the twentieth century (Randall et al., 2007).

b) Scenarios

The IPCC provides in the Special Report on Emissions Scenarios four broadly different 'storylines' on the evolution of the current society (Table 2). These are based on demographic, economic and technological driving forces (Nakiceňovic et al., 2000), without any probability assigned to any of these factors. Because long term prediction of emissions cannot be made with any accuracy, the climate models are integrated using various possible scenarios of future emissions. These varied emissions scenarios are based on the likely modifications of the sources and sinks of greenhouse gases, taking into account changes in direct anthropogenic emissions as well as in indirect emissions such as land use modifications. The emissions scenarios are the conversion of narratives of the evolution of our society into quantitative data that can be input to climate models.

Storyline A1 describes a world with "increased cultural and social interactions, with a substantial reduction in regional differences in per capita income" (Nakiceňovic et al. 2000) and A2 describes a heterogeneous world. Storylines B1 and B2 correspond to A1 and A2, but with enhanced solutions for economic, social and environmental sustainability. In order to get the broadest picture of the climate changes due to possible changes in emissions during the twenty-first century, we selected for this study the scenarios from storylines A2 and B1, corresponding to a high emission and a low emission scenario.

Storyline A1:

- Population peaks at 2050 and declines afterwards
- Very rapid economic growth
- Rapid introduction of new and more efficient technologies
- There exist three sub-groups:
  - Fossil fuel intensive (A1F1)
  - Alternative energy supply (Non-fossil fuel) (A1T)
  - Balanced use of all available energy sources (A1B)

Storyline A2:

- Homogenous across different region, steady increase in population
- Slowest economical growth and technology evolution of all storylines

Storyline B1:

- Population peaks at 2050 and declines afterwards (same as A1)
- Enhanced global solutions to economic, social and environmental sustainability.
- Introduction of clean and more efficient technologies

Storyline B2:

- Slowest increase of population of all storylines
- Intermediate economic development
- Enhanced local solutions to economic, social and environmental sustainability.

Table 2: *Emissions scenarios of selected socioeconomic storylines used in some of the IPCC model climate projections for the 21st century (Nakiceňovic et al. 2000).*

c) IPCC-AR4 projections

Emission scenarios based on the storylines described in the previous section were used as input to an extensive range of climate models used in the IPCC-AR4. Each model used the projected evolution of greenhouse gas concentration and of other gases and aerosols. Based on these climate model integrations, estimates of the likely range of sea-level rises and temperature increases through the 21st century (Table 3 and Fig. 7) have been made (IPCC, 2007). A global-average warming of 0.7 to 2.5ºC by the year 2050 and 1.4 to 5.8ºC by the end of the twenty-first century is estimated.

Moreover, in the IPCC-AR4 it was emphasised that the spatial distribution of the warming is not homogenous around the globe. The projections show a greater warming near the pole and over the land (Fig. 8).

Case	Temperature Change (°C at 2090-2099 relative to 1980-1999) [a] Best estimate	*Likely* range	Sea Level Rise (m at 2090-2099 relative to 1980-1999) Model-based range excluding future rapid dynamical changes in ice flow
Constant Year 2000 concentrations [b]	0.6	0.3 – 0.9	NA
B1 scenario	1.8	1.1 – 2.9	0.18 – 0.38
A2 scenario	3.4	2.0 – 5.4	0.23 – 0.51

Table notes:

[a] These estimates are assessed from a hierarchy of models that encompass a simple climate model, several Earth Models Intermediate Complexity (EMICs), and a large number of Atmosphere-Ocean Global Circulaion Models (AOGCMs).

[b] Year 2000 constant composition is derived from AOGCMs only.

Table 3: *Projected globally averaged surface warming and sea level rise at the end of the 21st century (from the IPCC 2007).*

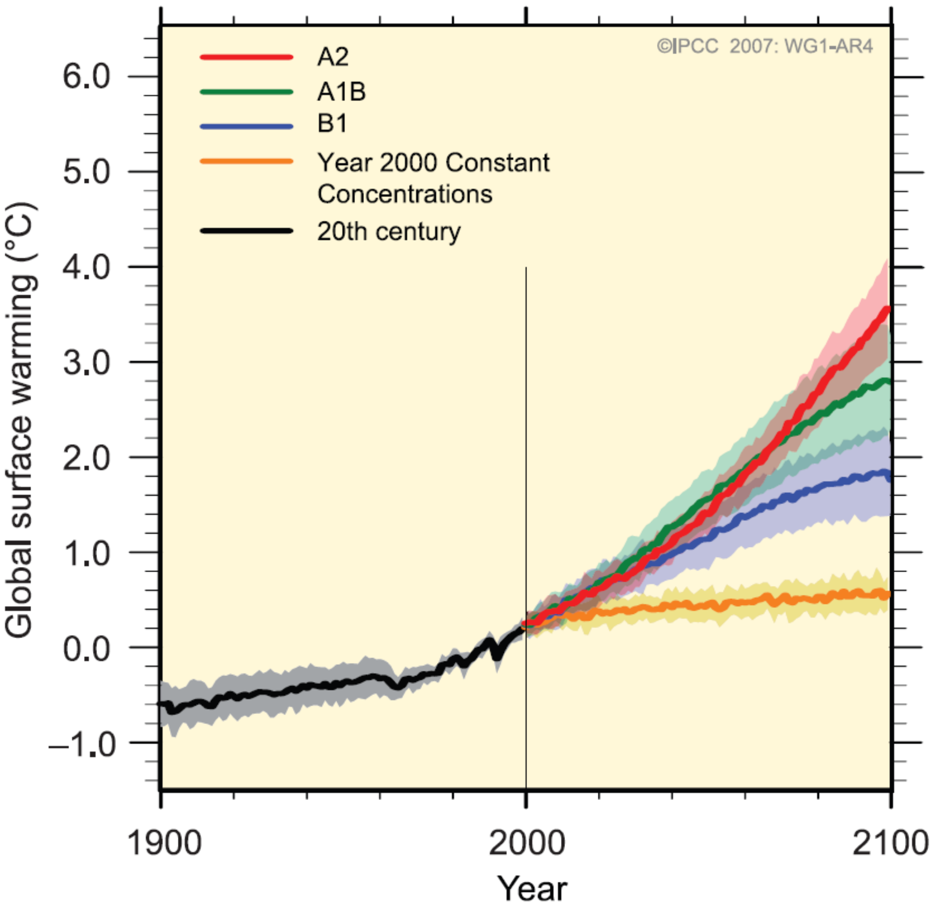

Figure 7: *Multi-model global averages of surface warming relative to 1980-99 (solid lines). Shading denotes the plus/minus one standard deviation range of individual model annual averages (from the IPCC 2007).*

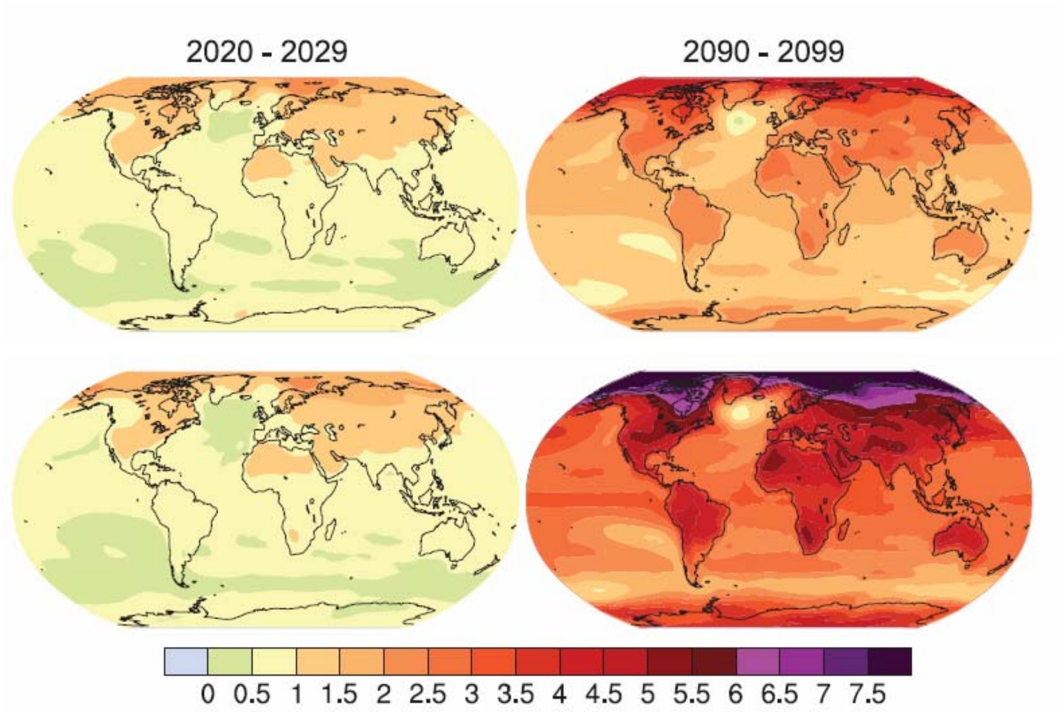

Figure 8: *Projected surface temperature changes in degrees Celsius for 2020-2029 (left) and 2090-2099 (right) relative to 1980-1999 from coupled Atmosphere-Ocean GCMs multi-Model average projections for the B1 (top) and A2 (bottom) SRES scenarios (from the IPCC, 2007).*

Other studies have been made to assess future temperature rise over the Australian continent. The result of one of them, conducted by the Australian Bureau of Meteorology and the Australian Commonwealth Scientific and Research Organization (CSIRO) (CSIRO and Bureau of Meteorology 2007) is shown in Fig. 9 for the B1, A1B and A1FI scenarios. The climate response under the A2 scenario is similar to that of A1Fl for 2070. A warming of more than 2ºC is predicted over the whole continent towards the end of the twenty-first century for the A2 scenario and between 1 and 2.5ºC for the B1 scenario.

While fire danger is often associated with high temperatures, it is also strongly influenced by changes in precipitation. The modelled future precipitation over Australia shows a 10 to 20% decrease over the south and southwest of the continent, notably during the austral winter months when most of precipitation occurs in those regions (Fig. 10 from the IPCC, 2007).

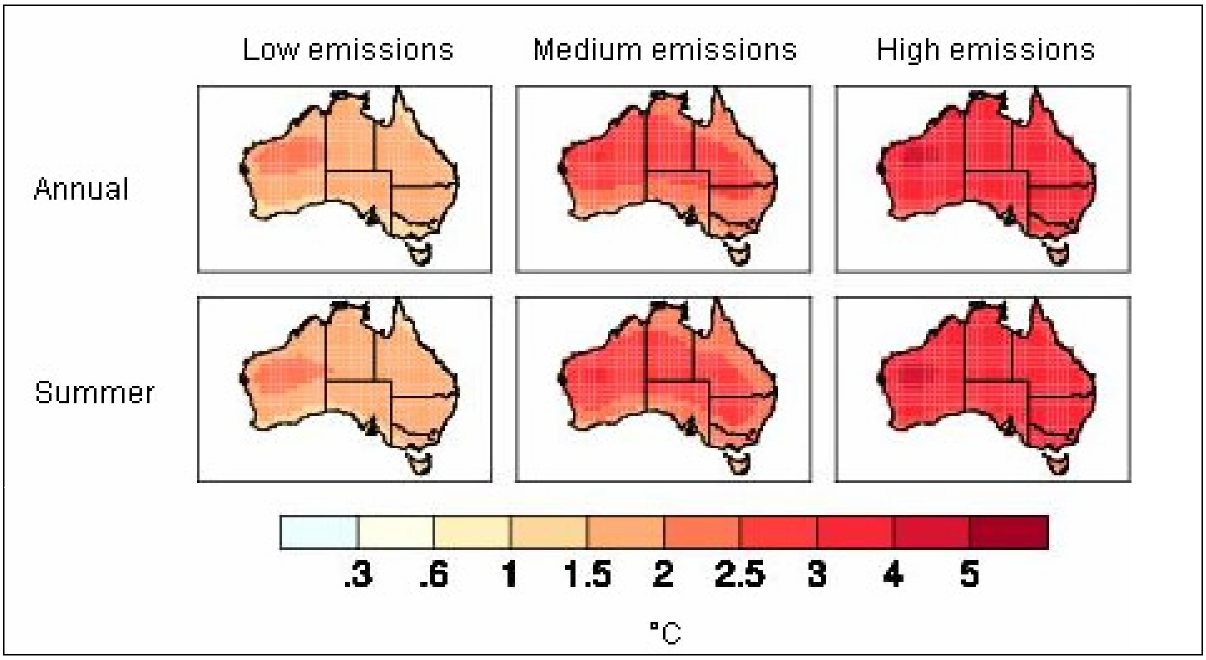

Figure 9: *Projections of temperature anomalies relative to the period 1980-1999. 50% percentile (best estimate) of the average annual and spring climate around 2070, for low, medium and high emissions corresponding to respectively the B1, A1B and A1FI SRES scenarios. (from the CSIRO and Bureau of Meteorology 2007).*

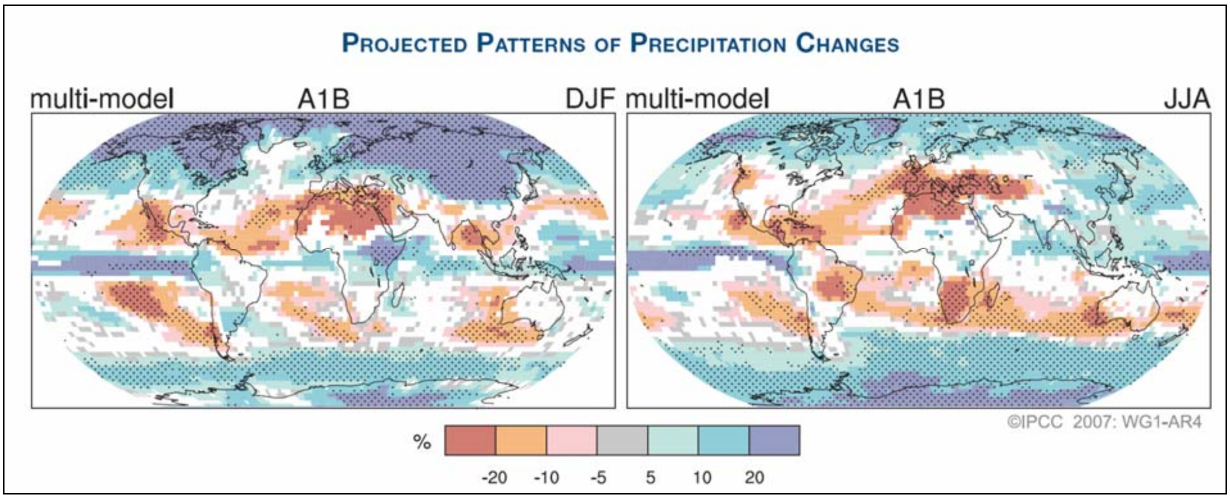

Figure 10: *Relative changes in precipitation (in percent) for the period 2090-2099, relative to 1980-1999. Values are multi-model averages based on the SRES A1B scenario for December to February (left) and June to August (right) (from the IPCC 2007).*

4) Projections of extreme fire weather under climate change

With the climate model projections indicating a warming climate, the IPCC is warning of potential increases in the intensity of extreme events such as bushfires, tropical cyclones, and droughts (IPCC, 2007). Therefore, it is imperative to be able to assess the evolution of the risk linked to the occurrence of bushfires, and in particular the potentially most disastrous events. A number of studies have used assessments based on changes in mean, median, or seasonal accumulated fire danger indices, and some of these are reviewed below. Few of these have attempted to study the extrema of the climate change data, and the application of the Mills phase space diagnostic to climate model projections is a potentially useful contribution to this on-going research. This will be described in the latter part of this section.

a) Projections using FFDIs

A recent study led by Tymstra et al. (2005) investigated the impact of climate change on the FDI in boreal forests of Alberta, eastern Canada. They used the Canadian Regional Climate Model (CRCM; Caya et al. 1995) with a 45 km by 45 km grid spacing, considered a "current time" period (1975-1985) and two future time periods, 2040-2049 and 2080-2089 respectively, and assessed the relative differences in temperature, relative humidity, wind speed, fine fuel and upper soil moisture, and long-term drought between the time periods. They showed that doubled and tripled carbon dioxide concentration scenarios induced a relative increase in burned area size of 12.9% and 29.4% respectively with respect to the constant carbon dioxide concentration control run. Tymstra et al. (2005) did not account for (but acknowledged) uncertainties in these conclusions based not only on uncertainties in the accuracy of the projections, but also to possible changes in fuel type, in diurnal humidity patterns, in precipitation and the increases in cloud to ground lightning strikes due to an increase in temperature.

Williams et al. (2001) investigated “the sensitivity of Australian fire danger to climate change” under the scenario of doubling the carbon dioxide atmospheric concentrations by the year 2100. They used the previous generation CSIRO 9-level GCM (Watterson et al. 1995) with an initial carbon dioxide concentration of 330 ppm (corresponding to the 1975 concentration) to assess the scenario impacts on the McArthur FFDI. They found that a doubling of the carbon dioxide concentration had a considerable impact on most of the traditional FDI variables apart from the wind speed. They diagnosed an increase in maximum temperature, a decrease in relative humidity and an increase in rainfall in southern Australia, although they indicated some reservations about the modelled rainfall projections. However, they considered that the FDI are most sensitive to changes in maximum temperature, and concluded that the length of the fire season seemed to be stable but with the high fire danger period occurring earlier. The fire season appeared to be more severe in the doubled carbon dioxide concentration scenario.

Hennessy et al. (2005) and Lucas et al. (2007) have assessed the impact of climate change on fire weather in south-east Australia. The fire weather variables used in this study were the daily maximum temperature, precipitation, 3pm relative humidity and wind-speed. They looked at the relative change in FFDI and GFDI by 2020 and 2050 with respect to the “present” conditions. The choice of models used in this study was limited by a number of factors: excellence of performance over southeast Australia, high resolution, and also the correspondence of the output to the traditional fire weather variables. Out of the twenty available models, two were selected: CCAM Mark2 and CCAM Mark3 (McGregor and Dix 2001). The scenarios chosen to force these models were the two most different ones, leading to high and low global warming projections (Nakiceňovic et al. 2000) and capture most of the emission uncertainties. The models were run for the 1962-2003 period, but only the relative variation in the FFDI and GFDI by the years 2020 and 2050 were examined. They used three statistics to illustrate the evolution of the two indices: the annual-average cumulative indices, the monthly-average indices and the daily-average indices. Monthly average FFDI results showed a higher fire danger in spring, summer and autumn, and an increase in length of the fire season. The main outcome of their study is a significant increase in the frequency of Very High and Extreme fire danger days by the end of the 21st century (Table 4).

Hennessy et al. (2005) listed areas where further research would be significant. This included the uncertainty in the humidity and wind speed, the limited number of only two models, the modelling scale being too coarse to take account of the fine topography and vegetation variations, and the assumption of non-evolution of the vegetation during climate change. Implicit in their downscaling technique was that the probability density functions for the individual ingredients (temperature, relative humidity etc) would not change in the future.

	2020		2050	
CCAM	Mark2	Mark3	Mark2	Mark3
Annual-average cumulative FFDI	2-10%	3-10%	5-25%	8-30%
Daily-average Very-High / Extreme FFDI	4-20%	6-25%	15-55%	20-70%

Table 4: *Increase in Annual and Daily-average FFDI as a function of the temperature increases (from Hennessy et al. 2005, Table 4).*

b) Projections using the Mills method

While the analysis of the evolution of fire danger due to the impact of climate change through the use of indices is limited by the coarse temporal and spatial resolutions of the output of the models used, it does have considerable value in assessing likely changes in seasonal characteristics. However, these techniques are not particularly well suited to assessing the changes in frequency of extreme events. Applying the 850 hPa T_G/T_{max} analysis proposed by Mills (2005) to future climate scenarios from the IPCC model projections provides one potential mode of assessment, as changes in the frequency of synoptic events clustered in the upper-right part of the phase space in Fig. 5 may be considered an indicator of changes in the number of this type of extreme fire weather events.

Mills (2005) method relies on only two parameters: the highest temperature (T_{max}) along the line of 37.5 S and the maximum 850 hPa thermal gradient (T_G), over a southeast Australia region defined as [137.5-150E] [35-40S]. This will be termed the Victorian Box (VB) hereafter, and is shown in Fig. 11. The two parameters are calculated from a single temperature field at the 850 hPa level. This level was chosen, as stated earlier, to ensure the selection of deep systems only. Consequently, this new diagnostic does not require a wide range of variables and can directly be applied to climate model output.

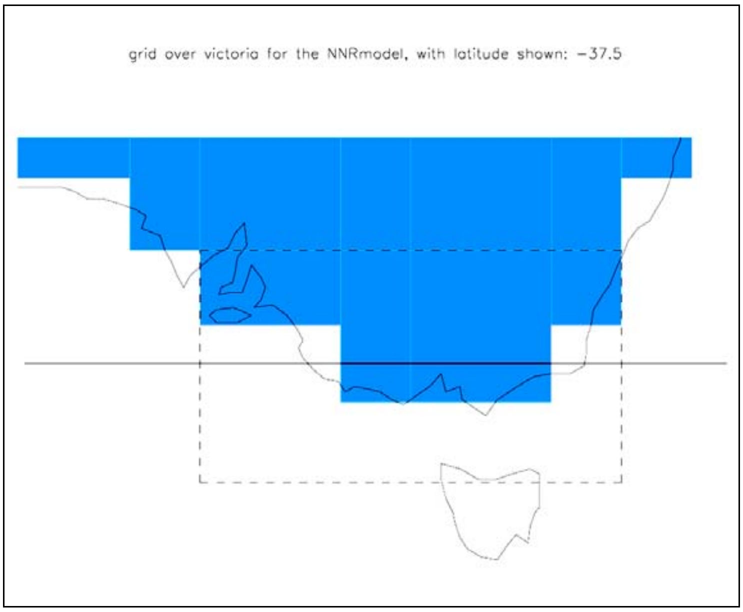

Figure 11: *NCEP/NCAR reanalysis (2.5˚x2.5˚ resolution) land-sea mask of southeast Australia, with the original Victorian Box (dashed line) and the 37.5S latitude line (solid line).*

There are a number of barriers with regard to applying this diagnostic technique to climate change models that first need to be addressed. First, the diagnostic has only been applied using the NNR data (although a shorter period using the Australian METANAL data set showed some consistency with the NNR data). Second, the climate model output was only available to us at 0000 UTC, while Mills used both 0000 and 1200 UTC NNR analyses, with the premise that it was highly likely that any front passing through the VB would be captured at one of those times. However, with 24-hour time interval, this assumption is likely to be violated. In addition, Mills speculated that the particular configuration of the southeast Australian coastline may make this approach only valid for this area, and so some relation of the bounds of the VB to the model's land-sea mask may be implicit in the definition of the VB. The box shown in Fig. 11 is based on the NNR 2.5° grid. However, because of the different resolution and respective land sea mask amongst the climate models, it makes the use of the same “VB” for all models impossible, and some care has to be taken to select an appropriate box and latitude for each model.

Before moving to make assessments of the likely changes in frequency of these strong frontal synoptic types in the future climate scenarios, we will examine each of the points in the preceding paragraph in turn.

5) Comparison of NNR and ERA40 diagnostics

Mills' (2005) comparison of his T_G/T_{max} phase space with known fires only addressed the 30 most intense T_G events in his data set, based on 0000 and 1200 UTC NNR analyses. Those results are indicative of an association of the top-right region of his scatter plot (reproduced in this report as Fig. 5) and extreme fire events. In this section we first repeat that analysis for both the NNR and the ERA40 reanalysis data sets (Kallberg et al. 2005), include additional fire events not included in the Mills data set, and restrict our analysis to the period 1 January 1964 to 28 February 2002 so that a common period is used for both sets of reanalyses. This period precludes using the fire events in 2003 (see Tables 1 and 2 of Mills 2005) but the addition of the other days means that some 20, rather than 13, events can be matched with the analyses. These events are listed in Table 5.

Since NNR and ERA40 output datasets have the same spatial resolution, identical VB sub-boxes over southeast Australia can be used to calculate T_G and T_{max}. Figure 12 shows the T_G vs. T_{max} scatter plots for both the NNR and the ERA40 data sets with both 1200 and 0000 UTC analyses included, and with the event dates shown in Table 6 highlighted. For NNR, the events cluster strongly in the top right-hand sector of the distribution, as seen in the earlier study, while there is some greater degree of scatter of the events in the ERA40 data set, although there is a strong bias to higher temperatures, and still an indication of enhanced event frequency towards the stronger gradients.

The IPCC climate model datasets available for our later analysis of the 21st century simulations were only available at 24-hour intervals, centred at 0000 UTC. The 0000 UTC analogue of Fig. 12 is shown in Fig. 13. This analysis shows a considerably greater scatter of the event data, but as the dates are for the calendar day on which the fire event was noted to have occurred, and with the normal diurnal variation of fire activity peaking in the afternoon, this result is perhaps to be expected. Sampling may also contribute to this result, as the eastward movement of a frontal system may well mean that with one sample per day the major thermal gradient may not lie within the VB at 0000 UTC, particularly as land-sea thermal gradients will also be stronger later in the day.

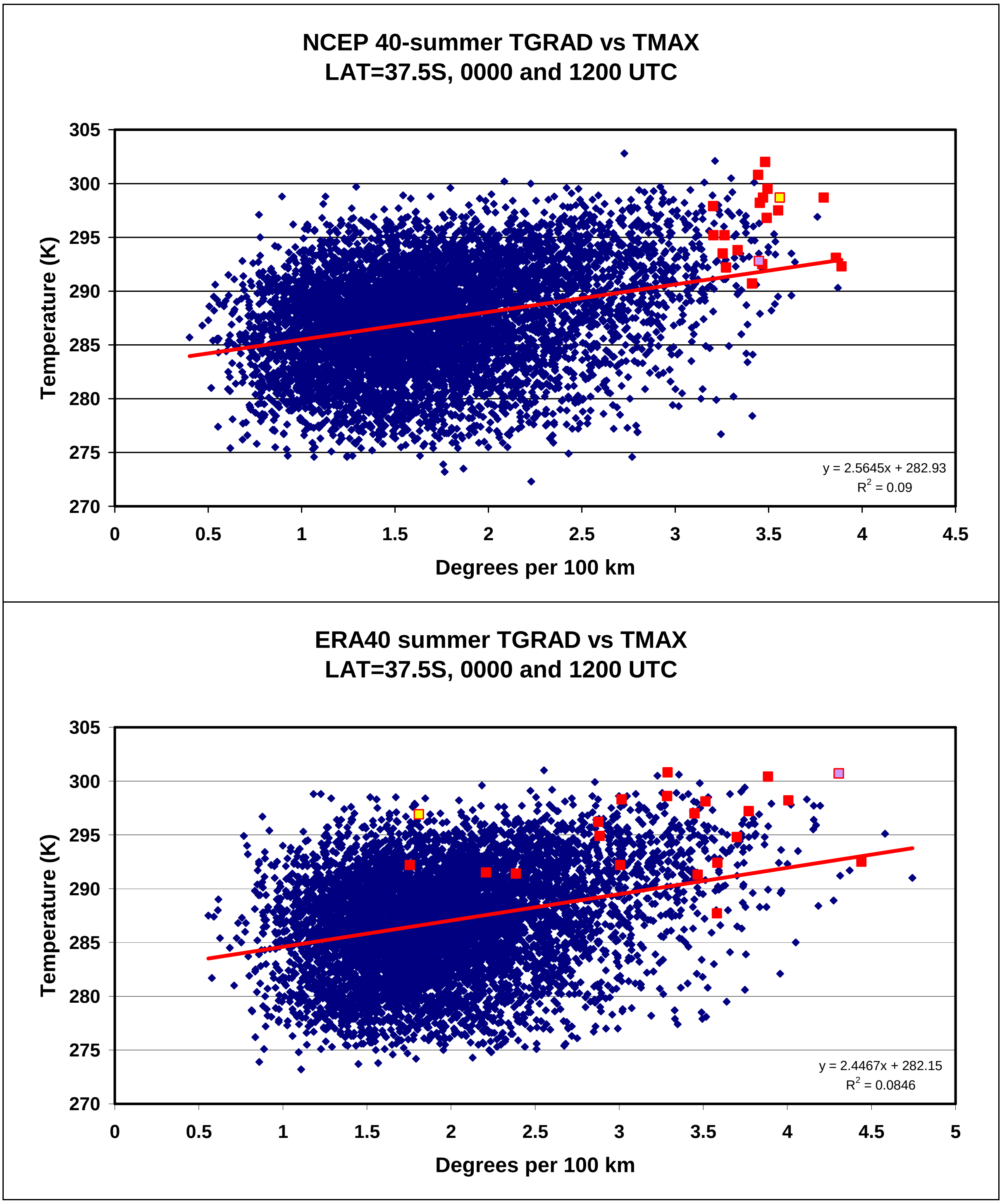

Figure 12: *Scatter-plot and its linear regression of the 850hPa maximum thermal gradient versus the maximum temperature on 37.5S over the Victorian Box at 0000 UTC and 1200 UTC during summer for the period 1964-2002 for the NNR data set (top) and for the ERA40 data set (bottom). The highlighted squares are for the events listed in Table 5.*

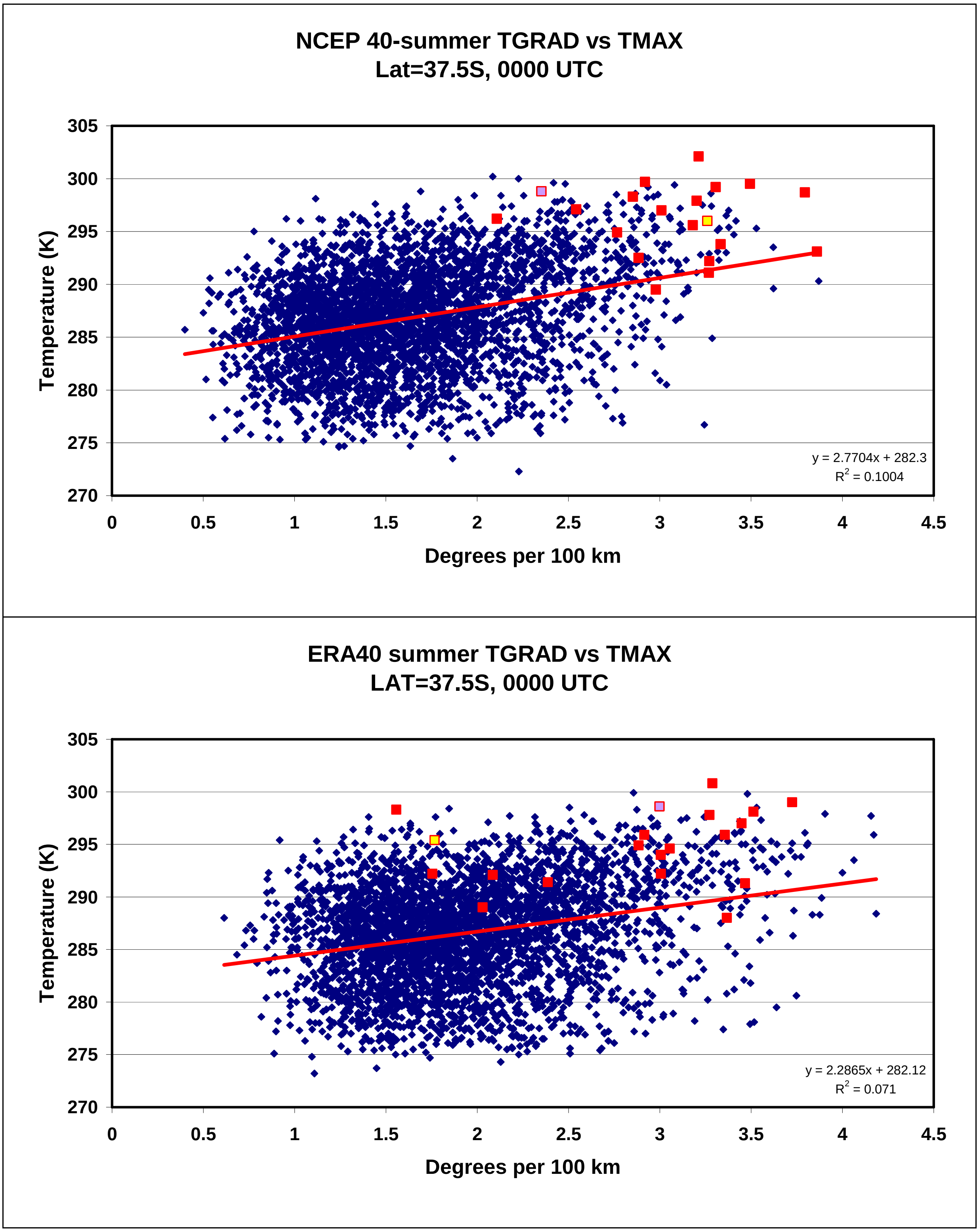

Figure 13: *Scatter-plot and its linear regression of the 850hPa maximum thermal gradient versus the maximum temperature on 37.5S over the Victorian Box at 0000 UTC during summer for the period 1964-2002 for the NNR data set (top) and for the ERA40 data set (bottom). The highlighted squares are for the events listed in Table 6, with the 0000 UTC T_G values for the given date selected.*

Location		Date			NNR		ERA40		ERA40 modified	
					T_G	Tmax	T_G	Tmax	T_G	Tmax
Longwood	■	1965	1	17	2.11	296.2	3.36	295.9	3.61	295.3
Brigalong	■	1965	2	22	3.27	292.2	1.56	298.3	2.70	292.1
Hobart	■	1967	2	7	3.26	296.0	1.77	295.4	2.58	294.5
SE Australia Fires	■	1968	1	31	2.85	298.3	2.08	292.1	2.91	296.5
Yarra Junction	■	1972	12	2	3.86	293.1	1.38	294.9	2.74	287.9
Western District	■	1976	1	3	3.01	297.0	1.75	292.2	2.46	296.1
Streatham	■	1977	2	12	3.18	295.6	2.88	294.9	2.88	294.9
Paynesville	■	1978	1	15	3.79	298.7	3.01	292.2	3.01	292.2
Caroline Forest	■	1979	2	3	3.33	293.8	3.05	294.6	3.05	294.6
Mallee	■	1981	1	3	3.20	297.9	3.45	297.0	3.48	297.0
Central Victoria	■	1982	1	11	2.54	297.1	2.91	295.9	2.91	295.9
Yallourn	■	1982	1	24	3.21	302.1	3.29	300.8	3.29	300.8
Wombat/D	■	1983	1	9	3.27	291.1	3.47	291.3	3.47	291.3
SE Australia (Ash Wednesday)	■	1983	2	16	2.35	298.8	3.00	298.6	3.73	286.3
SE Australia, 33 fires	■	1984	2	26	2.88	292.5	2.03	289.0	4.00	292.3
Central Victoria	■	1985	1	14	2.920	299.7	3.272	297.8	3.272	297.8
SE Australia, 132 fires	■	1990	1	3	3.49	299.5	3.51	298.1	3.51	298.1
Tasmania	■	1996	12	25	2.98	289.5	3.37	288.0	3.37	288.0
NSW/Tasmania	■	1997	12	21	2.77	294.9	3.01	294.0	3.01	294.0
SA/Mt. Macedon	■	1998	2	26	3.31	299.2	3.72	299.0	3.72	299.0

Table 5: *Table of historical disastrous fire events in southeast (SE) Australia over 1964-2000, adapted from Mills (2005), featuring for each fire event its location, date, values of the T_G and T_{max} from NNR and ERA40 datasets and from the "ERA40 modified" dataset as described in this section. The symbols in column 2 correspond to the highlighted points in Figures 12 and 13.*

Examples of individual events that illustrate this point are shown in Fig. 14, where the NNR and ERA40 analyses of 850 hPa temperature at 0000 UTC on the day of and the day following the 1967 Hobart and 1983 Ash Wednesday fires. One can immediately see the differences in the patterns between the two data sets in 1967, with the ERA40 analyses having a considerable phase difference in the position of the 850 hPa temperature gradient over Tasmania/Victoria. The differences between the two reanalyses are rather less for the Ash Wednesday case (Fig. 15), although subtle differences are still seen. In both diagrams, though, the steady progression of the baroclinic zones over the 24-hour period is clearly seen. The fact that the differences between NNR and ERA40 appears smaller for more recent cases than older one is consistent with findings that the ERA40 is much improved product in the post-1979 satellite era while the NNR product is most consistent over time (Bromwich and Fogt, 2004).

	ERA-40	NCEP/NCAR
0000 UTC 06 February 1967	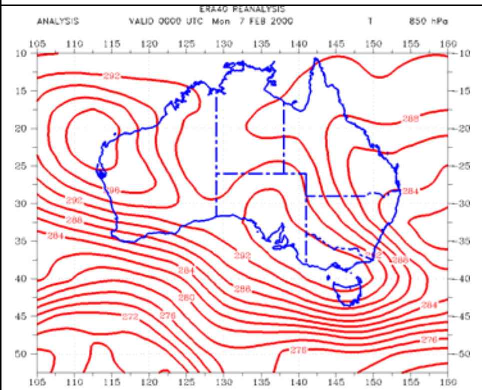	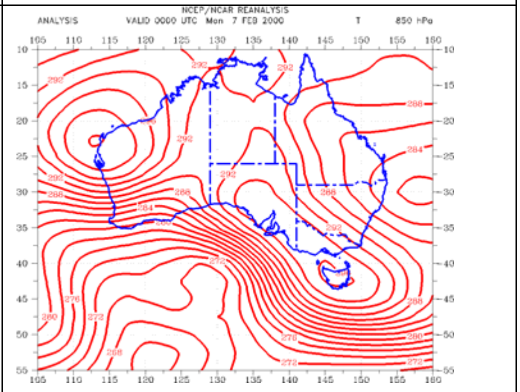
1200 UTC 07 February 1967	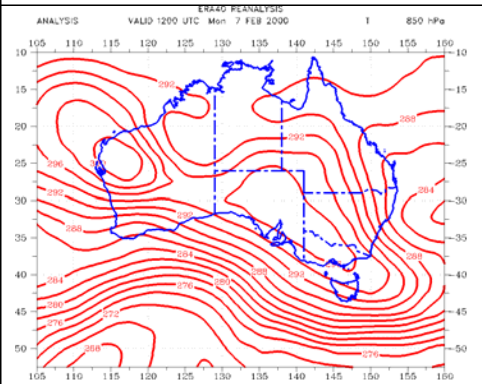	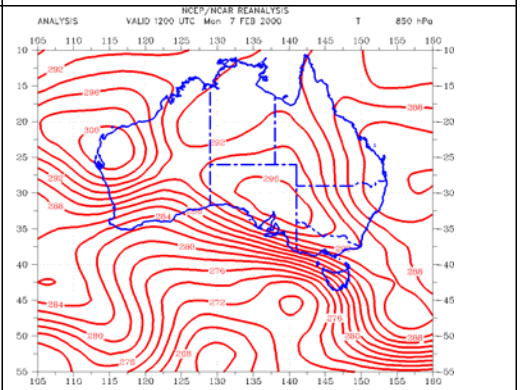
0000 UTC 08 February 1967	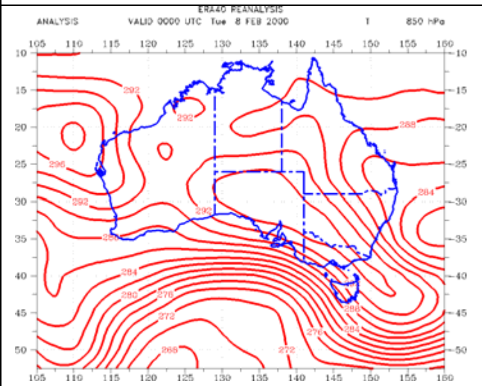	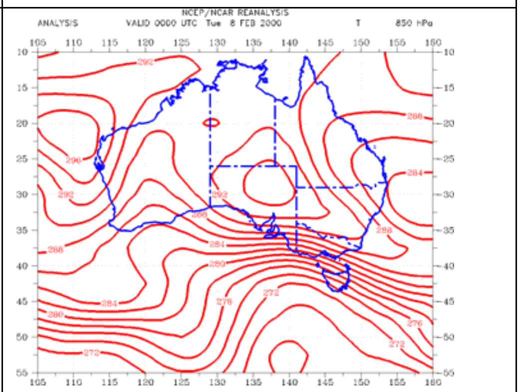

Figure 14: *Temperature analyses at 850 hPa from the ERA40 (left) and NCEP/NCAR (right) reanalysis data sets for the 7-8 February 1967 Hobart fires event shown at 12-hour intervals (top to bottom) from 0000 UTC 7 February 1967.*

	ERA40	NCEP/NCAR
0000 UTC 16 February 1983	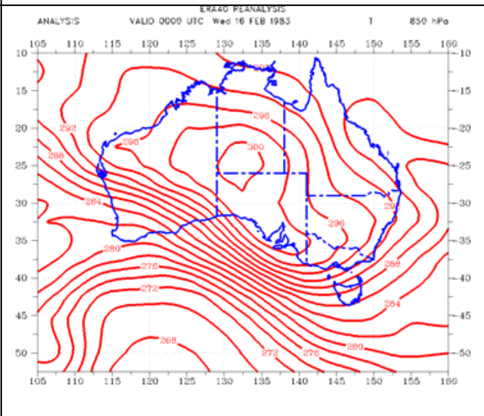	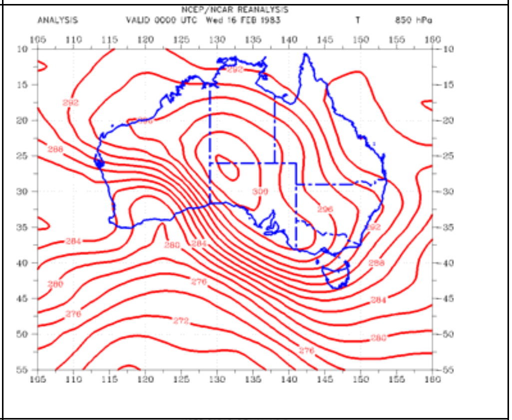
1200 UTC 16 February 1983	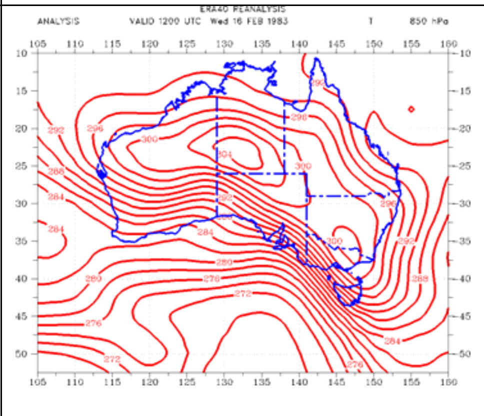	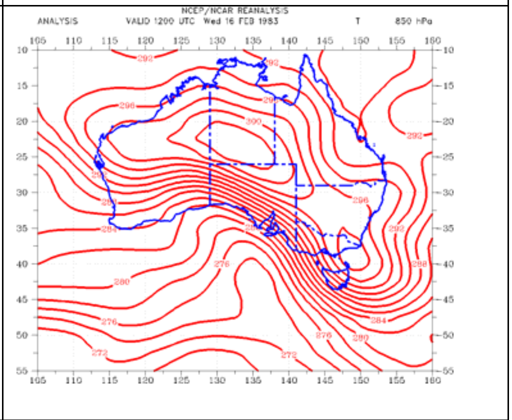
0000 UTC 17 February 1983	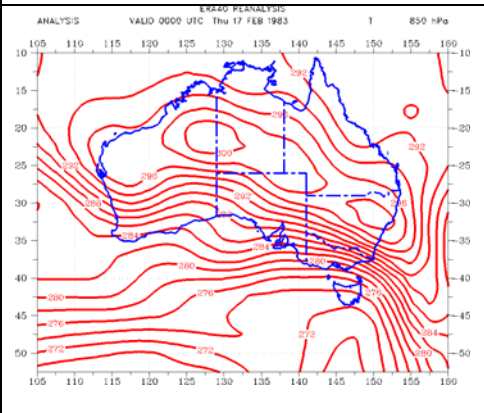	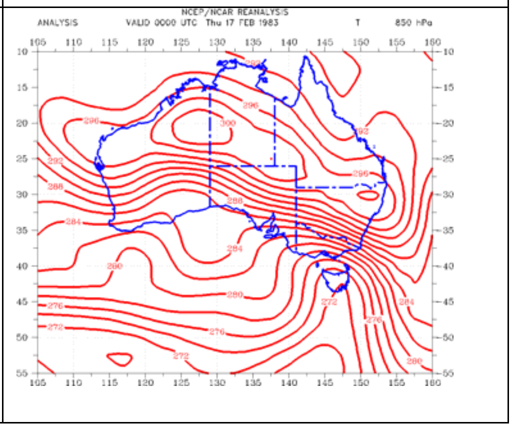

Figure 15: *Temperature analyses at 850 hPa from the ERA40 (left) and NCEP/NCAR (right) reanalysis data sets for the 16 February 1983 Ash Wednesday fires event at 12-hour intervals (top to bottom) from 0000 UTC 16 February 1983.*

The evolution of the patterns of 850 hPa temperature gradient seen in the two case examples in Figs. 14 and 15, suggests that if only 0000 UTC analyses are to be used for comparison with known fire events, some of the sampling issues may be ameliorated if the highlighted “event points” in the scatter plot diagrams (Figs. 12 and 13) were defined by the highest gradient at 0000 UTC on the nominal date of the fire, and that at 0000 UTC the following day, and we present this analysis in Fig. 16. There is a considerably stronger clustering of the event points towards the high T_G/high T_{max} zone of the scatter plots when compared with Fig. 13.

An alternative way of illustrating this point is noting the six event points in Fig. 14b that have relatively high temperatures, but T_G values less than 2.5. These events are shaded in Table 6, which lists, for each event, the 0000 UTC values of T_G and T_{max} for NNR, for ERA40, and also for the following day for ERA40. Each of these events showed a higher T_G value at 0000 UTC on the day following the date of the fire event, although on only two of those six days was T_{max} also higher. This is consistent with the eastward movement of a frontal system such that a baroclinic zone further east in the VB would be more likely to have a lower T_{max} than one in the western part of the VB.

It thus appears that, while less satisfactory than having a 12-hour interval between analyses, applying this technique to a time sequence of analyses at 24-hour intervals does show a clear association with major extreme fire events over southeastern Australia. This is an important result in the context of this study, as it makes it possible to apply the technique to the CMIP3 data set, for which only 0000 UTC data are readily available. Thus, if the climate change models available to this study can reproduce the broad characteristics of the past and future climates, then the applications of the T_G/T_{max} analysis to these data sets may provide a means of assessing the likely changes in extreme fire weather events associated with strong, mobile fronts. Climate models do not, of course, simulate actual events, and so the assessment based on the highest temperature gradient on two successive analyses is not necessary in the further application of the method – it is simply enough to perform the assessment based on each 0000 UTC output through the climate model's simulation.

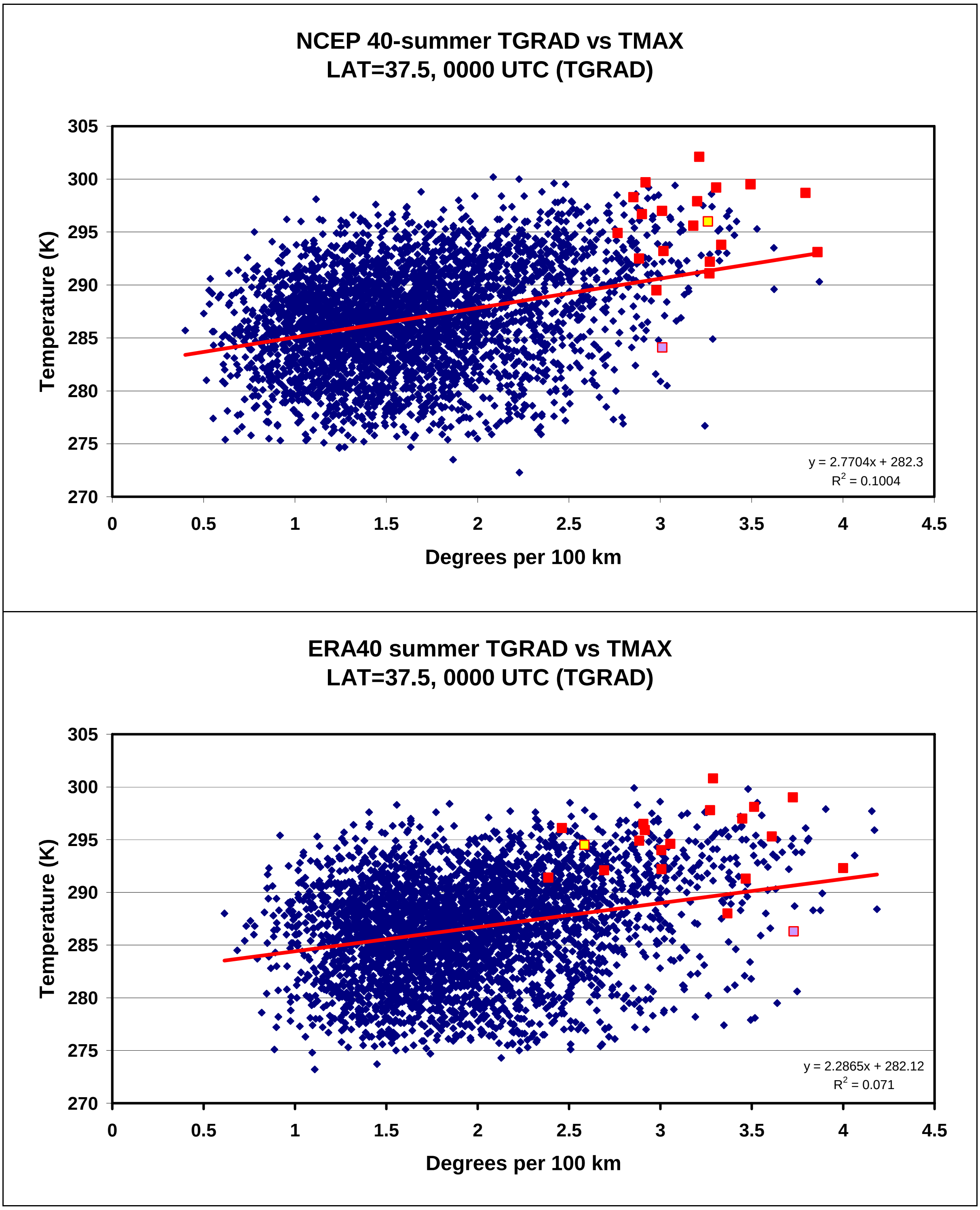

Figure 16: *Scatter-plot and its linear regression of the 850hPa maximum thermal gradient versus the maximum temperature on 37.5S over the Victorian Box at 0000 UTC during summer for the period 1964-2002, for the NNR data set (top) and for the ERA40 data set (bottom). The highlighted squares are for the events listed in Table 6, with the higher of the 0000 UTC T_G values for the given date and the following date selected.*

6) Adapting the methodology to climate models

The preceding section provided some level of confidence in applying the diagnostic approach of Mills (2005) to data sets valid at 0000 UTC only. However, while both ERA40 and NNR reanalyses are available on the same 2.5x2.5° grid, the IPCC-AR4 climate models used here (see Table 5) have a range of grid configurations and resolutions, and accordingly separate "Victorian Boxes" need to be specified for each model. A consequence is that the latitude line of 37.5°S on which the T_{max} parameter was determined with the reanalyses is not necessarily available in the climate model data, and so some care must be taken in specifying this latitude, particularly given that for the coarser resolution models the latitude increments may be as large as 4°. Before describing the sizes of the various boxes specified for each of the climate models, and discussing the choice of latitude used for calculating T_{max}, we make a synoptic assessment of the ability of the models to reproduce extreme thermal patterns such as those shown in Figs. 14 and 15.

a) Synoptic aspects of climate-model extreme events

The aim of this study is to assess the evolution of the frequency of deep, strong fronts moving through southeastern Australia. The methods for extracting those climate model events from the time-series of model data will be statistical, and based on the phase space diagrams as shown in Fig. 5. To a make an initial assessment of the ability of the models to reproduce the synoptic structures seen on, for example, Ash Wednesday we present in this section a brief discussion describing the synoptic patterns associated with the strongest T_G events from the model's 20th century climate simulations. As described by Mills (2005), on 16 February 1983 a deep eastward propagating trough was located just west of the Victorian coast. Figure 17 shows the MSLP and 850 hPa temperature analyses from ERA40 and NNR for 0000 UTC on that day. The trough approaching the Victorian coastline and a ridge off the south-west coast of Western Australia can also be observed in both the MSLP analyses. In addition, the temperature field at the 850hPa level shows a deep layer of hot air above most of central and southeast Australia as well as a cold pool located over the south-western corner of Western Australia, and a very strong temperature gradient, with northwest-to-southeast oriented isotherms, between these two centres.

The climate models do not predict a particular event on a given day, so some other method must be used to select extreme days, and for the purposes of this exercise we select, for each model, the two events with the highest values of T_G, commencing from the beginning of our data set (1 January 1964), so long as the days were not consecutive.

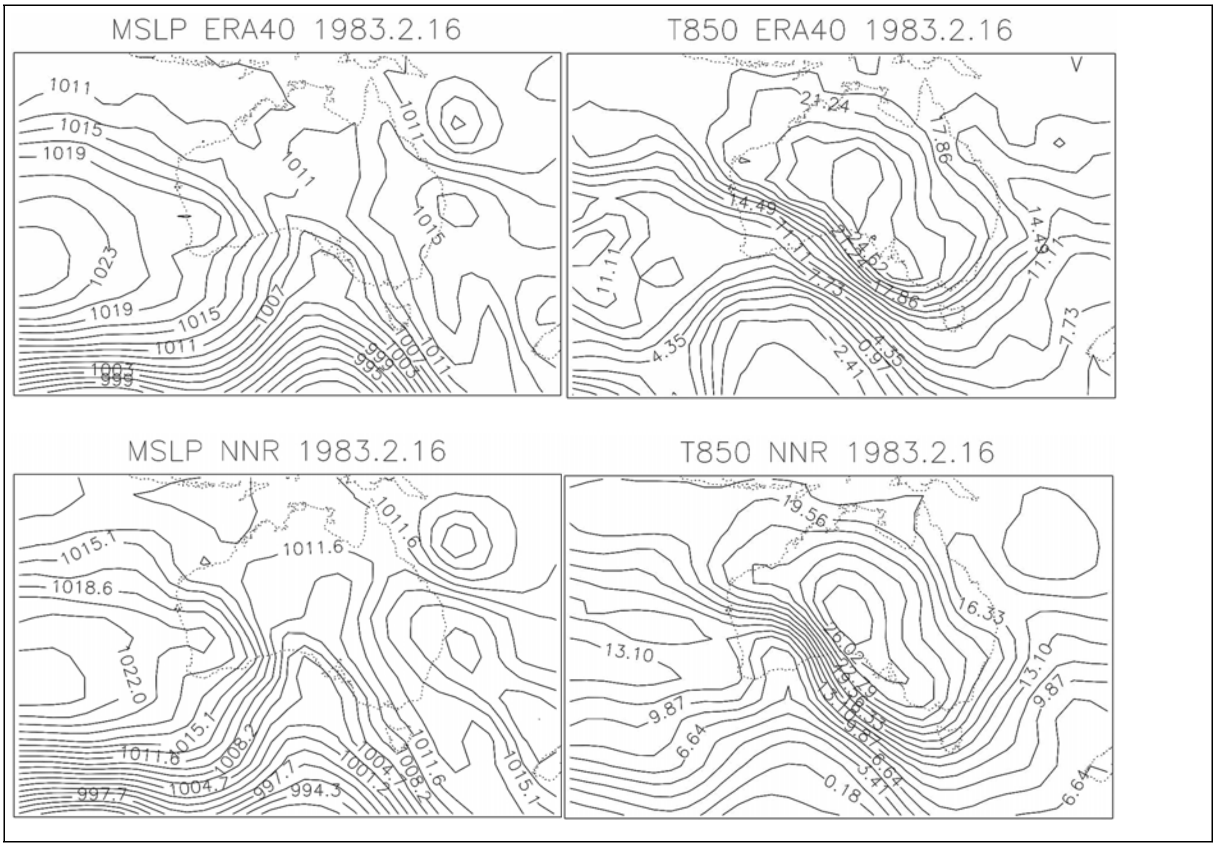

Figure 17: *Fields of Mean Sea Level Pressure and temperature at 850 hPa from the ERA40 and NNR data sets for Ash Wednesday 1983.*

The 850hPa temperature fields for these two events for each model are shown in Appendix 1, and, as examples, the fields of MSLP and of 850 hPa temperature for the two cases with highest T_G for the MRI model in Fig. 18. Characteristics similar to the ones observed in the reanalyses for Ash Wednesday (Fig. 17) can be seen, such as the region of warm air across central Australia to Victoria, the cold pool over the southwest of Western Australia, and strong surface troughs over southeastern Australia.

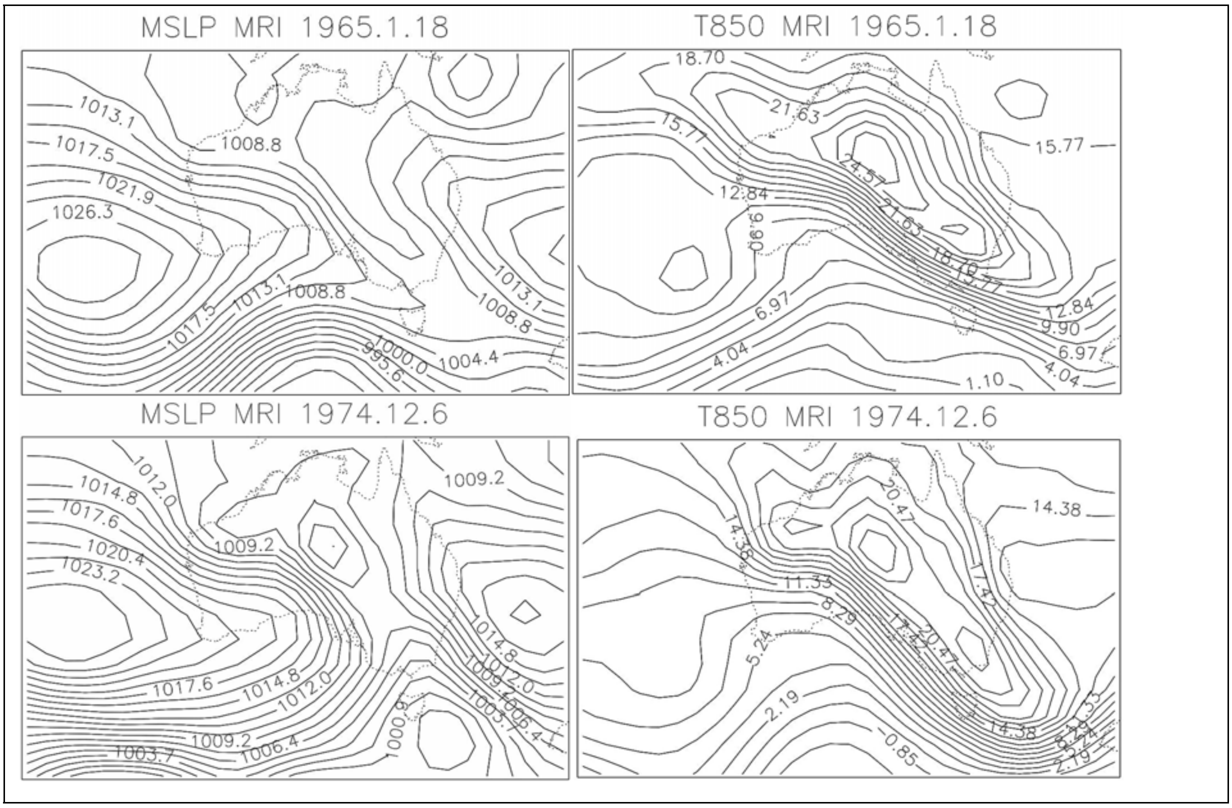

Figure 18: *Fields of Mean Sea Level Pressure and temperature at 850 hPa from the MRI model set for two extreme two cases.*

When one examines the range of extreme solutions shown in Appendix 1 it is seen that most of the models, despite their coarse resolution, reproduce the type of synoptic situations observed during historical extreme fire days, with tightly-spaced northwest-southeast isotherms near southeastern Australia. The ability of these climate models to simulate extreme events was noted in the last IPCC Working Group 1 report in the "climate models and their evaluation" section (Randall et al. 2007). However, a few of the models, notably CSIRO (left panel), GFDL1 (right panel) and GISSR (right panel) appear to show some differences from these archetypal patterns.

b) Defining the Victorian Box

The sizes of the boxes were chosen to be as close as possible to the VB bounds used in Mills (2005) subject to the grid spacing of the respective models. In most cases this resulted in slightly larger geographic areas, but not necessarily a larger total number of gridpoints on which the gradient calculations were made. Table 6 lists the number of gridpoints in each direction, and the latitude/longitude extent, of the target areas selected for each model. Diagrams showing the selected area and the land-sea masks for each of the models are shown in Appendix 2.

	ERA/NNR	CCM	CNRM	CSIRO	GFDL1	GFDL2	GISSR	IPSL	MIROC	MPI	MRI
Longitude Grid-points	6 (12.5)	4 (11.4)	6 (14.0)	8 (13.3)	7 (15.0)	7 (15.0)	4 (15.0)	4 (11.1)	6 (14.0)	8 (13.3)	6 (14.0)
Latitude Grid-points	3 (5.0)	3 (7.4))	4 (8.4)	5 (7.6)	5 (8.0)	5 (8.0)	3 8.0	4 (7.5.0)	4 (8.4)	5 (7.6)	4 (8.4)

Table 6: *Number of longitude and latitude lines in each models' VB on which values of T_G are calculated using centred differences. The bracketed values are the size (in degrees) of the entire VB box in each dimension.*

c) Selection of the maximum temperature latitude

As described above, the parameter T_{max} is calculated in the VB along latitude 37.5S when applied to the reanalyses. Our first choice in selection of an equivalent latitude for the climate models was the latitude closest to 37.5S, but varying relationships of this 'closest' latitude to the model's particular land-sea masks prompted us to question the sensitivity of our results to this choice. Accordingly scatter plots equivalent to Fig. 16 were prepared from each model's simulation of the 20th century climate (December-January-February for the years 1964-2000 inclusive) at this "closest" latitude, and also at the next lower (closer to the equator) latitude, as listed in Table 8 and shown graphically in Appendix 2.

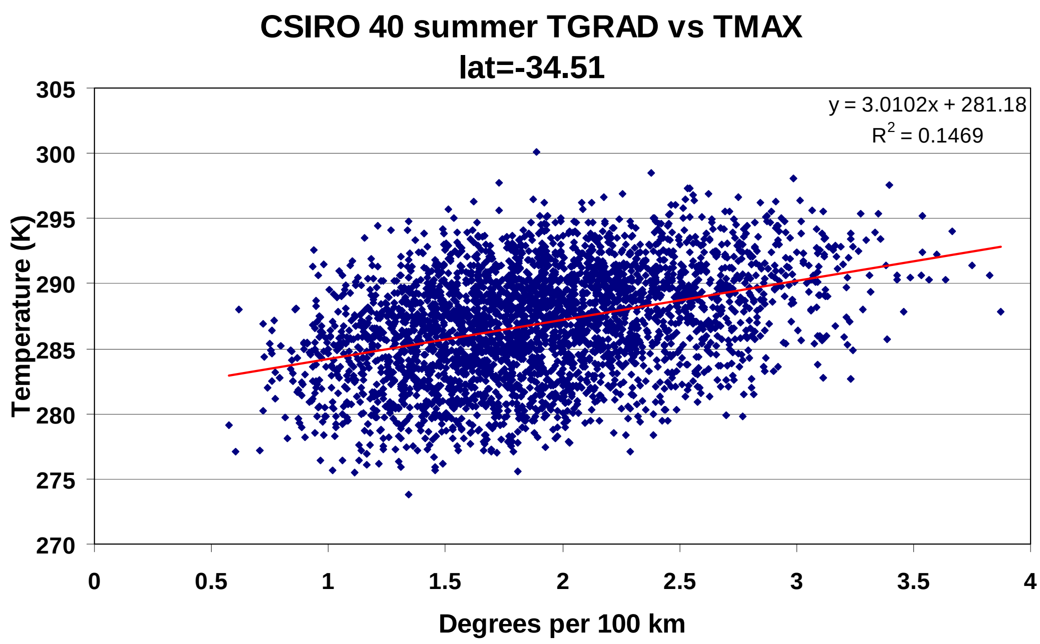

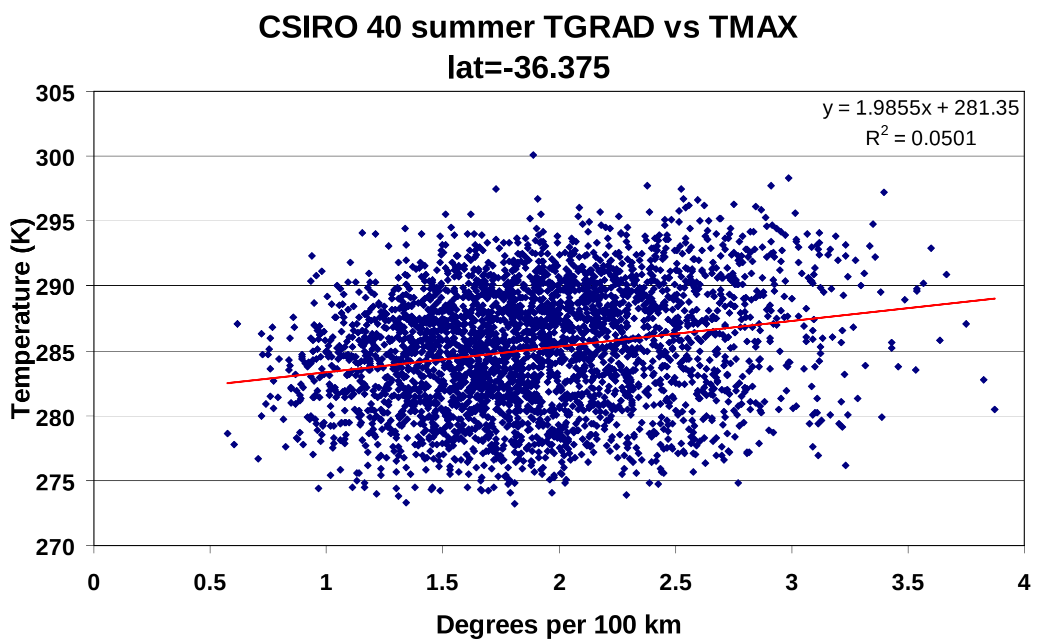

Figure 19: *Scatter-plots and their linear regression of the 850hPa maximum thermal gradient versus the maximum temperature on for latitudes 34.51S and 36.375S over the CSIRO VB at 0000 UTC during summer for the period 1964-2003, using the CSIRO model output.*

The scatter plots for each model for each of the two latitudes are shown in Appendix 3, and it is immediately apparent that there is considerable sensitivity of the shape of the scatter distribution to selected latitudes, with some showing virtually no correlation in T_{max} with increasing T_G, as seen for the reanalyses (although we are not implying that there is any necessary physical meaning to this correlation). An example for the CSIRO model is shown in Fig. 19; it is seen that the slope is some 50% greater for the neighbouring latitude further north than for the one further south.

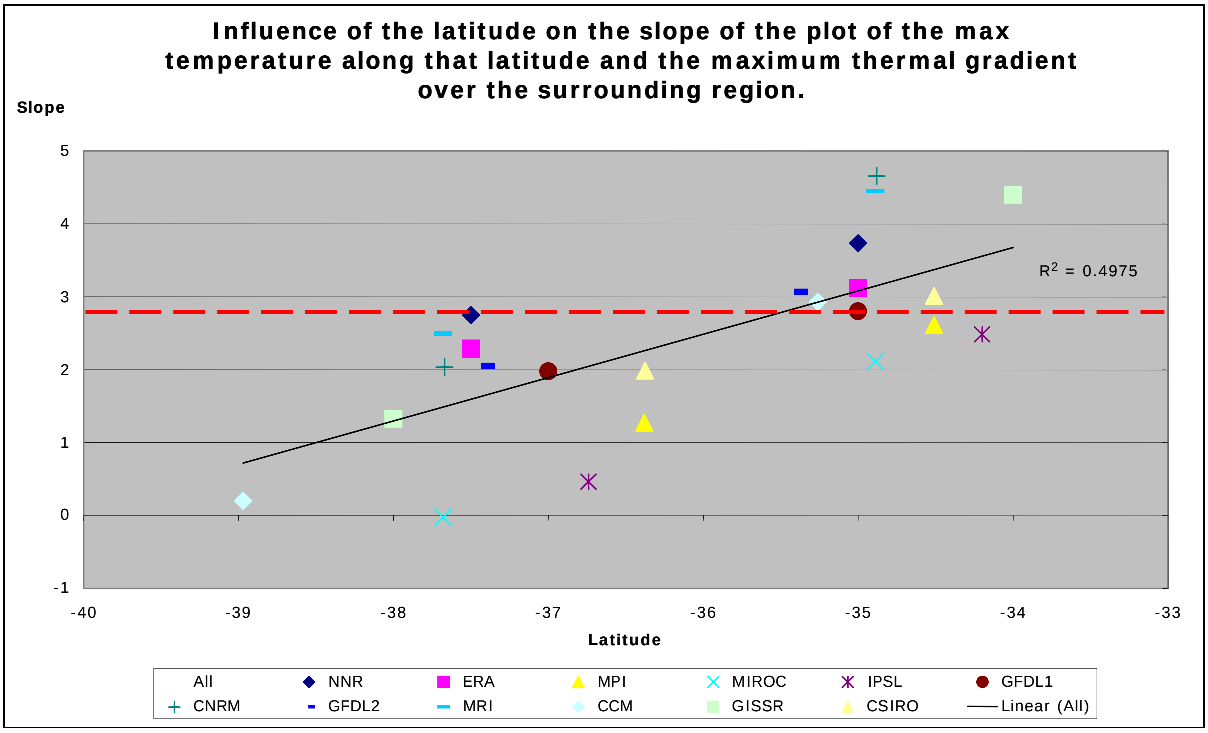

Figure 20: *Relationship between the slope of the scatter plot for each model and selected latitude versus latitude. The dashed red line shows the slope of the NNR scatter plot at 37.5S.*

One subjective criterion on which the selection of the latitude for determining T_{max} could be based is to choose the latitude which produces a slope on the scatter plots which is closest to that of the NNR scatter plot. Figure 20 shows a plot of the slope for each model at each latitude versus latitude; there is a strong relationship between slope and latitude, with a correlation of 0.71. The ERA40 data set matches the NNR slope very closely at both 37.5 and 35S latitudes. However the slope for the NNR dataset at 37.5S is 2.7205 (dashed red line) and some models match this slope better at the lower, and some at the higher latitude.

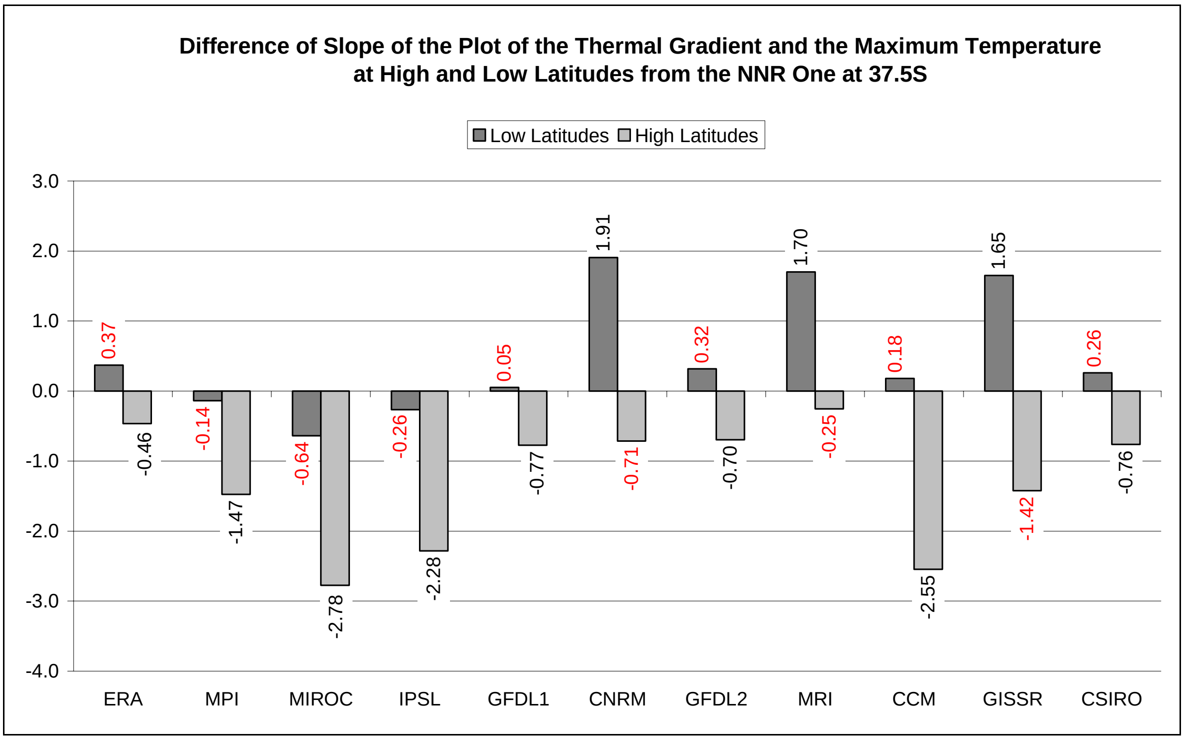

Figure 21: *Histogram of the difference between the slopes of linear regression for each IPCC-AR4 model for the two latitudes listed in Table 8 and that of the NNR scatter plot slope at 37.5S. The smallest value for each model is highlighted in red.*

Figure 21 shows this in a different way, with the difference between the slopes for each model's scatter plot at each latitude and that of the NNR scatter plot at 37.5S. The ERA40 data set reproduces the slope very closely at both latitudes. Only three models (CNRM, MRI, and GISS-R) show a better match at the higher latitude. These "selected latitudes", which best match the slope of the trend line in the NNR scatter plot, are listed in Table 8, and scatter plots of T_G versus T_{max} for these selected latitudes are shown for each of the 10 IPCC-AR4 models in Fig. 22.

IPCC Model	Lower Latitudes	Higher Latitudes	Selected Latitudes	
CCM	- 35.26	- 38.97	- 35.26	Low
CSIRO	- 34.51	- 36.37	- 34.51	Low
MIROC	- 34.89	- 37.68	- 34.89	Low
MPI	- 34.51	- 36.37	- 34.51	Low
MRI	- 34.89	- 37.68	- 37.68	High
CNRM	- 34.88	- 37.67	- 37.67	High
GFDL1	- 35.00	- 37.00	- 35.00	Low
GFDL2	- 35.41	- 37.43	- 35.41	Low
GISSR	- 34.00	- 38.00	- 38.00	High
IPSL	- 34.20	- 36.74	- 34.20	Low

Table 7: *Table of the two latitudes, examined for each model and at which latitude T_{max} is selected. The "Higher Latitudes" correspond to the model line the closest to 37.5S and the "Lower Latitudes" to the ones just equatorward from the "Higher Latitudes". The "Selected Latitudes" correspond to the one selected (see below).*

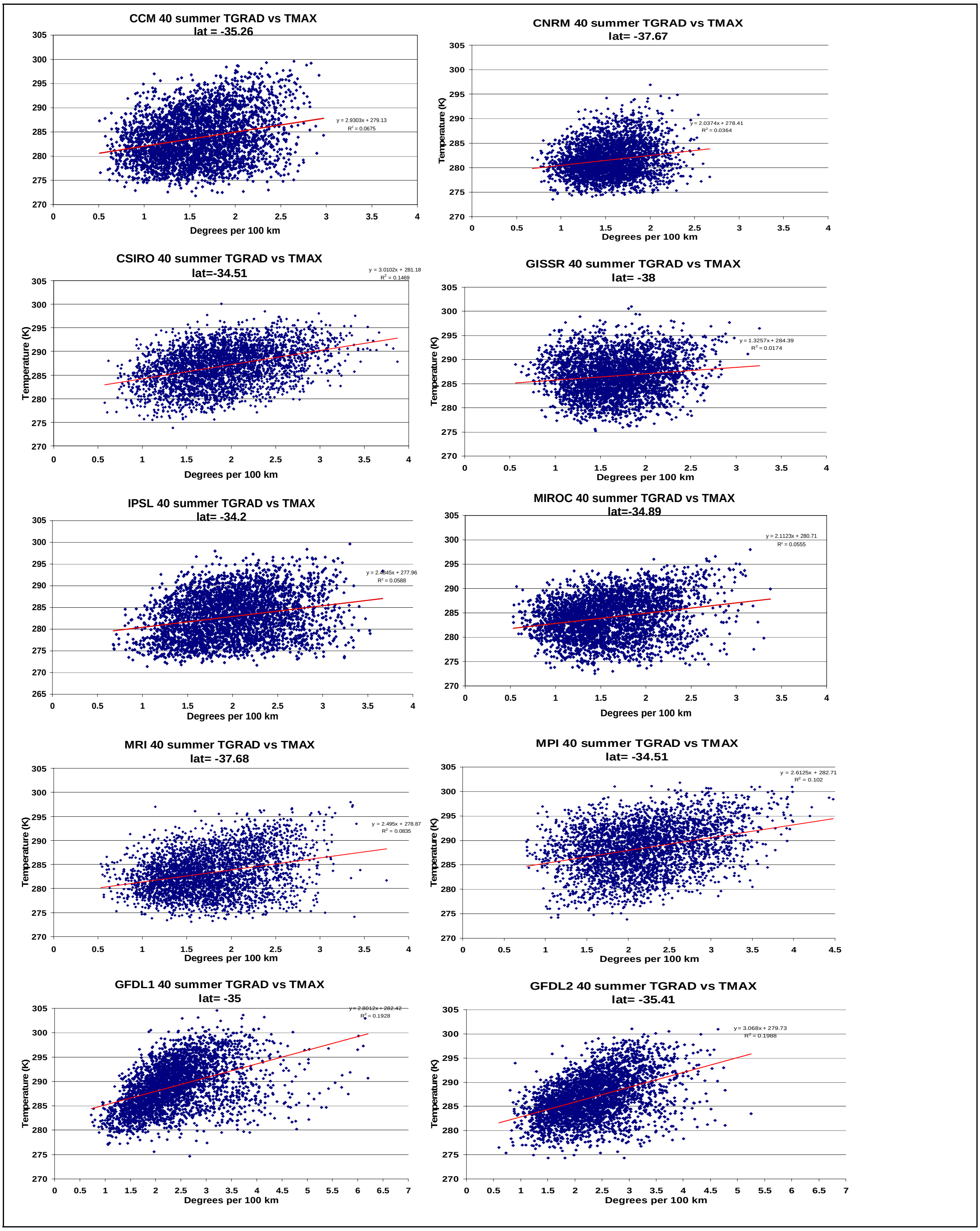

Figure 22: *Scatter plots and linear trend lines analogous to Fig. 5 for all IPCC-AR4 models at the "Selected Latitudes" listed in Table 7.*

d) Specifying Thresholds

In order to assess how the numbers of these extreme fire weather events may vary under climate change scenarios, we have opted to develop thresholds for T_G and T_{max} that jointly define the phase space of diagrams such as Fig. 5 in which such fronts occur. Then under climate model projections a change in frequency of such events can be inferred. A simple approach to determining thresholds for T_G and T_{max} that jointly define the environments in which the hypothesised extreme fire weather events may occur is shown by the red lines overlayed on Mills' (2005) scatter plot in Fig. 5, with lines used to delineate the zone that includes the events. These thresholds are 3.2 for T_G and 290K for T_{max}. However, simply applying these thresholds to each of the climate models is problematic due to the different distributions of T_G vs. T_{max} seen in Fig. 22. It is not possible with the CMIP3 simulations of the climate of the 20th century to evaluate the model's ability to reproduce observed events. Only the distributions of the model parameters can be used. We have tested two methodologies to define thresholds based on the statistical distribution of the model's temperature and temperature gradient distributions. These methods are described below.

Method 1: simple analysis of the distribution

Given that the process of determining thresholds for a parameter involves the investigation of the most extreme values, any specified threshold depends crucially on the characteristics of its Probability Distribution Function (PDF). A linear relationship between the mean (μ) and the variance (σ) of the NNR PDF and the thresholds shown in Fig. 5 can be derived (see box below), and then be applied to the mean and variance of each model (see Appendix 4) to provide model-specific thresholds.

$$\mu + a\sigma = threshold$$

For T_G :
$$1.64776 + a \times 0.31365 = 3.2$$
$$\Rightarrow a = 4.9489$$

For Tmax :
$$288.9 + a \times 21.01 = 290$$
$$\Rightarrow a = 0.0523$$

First applying this method to the ERA40 data set gives 28 cases above the thresholds, which is very close to the 27 obtained with the (dependent data) NNR analyses for the period 1964-2000 from the IPCC-AR4 climate models that is used to define their climate of the 20th century. Generating similar statistics for each of the climate models, though, produces a wide range of 'events' (Fig. 24), ranging from 7 to 113, or between ~25 and ~400% of the reanalysis numbers. This large range suggests that this approach to defining the thresholds has its limitations, and that alternative approaches should be investigated.

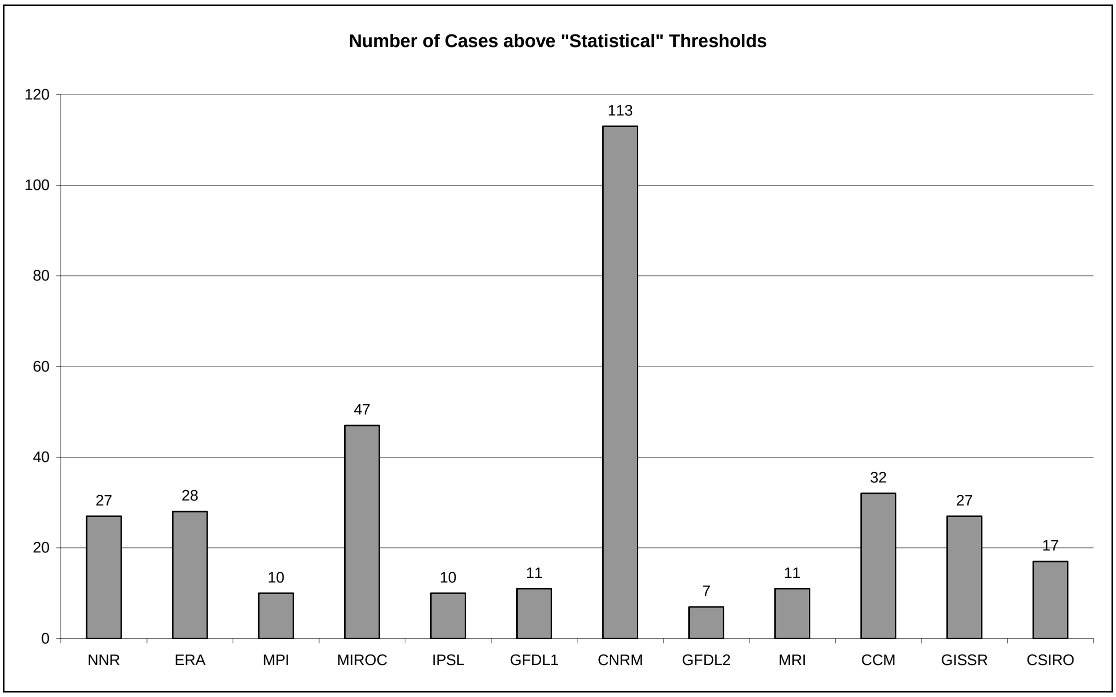

Figure 23: *Number of cases above the thresholds calculated for each model using the first method.*

Method 2: using the proportion of cases above thresholds

This method is designed to keep the number of cases above the thresholds to the same order of magnitude for every model, with the two individual thresholds defined such that the same percentage of values are above each threshold for each model. This is displayed schematically in Fig. 24 for the NNR data set, and shows that ~1.13% of T_G values, and 28.39% of T_{max} values exceed those thresholds.

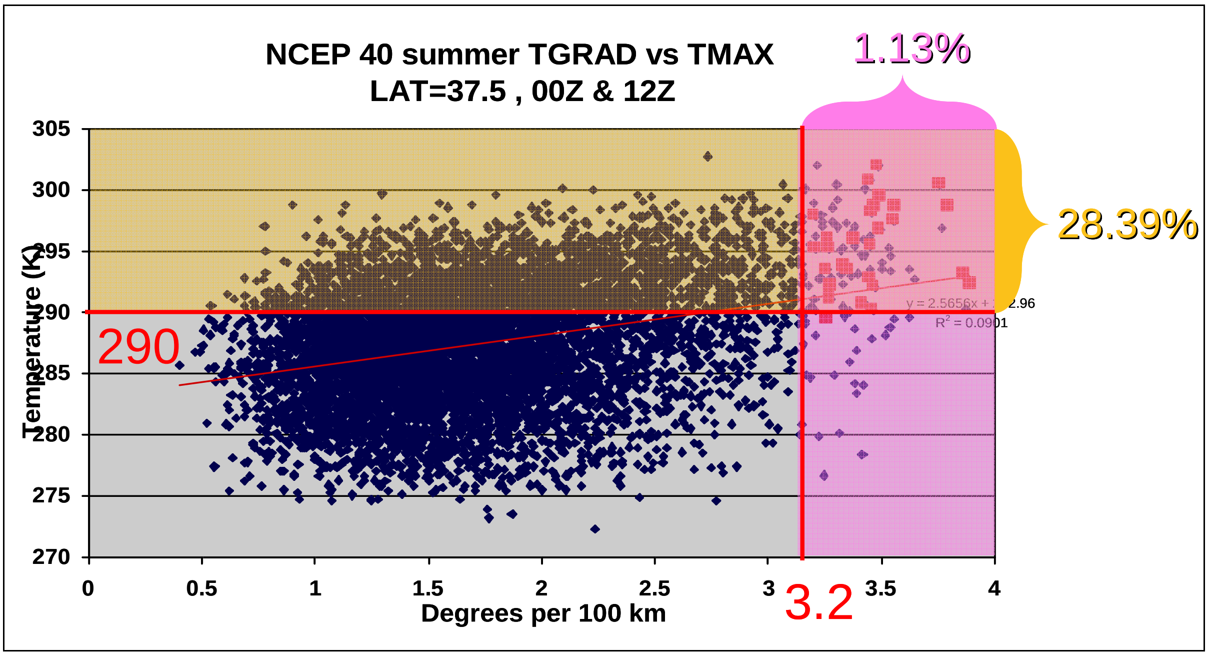

Figure 24: *The proportion of cases above the threshold lines for the plot shown in Fig. 5.*

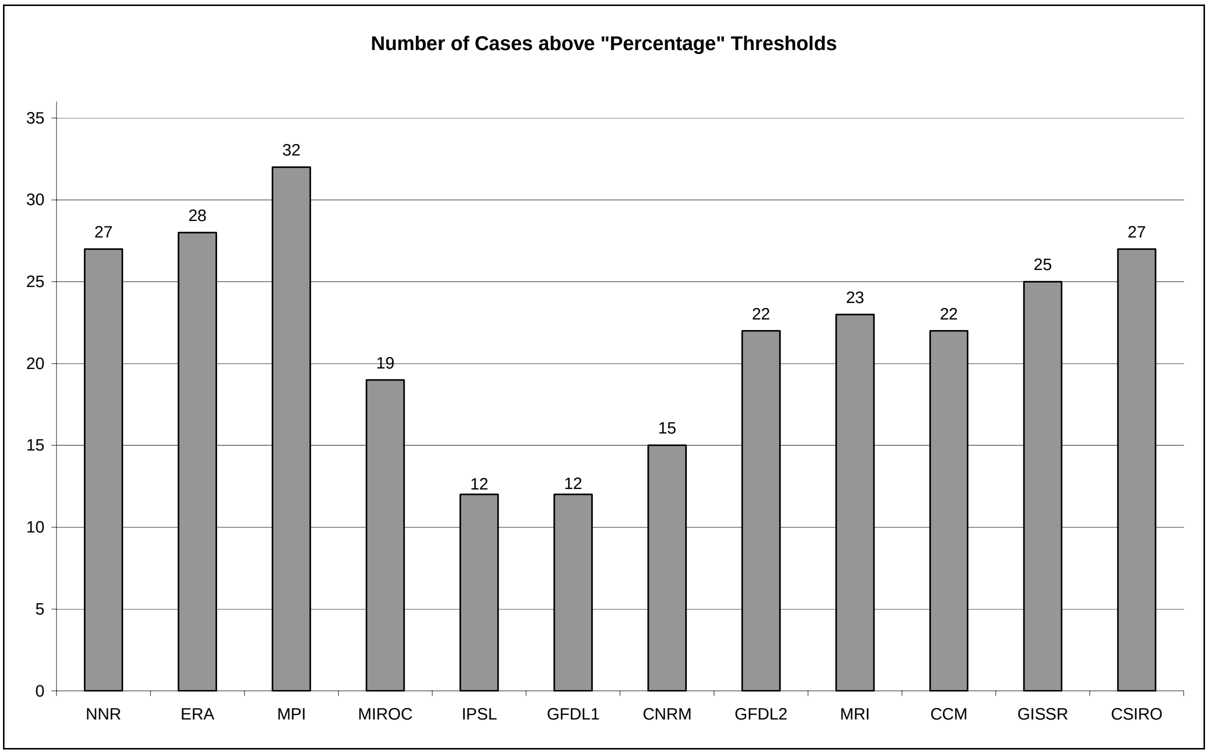

Figure 25: *Number of cases above thresholds for each model calculated using the second method.*

In this approach, the methodology is reversed from the previous way of setting the thresholds: the percentages are used to define the thresholds for both parameters for each model. With this methodology, we obtain 28 cases for the ERA40 dataset – the same as for Method 1. For the IPCC-AR4 models, the number of cases ranges from 12 to 32 cases above thresholds (Fig. 25). This is a much narrower spread than method 1, with only the IPSL and GFDL1 models producing less than half the number of extreme cases picked by the reanalyses, and no model giving more than 150% of that number

Summary of the threshold calculation methods

Two sets of empirical techniques based on the thresholds defined by Mills (2005) with the NNR set have been tested in this section. The values of thresholds calculated using each method, and the number of extreme events defined by them for each model at their "selected latitudes" are listed in Table 8.

Model	Selected Latitude	A	B	C	D	E	F
		{Thr(▼T) | μ,σ}	{Thr(T) | μ,σ}	Over th_μ,σ	{Thr(▼T) | %}	{Thr(T) | %}	Over th_%
NNR	-37.5	3.20	290.0	27	3.20	290.0	27
ERA40	-37.5	3.57	289.9	28	3.53	289.6	28
MPI	-34.5	3.95	285.1	10	3.66	291.5	32
MIROC	-34.9	2.68	281.9	47	2.82	286.7	19
IPSL	-34.2	3.26	280.7	10	3.15	286.2	12
GFDL1	-35	5.14	287.7	11	4.63	292.1	12
CNRM	-37.7	2.02	282.1	113	2.29	283.1	15
GFDL2	-35.4	4.46	285.3	7	4.06	289.4	22
MRI	-37.7	3.02	284.2	11	2.96	285.6	23
CCM	-35.3	2.59	285.1	32	2.62	286.7	22
GISSR	-38	2.48	292.4	27	2.65	289.0	25
CSIRO	-34.5	3.28	284.0	17	3.20	289.5	27

Table 8: *T_G and T_{max} threshold values and number of cases above them for each model, using the two calculation methods (respectively A, B and C with method 1 and D, E and F with method 2)*

Neither methodology gives constantly greater or lower values for the thermal gradient (T_G) threshold than the other. However the second methodology gives greater values of the maximum temperature threshold for all models. As noted above, the spread in the numbers of cases above the thresholds differs greatly between the two methodologies, from 15 cases to more than a 100. Across the full range of models, the second methodology gives a far more consistent number of cases above thresholds than the first, and as we believe that all available GCMs should be treated in a comparable manner in the application of this diagnostic, we have chosen to use this set of thresholds in the remainder of this study.

e) Model characteristics

The particular factors that cause the Probability Density Functions (PDFs) for each of the ingredients from each of the models to differ is rather difficult to assess, as they are the result of a large number of factors including model resolution, the numerical algorithms used, and the particular way in which physical processes are parameterised in each particular model. One particular aspect that is worth considering is the influence of the land-sea mask used in each model (see Appendix 2). Mills (2005) has drawn attention to the role of land-sea thermal contrast in enhancing or interacting with the synoptic-scale front to enhance frontogenesis over southeastern Australia. Figure16 shows an example where the 850 hPa thermal gradient strengthens as the front approaches the coastline of southeastern South Australia. As seen in the diagrams shown in Appendix 2, depending on the particular model, Bass Strait may or may not exist, with Tasmania in some cases included as part of the Australian continent or in other cases not represented at all. A plot of the T_G threshold versus the proportion of land in the land-sea mask in each models' individual VB is shown in Fig. 26, while a plot showing the relationship between the magnitude of the gradient and the size of the VB for each model is shown in Fig. 27.

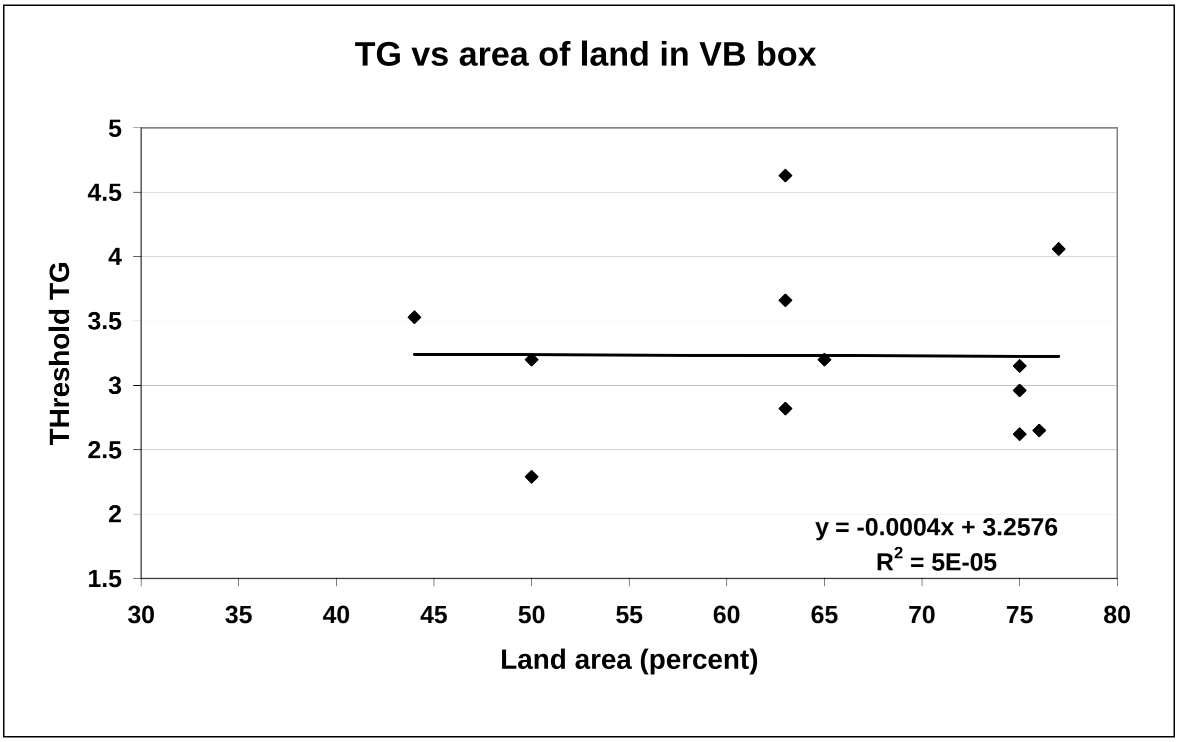

Figure 26: *Percentage of land for each model in their respective Victorian Box plotted against the T_G threshold. The trend line is shown by the solid line.*

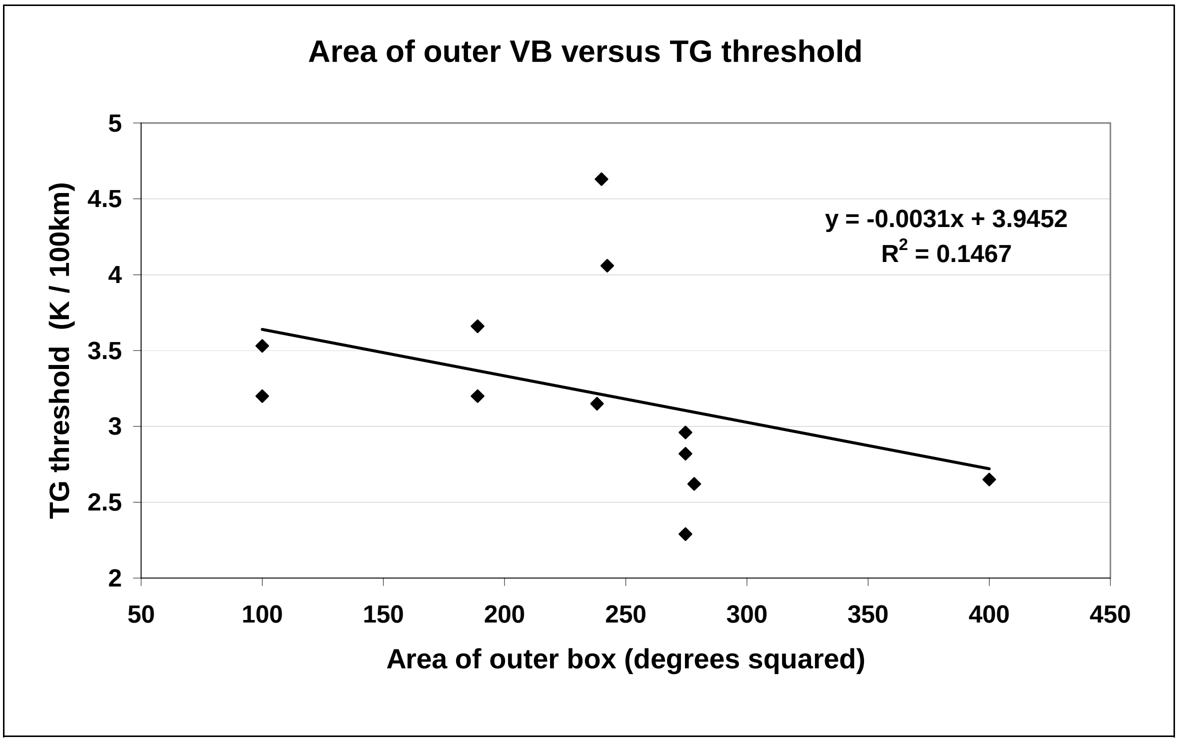

Figure 27: *Scatter plot of T_G threshold versus size of the VB box for each model.*

While there is no relationship between the value of the T_G threshold (determined above) and percentage of land inside the VB box for any particular model (Fig. 26), there does appear to be a weak inverse relationship between the actual size of the VB and the threshold T_G. This relationship becomes even weaker if only the box area for which gradients are calculated is used, rather than including those grid points that are used in the centred-difference calculation of T_G. It appears that any direct relationship between the particular land-sea mask used and variations in the threshold value of T_G is more complex than this simple analysis might reveal, and that the selected value is more a function of model characteristics than the size of the VB.

7) The CMIP3 models over the twentieth century

a) Evaluation of the models

While the ultimate aim of this project is to apply the thresholds determined in the previous section to climate change scenarios, it is apparent that the different models simulate subtle different climates. It is an obvious step to compare the individual model's simulation of the 20th century climate with that provided by the reanalyses. Although impossible to prove, it is a reasonable hypothesis that the "most reliable" models will best reproduce that climate, and that these "more reliable" models might then be considered more reliable in their projections of the climates of the middle and late 21st century, as argued in Randall et al. (2007) (see Fig. 7). In this section we present a series of tests to assess the closeness of fit of the climate model's PDFs of T_G and T_{max} to those of the reanalyses.

Simple statistical comparisons are presented in the next section, followed by a section describing higher-order tests are presented in the following section. As a result, we will categorise the models as having "closer" and "less close" fits to the reanalysis climates, but there is no exclusion of any models in our assessment of trends through the 21st century. These assessments could be used in a variety of ways: (1) we could rank and give weights to the models, (2) simply discard those considered outliers, or (3) include all models, but give greater subjective weight to those models which more closely match the reanalysis climates. Ranking the models and giving them weights is a subtle task because it is not known how much weight to give to the statistical tests themselves. Also, even if ranking the models' performance for each test is objective, it is not necessarily applicable for extreme events. This is even more evident in the second approach where the outlier model could be the model that reproduces the rare synoptic patterns linked to fire disasters. Therefore, we chose to use the third approach. The models will be placed for each test in one of three categories, which will be termed "close", "satisfactory" and "distant" in terms of their closeness to the reanalyses' climatology. The criteria for which a model will be assigned to a certain category will be based on the comparisons of the models' statistical distribution compared to that of the reanalyses.

Comparisons of mean, variance, and slope

These simple statistical tests involve the assessment of the ability of the models to reproduce the mean and the variance of the distribution of the two main parameters, T_G and T_{max}, and the slope of their scatter-plot.

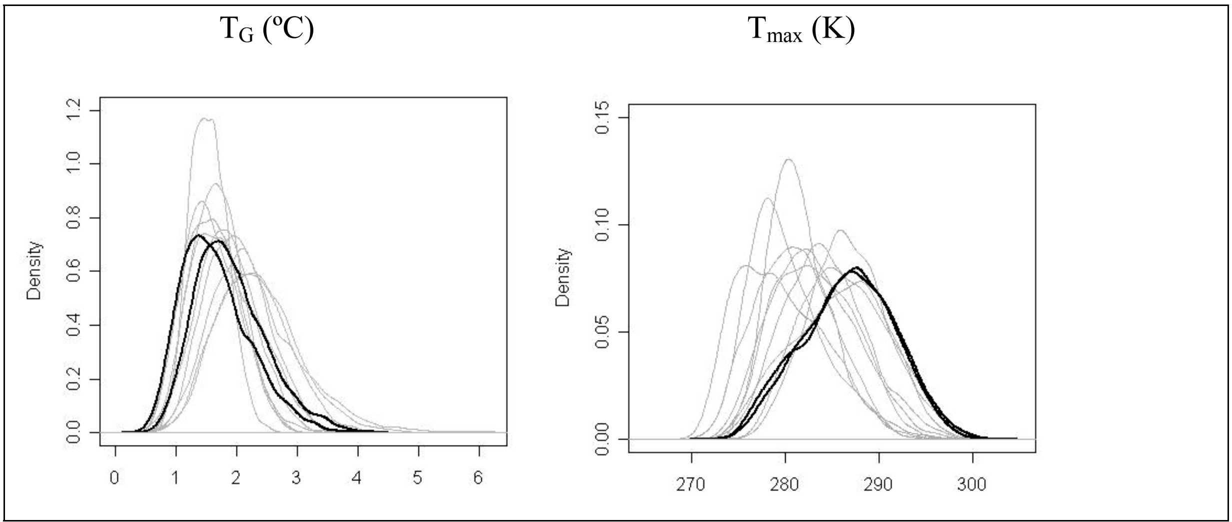

Figure 28: *Probability Density Functions of the maximum thermal gradient (left) and maximum temperature (right) along the selected latitude in each model VB, with the reanalyses PDFs in bold.*

The models tend to reproduce the distribution of T_G in the VB more closely than that of T_{max} at the selected latitudes (Fig. 28). These differences can be easily explained by the fact that even if the best latitudes were selected, a change of a few degrees north or southwards still has an impact on the temperature distribution. It is interesting, though, to note that the climate models all have the peak in their PDF for T_{max} at lower temperatures compared to the reanalyses, although many of them use a lower latitude for this calculation than the reanalyses (Table 8). As a consequence, only the mean and variance of the daily maximum thermal gradient in the VBs will be used in the following statistical assessment.

First, addressing the T_G means, a model will be considered as "close" if the value of its mean T_G is between those of the two reanalyses, illustrated by area between the red lines in Fig.

29. (A difference of 0.31 K km^{-1} is observed between the means of the maximum T_G of the two reanalyses.) A model will be considered “satisfactory” if its mean lies within the range delimited by the reanalyses means plus or minus their difference (i.e. between -0.31 and +0.62 K km^{-1}), as shown in blue on Fig. 29. Models whose mean lies outside these bounds are considered “distant”. On this basis, MRI, CSIRO, and GISSR models are “close”, MPI, MIROC, IPSL, CNRM and CCM models are “satisfactory”, and GFDL1 and GFDL2 models are “distant”.

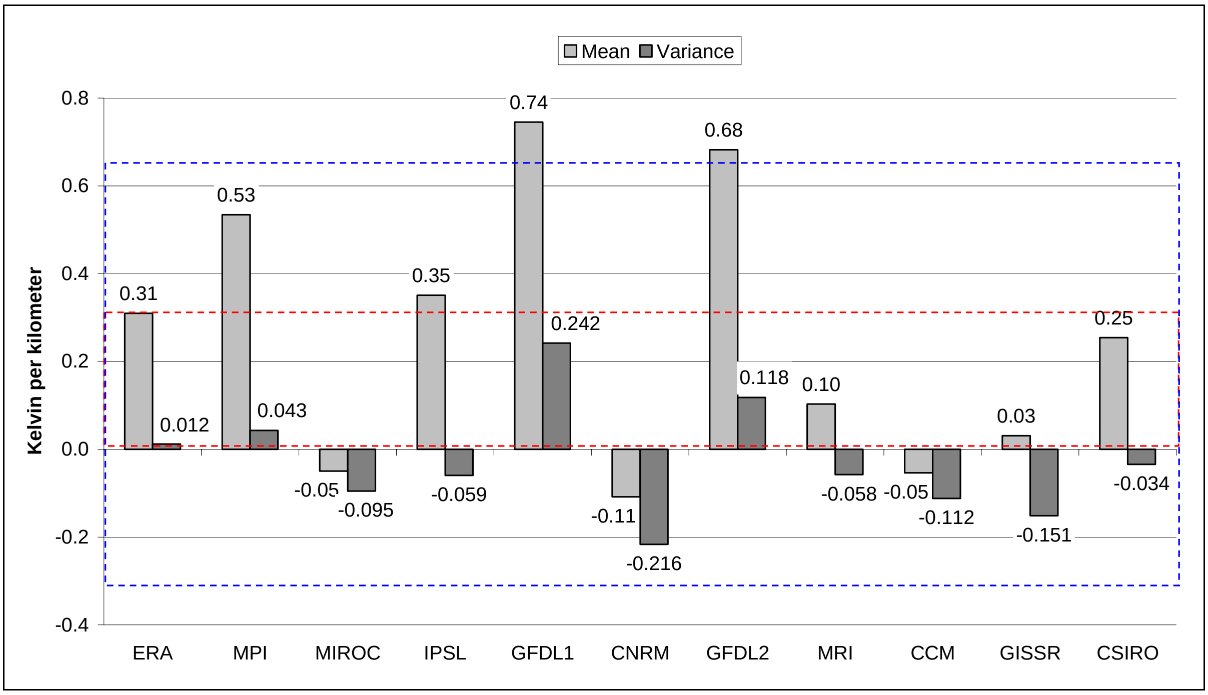

Figure 29: *Difference between NNR T_G mean and variance and those of ERA40 and the climate models. Boundary between values of “close” and “satisfactory” models is shown by the red dashed lines and between “satisfactory” and “distant” by the blue dashed lines.*

In attempting to apply the same methodology to the difference between the variances of the climate models and the variance difference between NNR and ERA40, we found that an alternative strategy was necessary as the difference between the NNR and ERA40 variance (Δ=0.012) is very small. We decided that a model would be considered as having a “distant” T_G distribution if the variance difference was more than 50% of the NNR variance, i.e. 0.157. This test adds the CNRM model to those considered distant, and the GFDL1 model also fails this test.

Earlier in this report we used the trend line slope of the scatter plots of T_G versus T_{max} to select the latitude at which T_{max} was calculated. There is still, however, considerable variation in this slope from model to model (Fig. 20 and Appendix 3). In Fig. 30 the difference of the slopes of the trend-lines in those scatter plots is compared with the difference between the NNR and ERA40 slopes. Applying a methodology analogous to that based on T_G (Fig. 30) and using the same colour-coding, adds the MIROC, CNRM, and GISSR models to the "distant" list, while GFDL1, GFDL2, CCM, and CSIRO models are rated as "close".

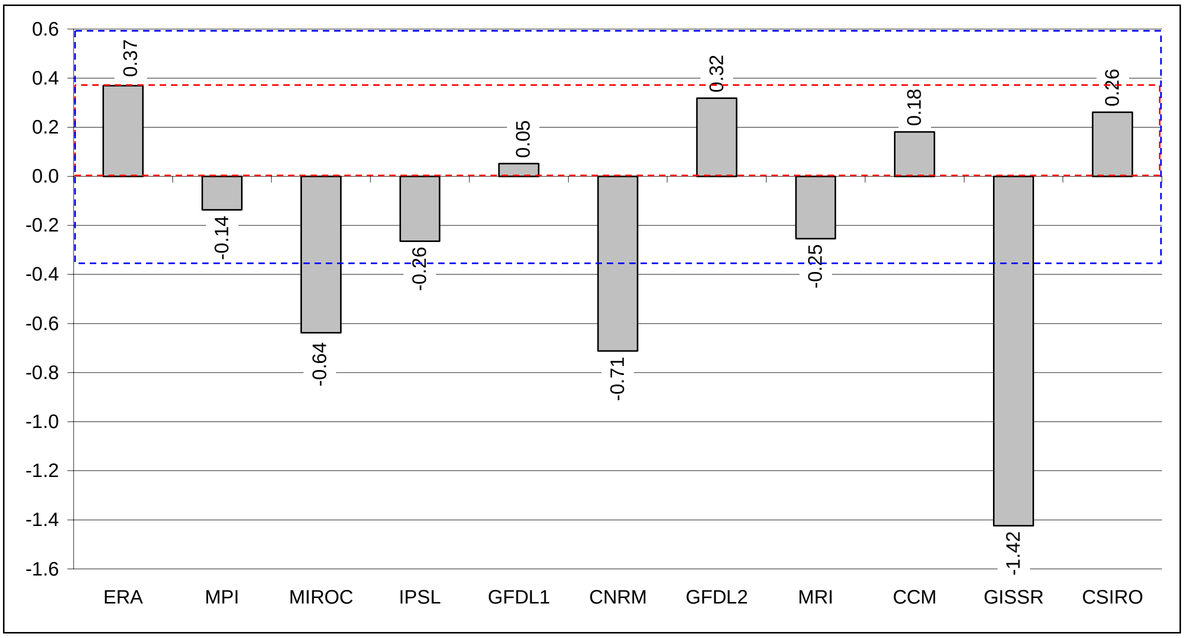

Figure 30: *Difference between the slopes of the linear regressions of the scatter-plots for the climate models and that of the NNR scatter plot.*

The outcome of these simple statistical tests is summarised in Table 10 below. Models MPI, IPSL, MRI, CCM, and CSIRO are rated as either satisfactory or close in each of the three tests, while MIROC, GFDL2, and GISSR models are rated as satisfactory or close in two of the three tests.

	MPI	MIROC	IPSL	GFDL1	CNRM	GFDL2	MRI	CCM	GISSR	CSIRO
Mean	S	S	S	D	S	D	C	S	C	C
Variance	C	S	S	D	D	S	S	S	S	S
Slope	S	D	S	C	D	C	S	C	D	C
Overall	**3**	**2**	**3**	**1**	**1**	**2**	**3**	**3**	**2**	**3**

Table 9: *Summary table of the simple tests on the distributions of the thermal gradient; iIn the overall assessment (bottom row) one point is given for close (C) or satisfactory (S), no points for distant (D).*

Higher order statistical tests

Simple statistical tests such as the comparison of mean and standard deviation do not explore the entire data distribution, and indeed the accurate reproduction of the mean and variance of T_G does not necessarily show that the model PDFs have reliable higher order moments. However, it is perhaps these higher order moments that are more important for the extreme cases that are the focus of this investigation. Consequently, an attempt is made to use higher-level statistical tests to strengthen our evaluation of the models. Two tests, both based on the whole data probability PDFs, have been performed for our model evaluation analysis; the Kolmogorov-Smirnov (KS) test and a recent test proposed by Perkins et al. (2007). In these methods the model PDFs are tested against both reanalyses, using the difference between the reanalyses as an estimation of the uncertainty and thus as a proxy for how the climate models reproduce the higher order moments of the PDFs of T_G.

We first use the KS test to assess by how much the models' distributions differ from those of the reanalyses. Unlike most of the goodness-of-fit tests, this test makes no assumptions about the distribution of the data. The KS test computes the D-statistic, which is the maximum vertical deviation between two sets of data cumulative fraction plots. This test assesses the differences in shape and location of the cumulative distribution functions of the two datasets. The best skill score for the KS test corresponds to the smallest value of its D statistic. Due to the dependence of the T_{max} distribution on latitude (see above), the KS test was only applied to the maximum thermal gradient (T_G) distributions over the defined VBs, using the statistical package R. The D statistic has been calculated with respect to both reanalyses and therefore the test gives two values per model (Fig. 31).

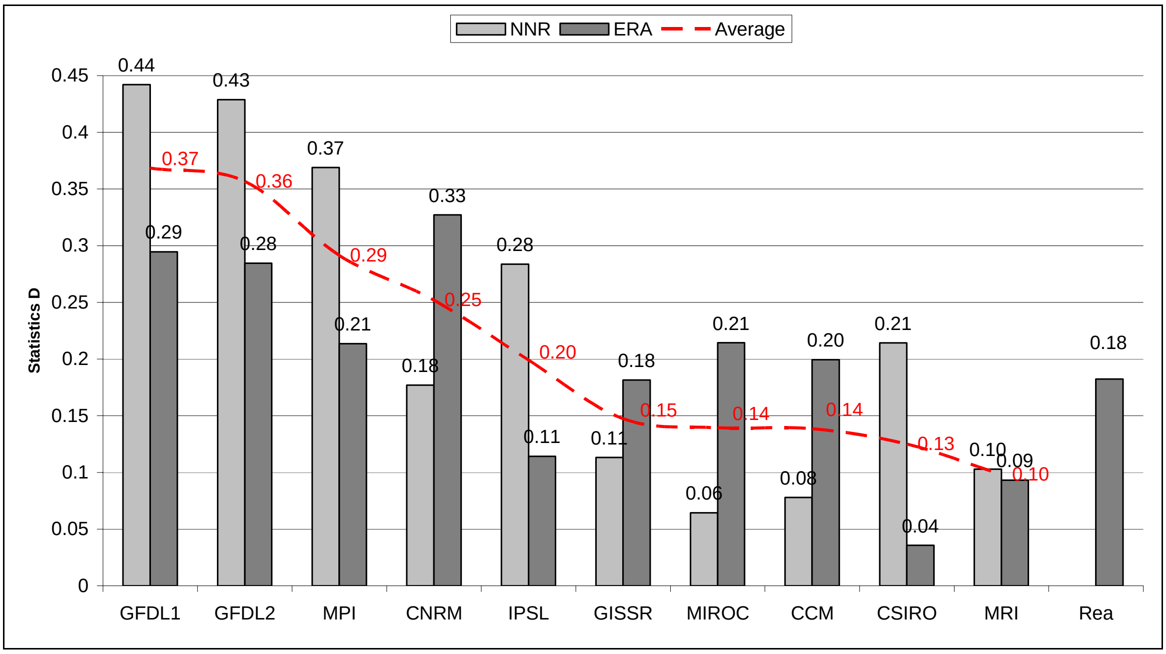

Figure 31: *Kolmogorov-Smirnov test results ("D value") for each of the climate models using both NNR and ERA40 as control sets. The average values are linked with a dashed curve. The bar "Rea" corresponds to the K-S test result for the reanalyses.*

The test was also performed to compare the two reanalysis data sets, resulting in a D statistic of 0.18, and this value will be used as the critical value for the climate model comparison. Averaging the two D statistics for each model (red figures and curve in Fig. 31) provides a basis on which each model can be compared with the reanalysis D value. In this test we regard those models whose D statistic is lower than that of the reanalyses as being close, while those whose D is greater than 1.5 times D_{rea} will be classed as distant. On this basis, MRI, CSIRO, CCM and MIROC models are close, CNRM and IPSL models are satisfactory, and GFDL1, GFDL2, and MPI models are distant.

Perkins et al. (2007) proposed an alternative way to objectively assess the ability of models to reproduce PDFs of selected observed parameters. Stating that "it is not clear how to sum across […] PDF-based statistics", he proposed a new methodology measuring the common area under the PDFs of the control and assessed datasets. This test gives each model a skill score (SS), with a SS of one indicating two identical frequency distributions. The SS is defined as:

$$S_{Score} = \sum_{1}^{n} \min(Z_m, Z_0)$$

Where n is the number of bins used to calculate the PDF for a given region, Z_m is the frequency of values in a given bin from the model, and Z_0 is the frequency of values in a given bin of observed data. As we consider the reanalyses as being two equivalently plausible versions of the observed data, two SS were computed for each model (Fig. 32). The models' average SS have been ranked in increasing order in Fig. 32. There are no particularly obvious "break points" in this series, but if the reanalyses SS of 0.83 is used as a criterion for classing a particular model as "close" then MRI, CSIRO, CCM and MIROC meet this criterion, while GFDL1, GFDL2, and CNRM models are distant.

Interestingly, apart from exchanging the positions of the CNRM and MPI models, the ordering of the models is the same using both the KS and the Perkins D tests (Figs. 31, 32).

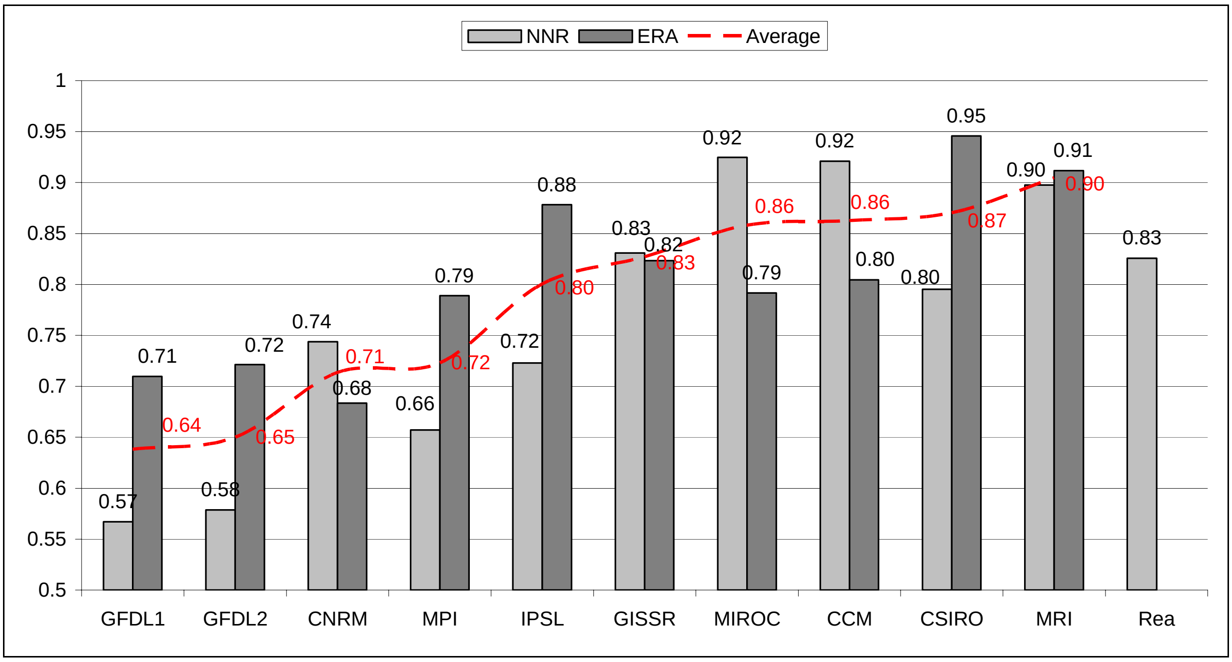

Figure 32: *Results for the Skill Score test (Perkins et al. 2007) for each climate model using both NNR and ERA40 as control sets. The average values are linked with a dashed curve. The bar "Rea" corresponds to the SS of the reanalyses.*

b) Summary - evaluation of the models

Combining the results of the simple and the higher order statistics tests (Table 10), it is found that only the CCM, CSIRO, and MRI models satisfied all our criteria, while the GFDL1, GFDL2, and CNRM models were most distant from the reanalyses on most of our tests. In the discussion of future climate change scenarios all models will be included, but each of these model groupings will be differentiated.

	CCM	CSIRO	CNRM	GFDL1	GFDL2	GISSR	IPSL	MIROC	MPI	MRI
Simple stats tests	C	C	D	D	S	S	C	S	C	C
High level stats tests	C	C	D	D	D	S	S	S	S	C

Table 10: *Summary of the results of all tests for all models; a C represents a close match, an S a satisfactory match, and D a distant match to the reanalysis climate.*

8) Projections of climate model diagnostics over the twenty-first century

The principal aim of the present study is to assess the possible impact of climate change on the evolution of fire weather systems linked with very high fire danger, and for the purposes of this study these are defined as those days on which threshold values of both T_G and T_{max} are exceeded. In this section we first re-visit the temperature projections expected by the various climate models over southeastern Australia through the 21st century under varying emissions scenarios, and then examine the trends in the number of "strong cold front" days under the low-impact (B1) and high impact (A2) scenarios for two twenty-year periods centred on 2050 and 2090. In making this analysis we are assuming that the threshold defining an extreme fire day will remain unchanged, and that therefore any changes in the number of days on which both T_G and T_{max} thresholds are exceeded equate to changes in frequency of these extreme fire weather frontal passages.

a) Temperature projections

Many studies have been undertaken in order to evaluate the change in temperature for the twenty first century, both over the whole globe and also on continental and regional scales. The CSIRO and Bureau of Meteorology (2007) projections show an increase of the summer temperature of less than 2ºC over southeast Australia at 2030 for all scenarios, but by 2070 only the low emissions scenario (B1) shows temperature increases of less than 2ºC. The projected increase in summer temperature under the high emissions scenario is greater than 3ºC by 2070 over most of the Victorian region (Fig. 33). In this diagram only the B1, A1B and A1Fl scenarios are shown. However, the climate response under the A2 scenario is similar to that of A1B for 2050 and to that of A1Fl for 2070. Consequently, an increase of more than 3ºC is expected for scenario A2 by the end of the twenty-first century.

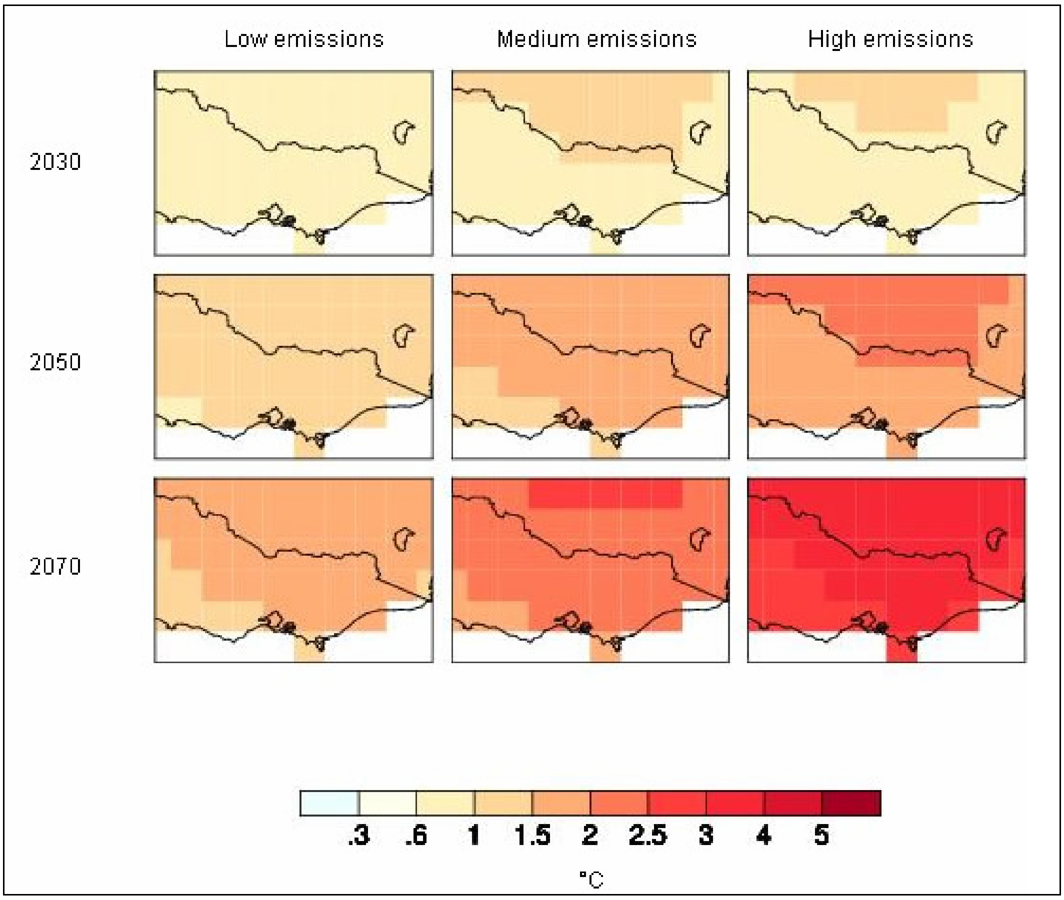

Figure 33: *Projected 50th percentile Victorian summer temperature change relative to the period 1980-1999 at 2030, 2050 and 2070 under the low, medium and high emissions scenarios, corresponding respectively to the B1, A1B and A1FI SRES scenarios (CSIRO and Bureau of Meteorology 2007).*

Figure 34 shows an example of a scatter plot of T_G vs. T_{max} under these climate change scenarios. Displayed are the results for the 20th century, the A2 scenario around 2090 and their respective trend lines for model MRI. The slope of the trend line is virtually identical, but is displaced to higher temperatures under the different emissions scenarios and time extrapolations, consistent with the discussion of Fig. 33. It should be noted that there is also a larger number of high T_G values under the more extreme scenario.

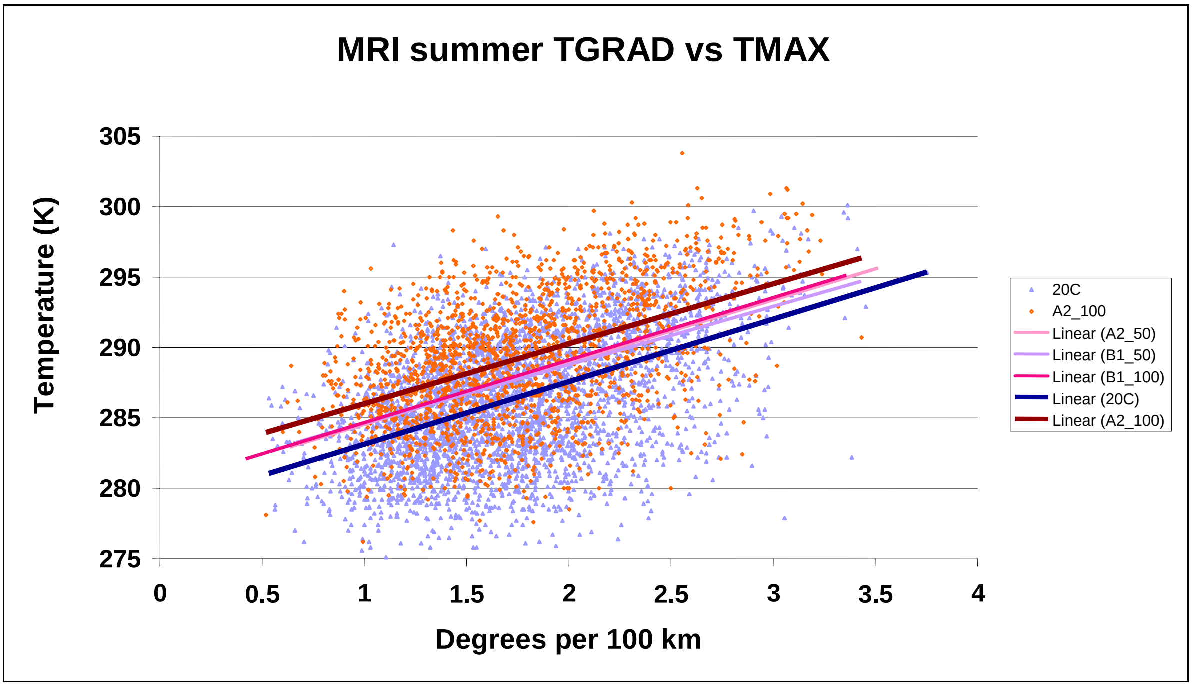

Figure 34: *As Figure5 but for the MRI model (blue dots), with the values for 2081-2100 displayed as orange.; linear regressions for the period 1964-2000 and for the high and low emissions scenarios over the periods 2046-2065 and 2081-2100 are also shown.*

b) Changes in frequency of extreme events

In this section we first present results for the three models which best match the reanalyses' climate during the 20th century (MRI, CCM, and CSIRO). We will then extend the analysis to all models to broaden the perspective on the uncertainties in these projections.

The three "close" models all show an increase in the occurrence of the class of extreme events addressed in this report over the 21st century (Fig. 35), although there is a great difference in the amplitude of the signal between the two scenarios. All three models show an increased frequency of extreme events under the B1 scenario by the middle of the 21st century. This frequency then declines slightly towards the end of the 21st century, but still ranges between 13 and 99% greater than during the late 20th century. Under the A2 scenario, there is change of between -25% and 102% by the middle of the 21st century, and between 77 and 312% increase by the end of the 21st century.

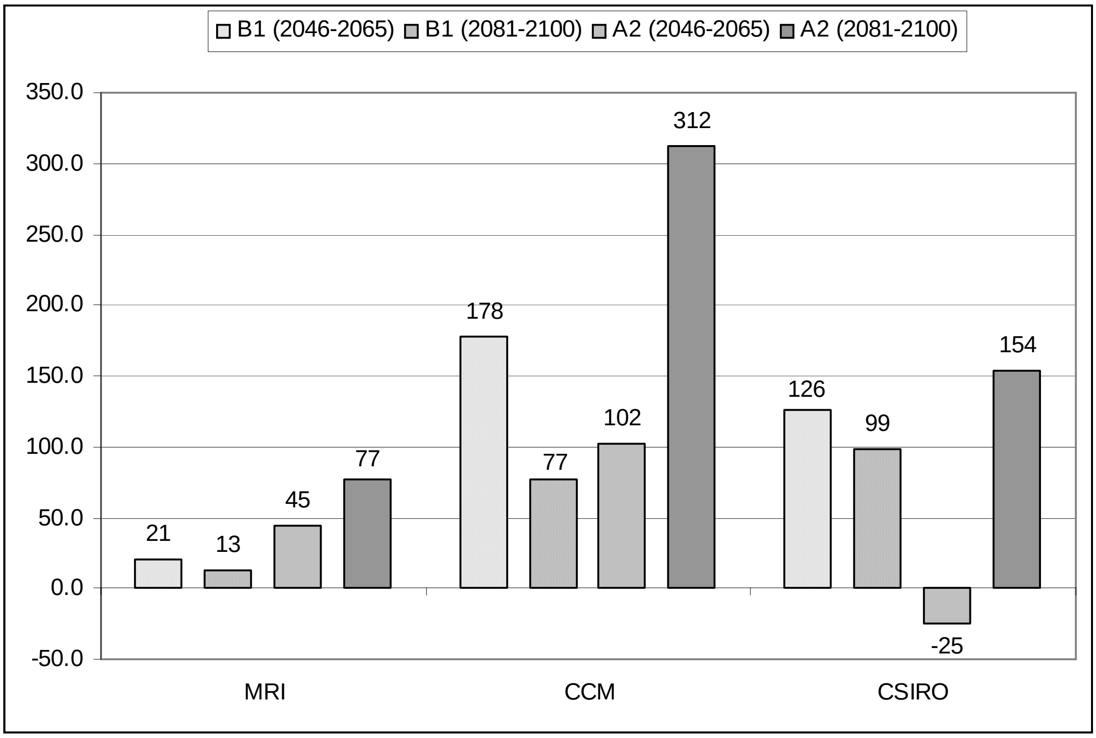

Figure 35: *Percentage change in the number of extreme cases per decade from the 20th century to the periods (2046-2065) and (2081-2100), for the low and high emissions scenarios for the three models whose 20th century climate is closest to that of the reanalyses.*

The three models whose projections are summarised in Fig. 35 are those whose T_G/T_{max} climates of the 20th century are closest to those of the reanalyses using the statistical tests described in the previous section. Therefore the projections from these models might be hypothesised to be "more reliable" than the other models (Whetton et al. 2007); however, such a judgement must be treated with some caution, and it can be argued that there is value in presenting the trends for all the available climate models. These trends are shown in Fig. 36 for B1 and A2 scenarios in terms of number of events per year. The three models whose climates are closest to the reanalyses are in bold, and the three whose climates are most distant are shown in dashed lines. For the B1 scenario there is considerable qualitative consistency in the projections, with all models showing an increase in the number of events per year during the first half of the 21st century, and all but one (IPSL) then showing a decrease in numbers towards the end of the 21st century, but with an increasing spread in the potential numbers. Under the A2 scenario, all models show an increase in the number of events during the first half of the 21st century, and an even greater increase in the next 50 years. Even if the IPSL model (the model showing the most extreme rate of increase) is excluded, the mean number of events per year changes from 0.59 (C20C) to 0.93 (1.04) by the middle of the 21st century for the B1 (A2) scenarios, and to 0.94 (1.54) by the end of the 21st century.

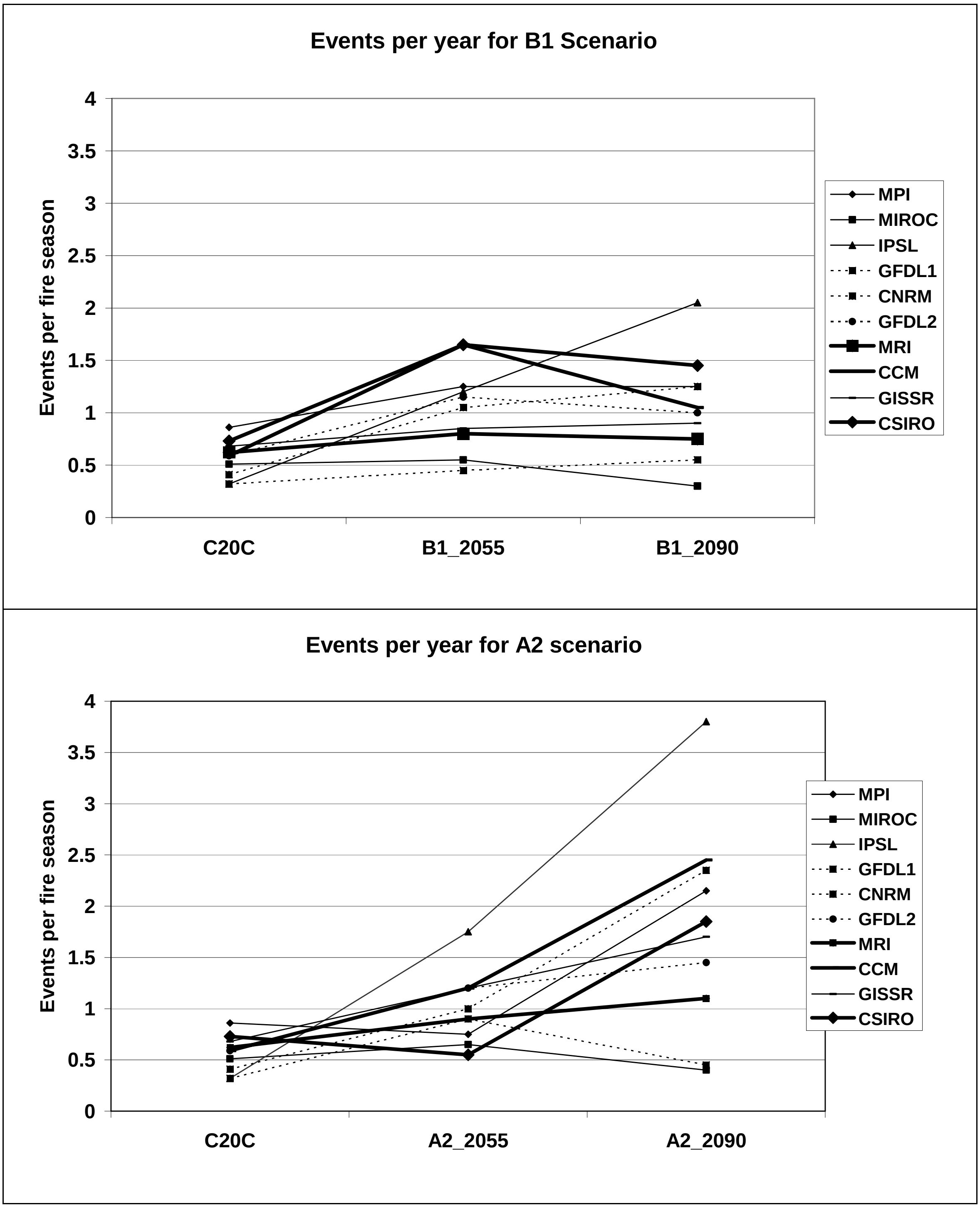

Figure 36: *Number of extreme fire weather frontal events per season for the climate of the 20th century (C20C), for the 2046-2065 period (_2055), and for the 2080-2100 period (_2090). Upper panel shows projections for the B1 emissions scenario, and the lower panel for the A2 scenario. The heavy lines are for the three "close" models, while the dashed lines are for the three "distant" models.*

Summary and future Work

This study has investigated the change of the occurrence of extreme fire danger days through the twenty-first century by use of a proxy adapted from Mills (2005) which assesses the evolution of the incidence of a particular synoptic situation shown to be linked to historical disastrous fires. The information gained from such research is vital for evaluating and planning future changes needs in fire fighting resources in the South-east of Australia for the next century.

The research results reveal an increasing danger under climate change conditions for both of the two contrasting scenarios investigated. The models selected by our analysis show under the low and high emissions scenarios an increase of respectively -41-208% and -22-1072% in the number of cases of potential fire weather by the end of the twenty-first century. Excluding the one model that showed a far stronger trend than the others, these percentage increases equate to a change from around one event every two years during the 20th century, to around 1 event per year in the middle of the 20th century, and 1-2 events per year by the end of the 21st century, but with a great degree of variation between models. In addition to a greater overall increase under the high emissions scenario, the rate at which the increase occurs amplifies during the second half of the century, whereas under the low emissions scenario, the number of extreme cases stabilizes.

Previous studies (Hennessy et al. 2005, Lucas et al. 2007) investigated the evolution of occurrence of extreme fire danger days through FFDI statistics for southeast Australia. Hennessy et al. (2005) found a potential increase of Very High and Extreme FFDI days by 15-70% by 2050. Since our study used a different methodology, it adds to the consensus regarding future increased fire danger.

The difference in the overall increase of the number of extreme danger episodes between the two emissions scenarios, and between the different models, should be taken in account when interpreting the large relative increases that some models predict by the end of the twenty-first century under the high emissions scenario. It must also be remembered that the results are to some extent dependent on the methodology used.

Further work is suggested to strengthen the methodology used to select the days with extreme fire danger conditions, possibly by looking at the meridional and zonal components of the thermal gradient. It is also recommended to extend the analysis of the impact of the model characteristics, such as the land-sea masks, on the results. Furthermore, the diagnostic tool could be adapted to other regions of Australia and the world, although as noted in Mills (2005) the particular configuration of the southeastern Australian coastline may make the methodology, at the very least, more applicable there than in other areas.

Acknowledgements

This report is based on the senior author's Honours Thesis at the University of Melbourne. We wish to thank Ian Smith, Elodie Fernandez and other BMRC staff members for sharing their knowledge and experience during the progress of the research. The senior author also thanks the Bureau of Meteorology for receiving her in their Head Office during 2007, and for providing the computer facilities needed to achieve the research. To conclude, the modeling groups concerned are thanked for making their simulation results available and the Program for Climate Model Diagnostics and Intercomparison at Lawrence Livermore National Laboratory for compiling and providing access to these results.

References

Bond, H.G., McKinnon, K., and Noar, P.E., 1967. Report on the meteorological aspects of the catastrophic bushfires in south-eastern Tasmania on 7 February 1967. Bureau of Meteorology, Australia, 54pp.

Bromwich D.A., and R.L. Fogt, 2004, Strong trends in the skill of the ERA-40 and NCEP-NCAR Reanalyses in the high and mid-latitudes of the southern Hemisphere, 1958-2001. *Journal of Climate*, 17, 4603-4619

Bureau of Meteorology 1984. Report on the meteorological aspects of the Ash Wednesday fires – 16 February 1983. Bureau of Meteorology, Australia, 143pp.

Bureau of Meteorology, 2003. Meteorological aspects of the eastern Victorian fires January-March 2003. Bureau of Meteorology, Victoria. 82pp

Caya, D., Laprise, R., Giguere, M., Bergeron, G., Blanchet, J.P., Stocks, B.J., Boer, G.J. & McFarlane, N.A., 1995. Description of the Canadian regional climate model, *Water Air and Soil Pollution,* 82**,** 477-482.

Cheney, P., and Sullivan, A., 1997. Grassfires : fuel, weather and fire behaviour. CSIRO Publishing, 102pp.

Cheney, P., Gould,J., and McCaw,L. 2001. The Dead Man Zone – A neglected area of firefighter safety. *Australian Forestry 64*, 45-50.

Crimmins, M.A., 2006. Synoptic climatology of extreme fire-weather conditions across the southwest United States, *International Journal of Climatology,* 26**,** 1001-1016.

CSIRO & Bureau of Meteorology, 2007. Climate change in Australia : Technical report 2007, pp. 148, Australian Commonwealth Scientific and Industrial Research Organization; Bureau of Meteorology, Australia. (www.climatechangeinaustralia.com).

Deeming, J.E., Burgan, R.E. & Cohen, J.D., 1977. The National Fire-Danger Rating System-1978. *in USDA For. Serv. Intermt. For. and Range Exp. Stn.*Utah. Gen. Tech. Rep., Ogden.

deGroot, W.J., Wardati, and Wang, Y., 2005. Calibrating the Fine Fuel Moisture Code for grass ignition potential in Sumatra, Indonesia. *Int, J. Wildland Fire 14*, 161-168.

Dudfield, M., 2004. Art and Science of Forest and Rural Fire Management. Proceedings AFAC/Bushfire CRC Annual Conference, Perth, October 2004. Pp 183-185.

Finkele,K., G.A.Mills, G. Beard,and D. Jones, 2006. National daily grided soil moisture deficit and drought factors for use in prediction of Forest Fire Danger Index in Australia. BMRC Research Report No 119. 68pp.

Griffith, D., 1999. Improved formula for the drought factor in McArthurs Forest Fire Danger Meter. *Australian Forestry,* 62**,** 202-206.

Haines, D.A., 1988. A lower atmosphere severity index for wildland fires, *National Weather Digest,* 13**,** 23-27.

Hennessy, K., Lucas, C., Nicholls, J.B., Suppiah, R. & Ricketts, J., 2005. Climate change impacts on fire-weather in south-east Australia, pp. 88, Commonwealth Scientific and Industrial Research Organisation Australia.

Hughes, L., 2003. Climate change and Australia: Trends, projections and impacts, *Austral Ecology,* 28**,** 423-443.

IPCC, 2001. Climate Change 2001: The Scientific Basis. Contribution of Working Group I to the Third Assessment Report of the IPCC, pp. 881, eds Houghton, J. T., Ding, Y., J., G. D., Noguer, M., van der Linden, P. J., Dai, X., Maskel, K. & Johnson, C. A. Cambridge University Press, Cambridge, Cambridge, United Kingdom and New York, NY, USA.

IPCC, 2007. Climate Change 2007: The Physical Science Basis. Contribution of Working Group I to the Fourth Assessment Report of the IPCC, pp. 996, eds Solomon, S., Qin, D., Manning, M., Chen, Z., Marquis, M., Averyt, K. B., Tignor, M. & Miller, H. L. Cambridge University Press,, Cambridge, United Kingdom and New York, NY, USA.

Kallberg, P., Berrisford, P., Hoskins, B., et al. 2005. ERA-40 Atlas, ERA-40 Project Report Series, No 19. European Centre for medium Range Weather Forecasts.

Kalnay, E., Kanamitsu, M., Kistler, R., Collins, W., Deaven, D., Gandin, L., Iredell, M., Saha, S., White, G., Woollen, J., Zhu, Y., Chelliah, M., Ebisuzaki, W., Higgins, W., Janowiak, J., Mo, K.C., Ropelewski, C., Wang, J., Leetmaa, A., Reynolds, R., Jenne,

R. & Joseph, D., 1996. The NCEP/NCAR 40-year reanalysis project, *Bulletin of the American Meteorological Society,* 77**,** 437-471.

Keetch, J.J. & Byram, G.M., 1968. A drought Index for Forest Fire Control, pp. 32U.S. Department of Algriculture-Forest Service, Asheville, NC.

Long, M., 2006. A climatology of extreme fire weather days in Victoria, *Australian Meteorological Magazine,* 55**,** 3-18.

Lucas, C., K. Hennessy, G.Mills and J.Bathols 2007. Bushfire weather in southeast Australia: recent trends and projected climate change impacts. Consultancy Report prepared for the Climate Institute of Australia. Bushfire Cooperative Research Centre, 81pp.

Luke, R.H. and McArthur, A.G., 1978. Bushfires in Australia. Australian Government Publishing Service, Canberra. 359pp.

Manabe, S. & Wetherald, R.T., 1975. The Effects of Doubling the CO2 Concentration on the climate of a General Circulation Model, *Journal of the Atmospheric Sciences,* 32**,** 3-15.

McArthur, A.G., 1967. Fire behaviour in eucalypt forest. *in Comm. Aust. For. Timb. Bur. Leaflet*, pp. 25.

McCaw, L., Marchetti, P., Elliott, G., Reader, G. 2007. Bushfire weather climatology of the Haines Index in south-western Australia. *Aust Meteor. Mag. 56*, 75-80.

McGregor, J.L. & Dix, M.R., 2001. The CSIRO conformal-cubic atmospheric GCM. *in IUTAM Symposium on Advances in Mathematical Modeling of Atmosphere and Ocean Dynamics*, pp. 197-202.

Mills, G.A., 2005. A re-examination of the synoptic and mesoscale meteorology of Ash Wednesday 1983, *Australian Meteorological Magazine,* 54**,** 35-55.

Nakicenovic, N., Alcamo, J., Davis, G., de Vries, B., Fenhann, J., Gaffin, S., Gregory, K., Grubler, A., Jung, T.Y., Kram, T., La Rovere, E.L., Michaelis, L., Mori, S., Morita, T., Pepper, W., Pitcher, H.M., Price, L., Riahi, K., Roehrl, A., Rogner, H.-H., Sankovski, A., Schlesinger, M., Shukla, P., Smith, S.J., Swart, R., van Rooijen, S., Victor, N. & Dadi, Z., 2000. *Special Report on Emissions Scenarios : a special report of Working Group III of the Intergovernmental Panel on Climate Change,* pp. 27, Cambridge University Press, New York, United States.; Pacific Northwest

National Laboratory (PNNL), Richland, WA (US), Environmental Molecular Sciences Laboratory (EMSL), United States.

Noble, I.R., Bary, G.A.V. & Gill, A.M., 1980. McArthur Fire-danger meters expressed as equations, *Australian Journal of Ecology,* 5**,** 201-203.

Perkins, S.E., Pitman, A.J., Holbrook, N.J. & McAneney, J., 2007. Evaluation of the AR4 Climate Models; Simulated Daily Maximum Temperature, Minimum Temperature, and Precipitation over Australia Using Probability Density Functions, *Journal of Climate,* 20**,** 4356-4376.

Purton, C.M., 1982. Equations for the McArthur Mk 4 Grassland fire danger metre. *in Meteorological Note 147.* Bureau of Meteorology, Australia. 12pp.

Randall, D.A., Wood, R.A., Bony, S., Colman, R., Fichefet, T., Fyfe, J., Kattsov, V., Pitman, A., Shukla, J., Srinivasan, J., Stouffer, R.J., Sumi, A. & Taylor, K.E., 2007. Cilmate Models and Their Evaluation. In: Climate Change 2007: The Physical Science Basis. Contribution of Working Group I to the Fourth Assessment Report of the Intergovernmental Panel on Climate Change, pp. 74, eds Solomon, S., Qin, D., Manning, M., Chen, Z., Marquis, M., Averyt, K. B., Tignor, M. & Miller, H. L. Cambridge University Press, Cambridge, United Kingdom and New York, NY, USA.

Seaman, R.S., Falconer, R.L. & Brown, J., 1977. Application of a variational blending technique to numerical analysis in the Australian region. *Aust. Meteor. Mag. 25*, 3-23.

Stocks, B.J., Lawson, B.D., Alexander, M.E., Vanwagner, C.E., McAlpine, R.S., Lynham, T.J. & Dube, D.E., 1989. The Canadian Forest Forest Fire Danger Rating System – An overview, *Forestry Chronicle,* 65**,** 450-457.

Tymstra, C. & Armitage, B., 2005. Impact of climate change on area burned in Alberta's boreal forest (http://ams.confex.com/ams/pdfpapers/104604.pdf).

Viegas, D.X., Bovio, G., Ferreira, A., Nosenzo, A., and Sol., B., 1999. Comparative study of various methods of fire danger evaluation in southern Europe. *Int. J. Wildland Fire 9*, 235-246.

Watterson, I.G., Dix, M.R., Gordon, H.B. & McGregor, J.L., 1995. The CSIRO 9-level atmospheric general circulation model and its equilibrium present and doubled CO2 climates, *Aust. Meteor. Mag.,* 44**,** 111-125.

Whetton, P., Macadam, I., Bathols, J. & O'Grady, J., 2007. Assessment of the use of current climate patterns to evaluate regional enhanced greenhouse response patterns of climate models, *Geophysical Research Letters,* 34**,** 5.

Williams, A.A.J., Karoly, D.J., and Tapper, N., 2001. The Sensitivity of Australian Fire Danger to Climate Change, *Climatic Change,* 49**,** 171-191.

Xiao-Rui, T., McRae, D.J., Boychuk, D., JiZhong, J., ChengDa, G., Lifu, S. & MingYu, W., 2005. Comparisons and assessment of forest fire danger systems, *Forestry Studies in China,* 7.

Appendix 1

Maps of the temperature field at 850hPa for the 10 models on the 2 extreme case days following the 01/01/1964 picked by the second “threshold methodology”.

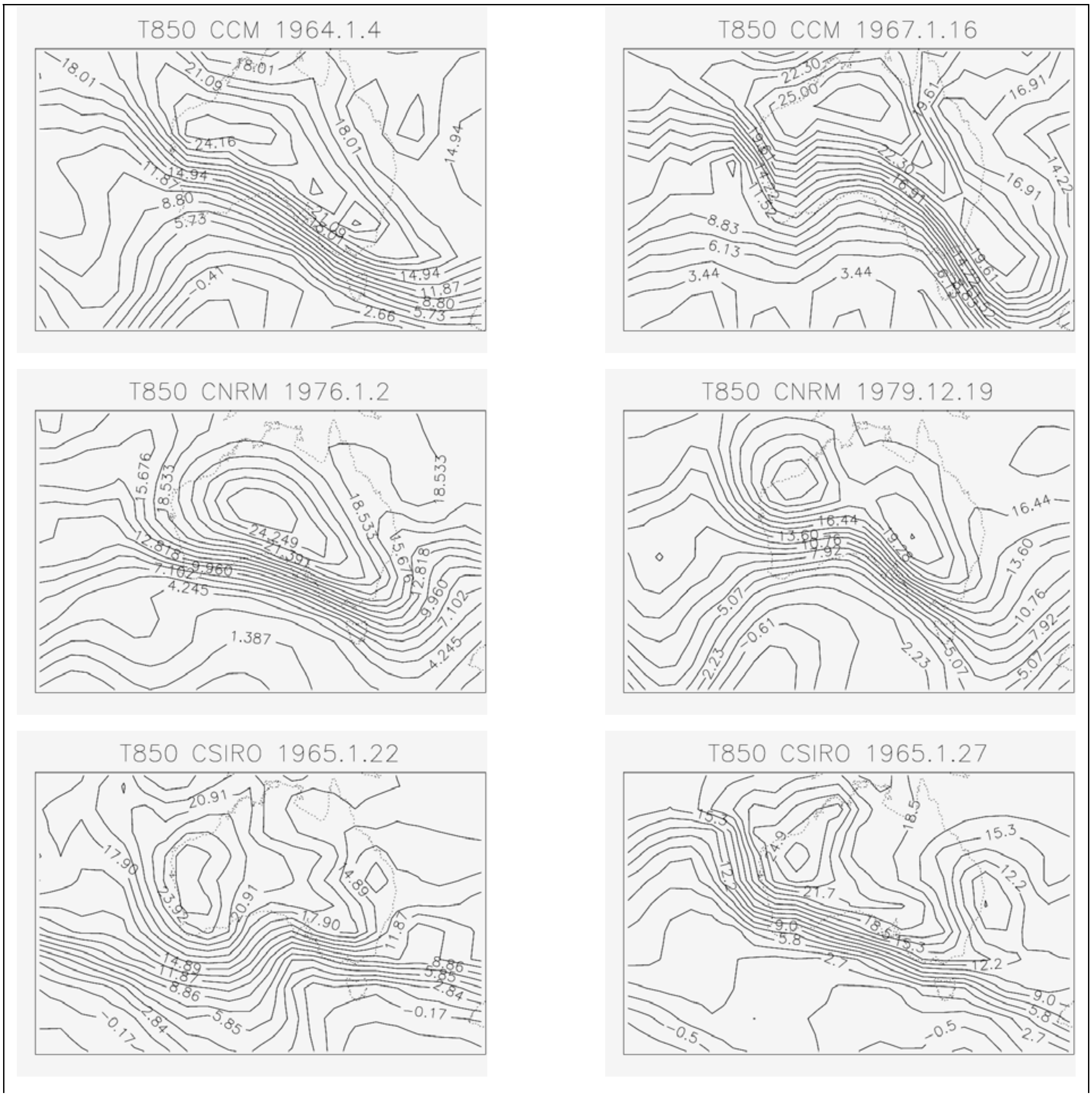

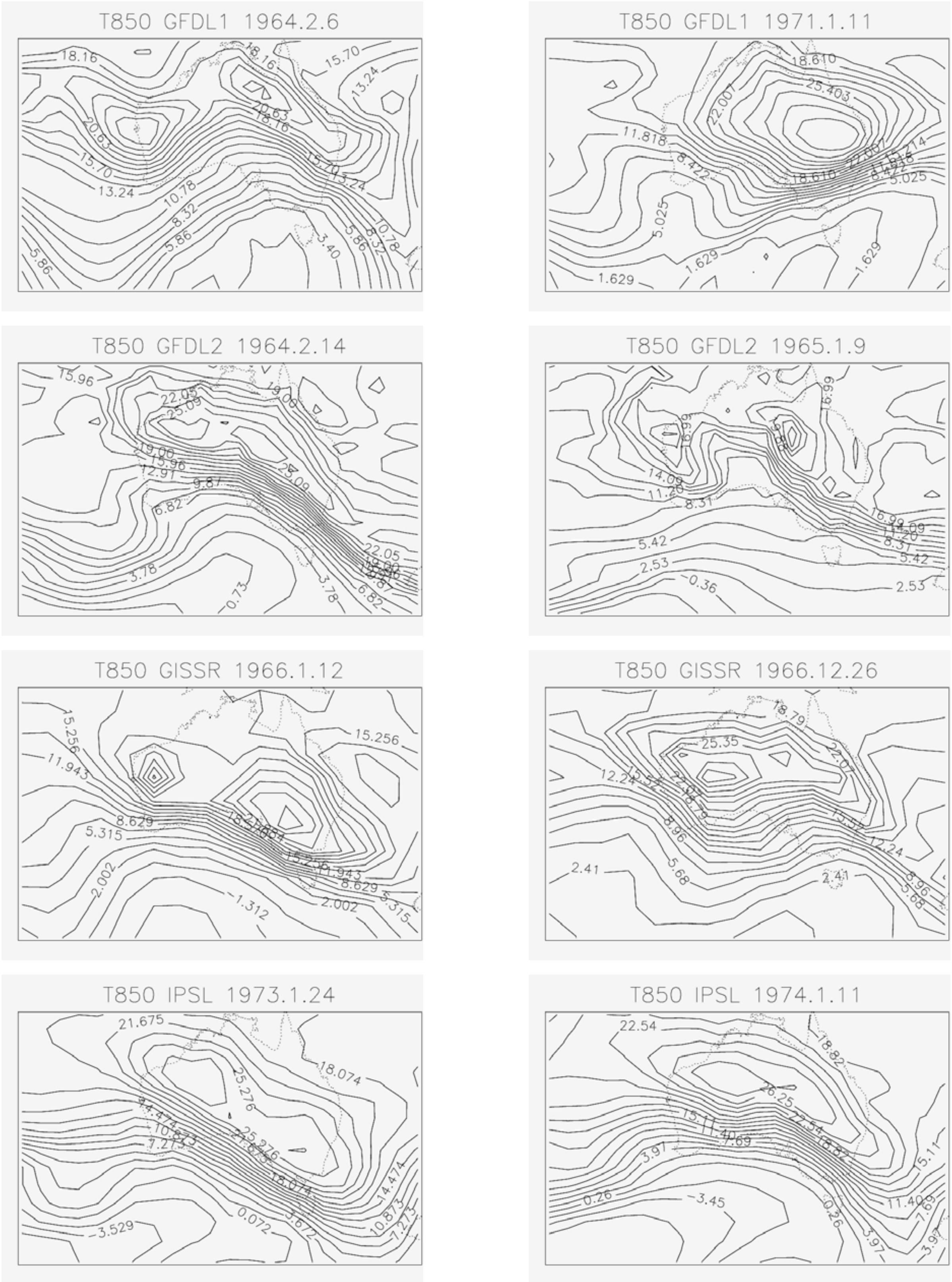
T850 GFDL1 1964.2.6
T850 GFDL1 1971.1.11
T850 GFDL2 1964.2.14
T850 GFDL2 1965.1.9
T850 GISSR 1966.1.12
T850 GISSR 1966.12.26
T850 IPSL 1973.1.24
T850 IPSL 1974.1.11

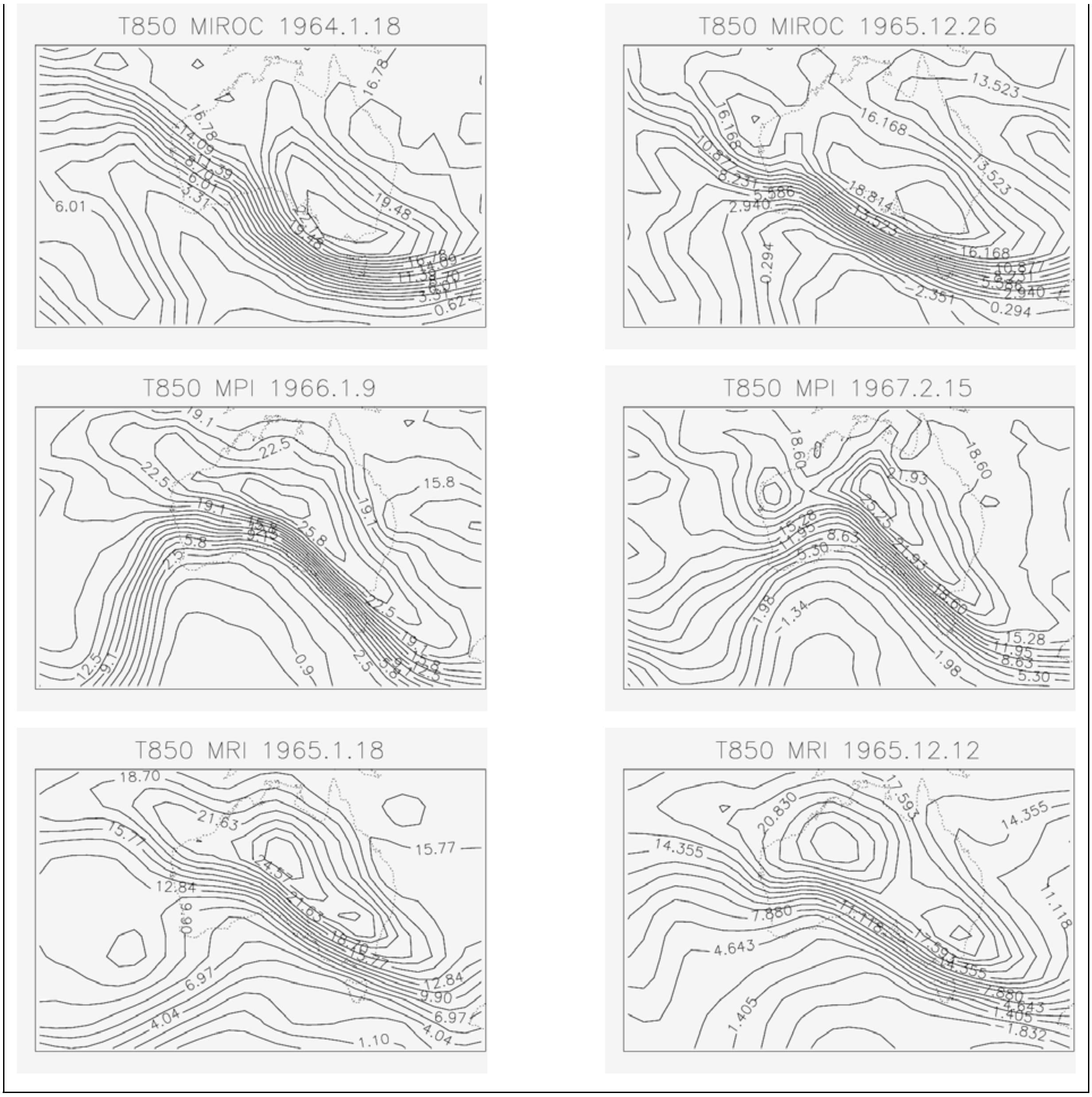
T850 MIROC 1964.1.18
T850 MIROC 1965.12.26
T850 MPI 1966.1.9
T850 MPI 1967.2.15
T850 MRI 1965.1.18
T850 MRI 1965.12.12

Appendix 2

Land-sea masks of each model and reanalysis over southeast Australia. The dashed box is the original Victorian Box (i.e. the reanalyses' one) and the dotted boxes are the Victorian boxes specific to each model. The solid lines are the latitudes along which T_{max} is selected, listed in Table 7.

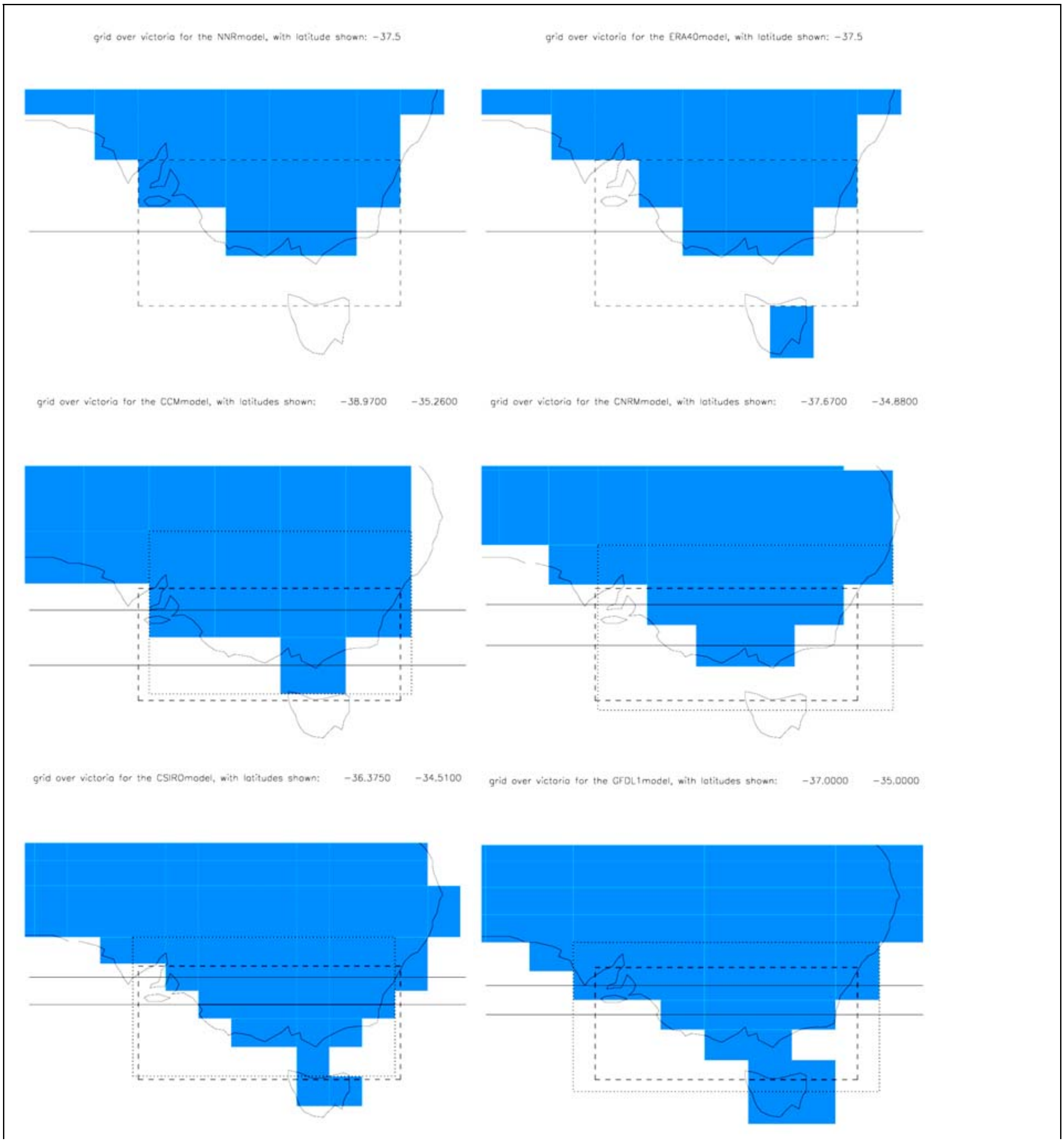

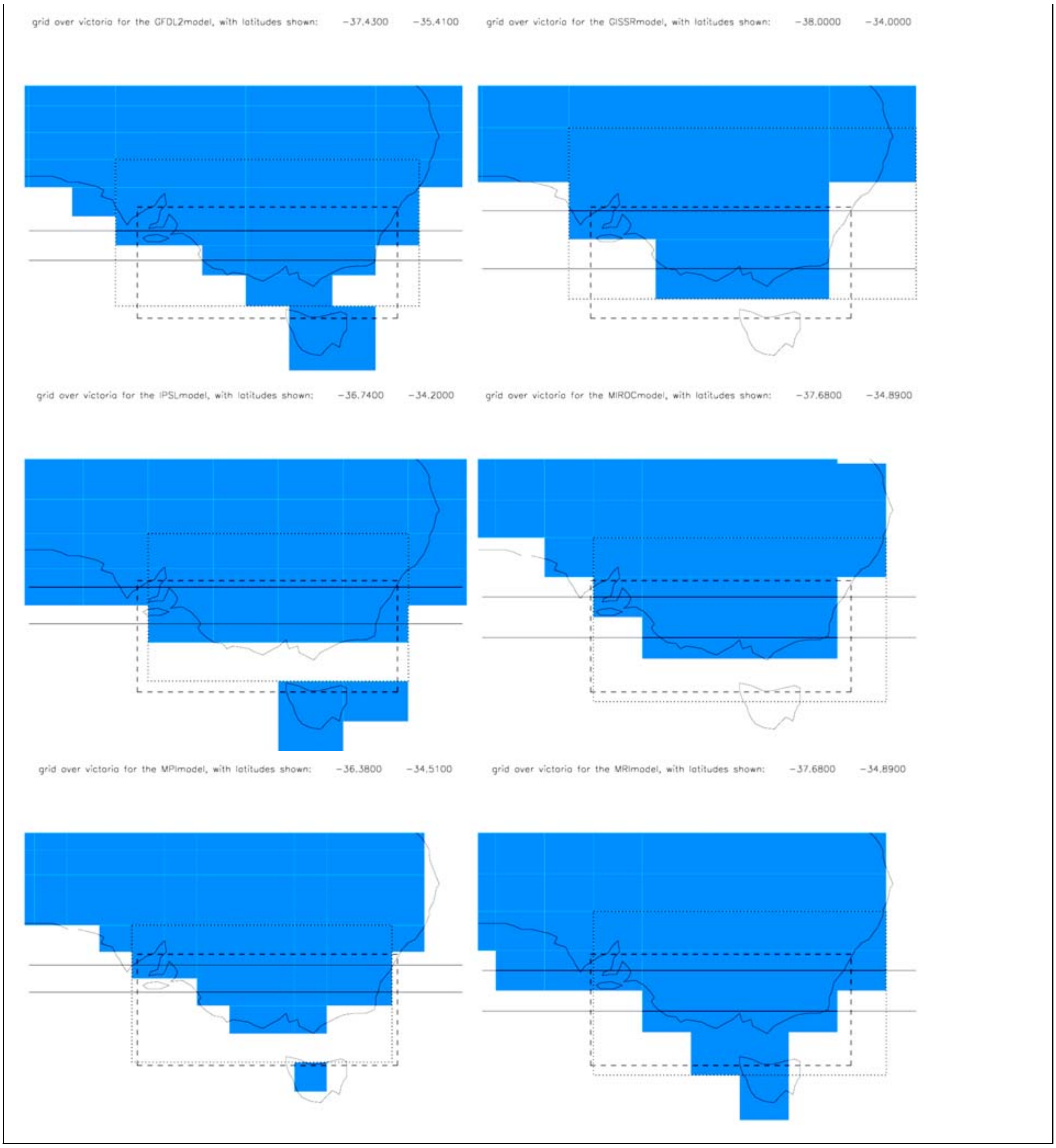
grid over victoria for the GFDL2model, with latitudes shown: −37.4300 −35.4100
grid over victoria for the GISSRmodel, with latitudes shown: −38.0000 −34.0000
grid over victoria for the IPSLmodel, with latitudes shown: −36.7400 −34.2000
grid over victoria for the MIROCmodel, with latitudes shown: −37.6800 −34.8900
grid over victoria for the MPImodel, with latitudes shown: −36.3800 −34.5100
grid over victoria for the MRImodel, with latitudes shown: −37.6800 −34.8900

Appendix 3

Scatter-plot for each model (Table 7) set and its linear regression (solid red line) of the 850hPa maximum thermal gradient versus the maximum temperature on the “northern” and “southern” latitudes (Table 7) over the model’s Victorian Box at 0000 UTC during summer for the period 1964-2000.

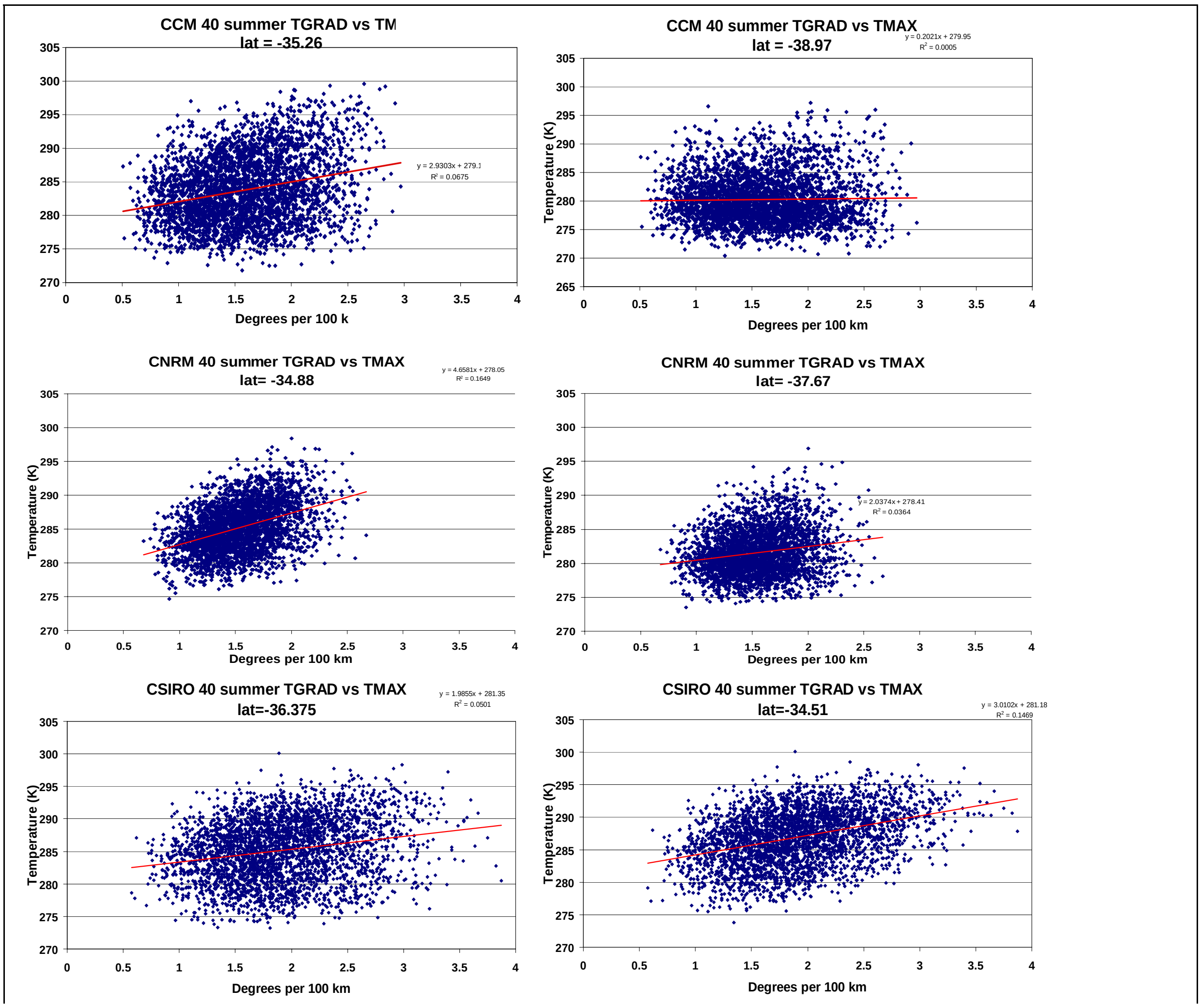

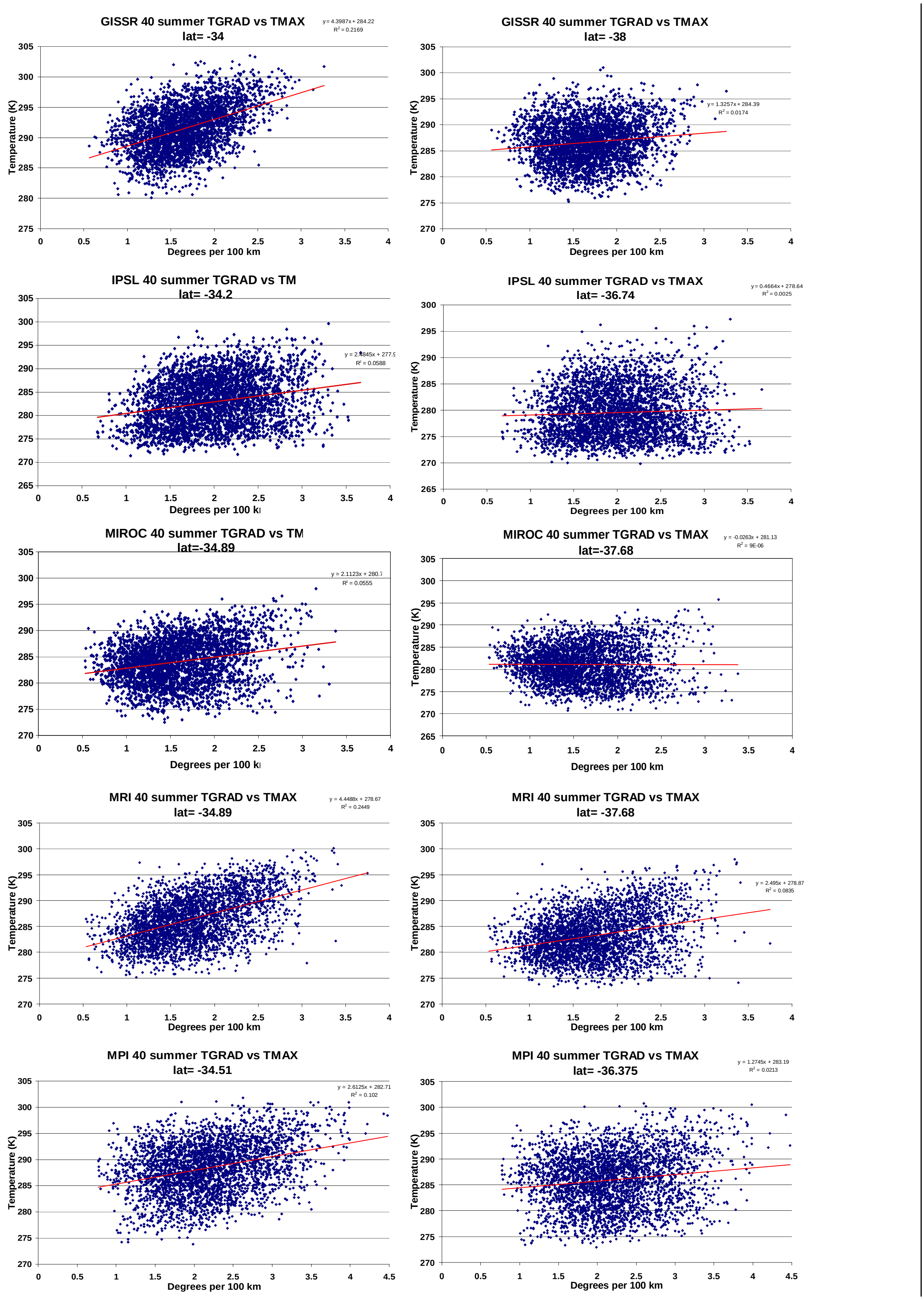

GISSR 40 summer TGRAD vs TMAX
lat= -34
y = 4.3987x + 284.22
R² = 0.2169
GISSR 40 summer TGRAD vs TMAX
lat= -38
y = 1.3257x + 284.39
R² = 0.0174
IPSL 40 summer TGRAD vs TM
lat= -34.2
y = 2.1845x + 277.9
R² = 0.0588
IPSL 40 summer TGRAD vs TMAX
lat= -36.74
y = 0.4664x + 278.64
R² = 0.0025
MIROC 40 summer TGRAD vs TM
lat=-34.89
y = 2.1123x + 280.7
R² = 0.0555
MIROC 40 summer TGRAD vs TMAX
lat=-37.68
y = -0.0263x + 281.13
R² = 9E-06
MRI 40 summer TGRAD vs TMAX
lat= -34.89
y = 4.4488x + 278.67
R² = 0.2449
MRI 40 summer TGRAD vs TMAX
lat= -37.68
y = 2.495x + 278.87
R² = 0.0835
MPI 40 summer TGRAD vs TMAX
lat= -34.51
y = 2.6125x + 282.71
R² = 0.102
MPI 40 summer TGRAD vs TMAX
lat= -36.375
y = 1.2745x + 283.19
R² = 0.0213
Temperature (K)
Degrees per 100 km

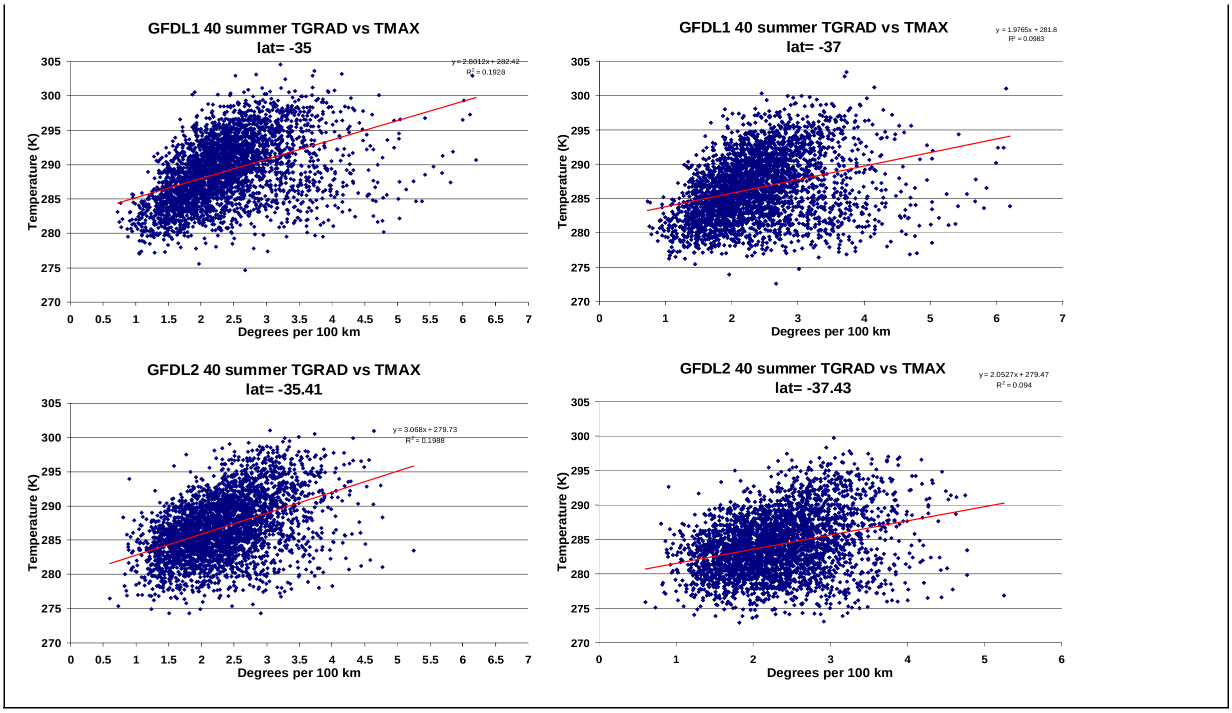
GFDL1 40 summer TGRAD vs TMAX
lat= -35
y = 2.8012x + 282.42
R2 = 0.1928
Temperature (K)
Degrees per 100 km
GFDL1 40 summer TGRAD vs TMAX
lat= -37
y = 1.9765x + 281.8
R2 = 0.0983
Temperature (K)
Degrees per 100 km
GFDL2 40 summer TGRAD vs TMAX
lat= -35.41
y = 3.068x + 279.73
R2 = 0.1988
Temperature (K)
Degrees per 100 km
GFDL2 40 summer TGRAD vs TMAX
lat= -37.43
y = 2.0527x + 279.47
R2 = 0.094
Temperature (K)
Degrees per 100 km

Appendix 4

Model	Latitudes	A	B	C	D	E	F
		Slope Tmax/ T_G	R^2	μ (T_G)	σ (T_G)	μ (Tmax)	σ (Tmax)
NNR	-35	3.735	0.214	1.648	0.314	286.85	23.68
	-37.5	2.749	0.099			288.90	21.01
ERA	-35	3.119	0.166	1.958	0.326	286.20	24.01
	-37.5	2.287	0.071			288.90	19.36
MPI	-34.51	2.613	0.102	2.182	0.356	288.41	23.85
	-36.38	1.275	0.022			285.97	27.19
MIROC	-34.89	2.112	0.056	1.598	0.218	284.09	17.58
	-37.68	-0.026	0.000			281.09	16.97
IPSL	-34.2	2.485	0.059	1.999	0.254	282.92	26.69
	-36.74	0.466	0.003			279.57	21.95
GFDL1	-35	2.801	0.193	2.393	0.556	289.12	22.62
	-37	1.977	0.098			286.53	22.09
CNRM	-34.88	4.658	0.165	1.539	0.097	285.20	12.70
	-37.67	2.037	0.036			281.55	11.09
GFDL2	-35.41	3.068	0.199	2.330	0.432	286.87	20.43
	-37.43	2.053	0.094			284.26	19.35
MRI	-34.89	4.449	0.245	1.751	0.256	286.46	20.69
	-37.68	2.495	0.084			283.24	19.07
CCM	-35.26	2.930	0.068	1.594	0.202	283.81	25.64
	-38.97	0.202	0.001			280.27	17.90
GISSR	-34	4.399	0.217	1.679	0.162	291.60	14.47
	-38	1.326	0.017			286.61	16.39
CSIRO	-34.51	3.010	0.147	1.902	0.279	286.91	17.23
	-36.375	1.986	0.050			285.13	21.97

Table 4.1

This table (4.1) summarises the slope and R^2 of the scatter plots (T_{max} versus T_G), as well as the mean (μ) and variance (σ) of the T_G and T_{max} distributions:

A. Slope of the linear regression of the scatter-plots displayed above, for each model at each investigated latitude

B. R^2 of the same scatter-plots

C. Mean of the T_G set

D. Variance of the T_G set

E. Mean of the T_{max} set

F. Variance of the T_{max} set

Models	Selected Latitudes	20th Century		A2					
		1964-2000		2046-2065			2081-2100		
		A	B	A	B	C	A	B	C
MPI	-34.51	32	0.86	15	0.75	-13.3	43	2.15	148.6
MIROC	-34.89	19	0.51	13	0.65	26.6	8	0.40	-22.1
IPSL	-34.2	12	0.32	35	1.75	439.6	76	3.80	1071.7
GFDL1	-35	12	0.32	18	0.90	177.5	9	0.45	38.8
CNRM	-37.67	15	0.41	20	1.00	146.7	47	2.35	479.7
GFDL2	-35.41	22	0.59	24	1.20	101.8	29	1.45	143.9
MRI	-37.68	23	0.62	18	0.90	44.8	22	1.10	77.0
CCM	-35.26	22	0.59	24	1.20	101.8	49	2.45	312.0
GISSR	-38	25	0.68	24	1.20	77.6	34	1.70	151.6
CSIRO	-34.51	27	0.73	11	0.55	-24.6	37	1.85	153.5

Models	Selected Latitudes	20th Century		B1					
		1964-2000		2046-2065			2081-2100		
		A	B	A	B	C	A	B	C
MPI	-34.51	32	0.86	25	1.25	44.5	25	1.25	44.5
MIROC	-34.89	19	0.51	11	0.55	7.1	6	0.30	-41.6
IPSL	-34.2	12	0.32	24	1.20	270.0	41	2.05	532.1
GFDL1	-35	12	0.32	9	0.45	38.8	11	0.55	69.6
CNRM	-37.67	15	0.41	21	1.05	159.0	25	1.25	208.3
GFDL2	-35.41	22	0.59	23	1.15	93.4	20	1.00	68.2
MRI	-37.68	23	0.62	16	0.80	28.7	15	0.75	20.7
CCM	-35.26	22	0.59	33	1.65	177.5	21	1.05	76.6
GISSR	-38	25	0.68	17	0.85	25.8	18	0.90	33.2
CSIRO	-34.51	27	0.73	33	1.65	126.1	29	1.45	98.7

Table 4.2

Table 4.2 summarizes the results for the 10 models and for the 2 scenarios, A2 and B1: column A correspond to the effective number of cases above thresholds during the period investigated, column B to the average number of cases per year, and column C to the percentage increase with respect to the 20th century.

The Centre for Australian Weather and Climate Research is a partnership between CSIRO and the Bureau of Meteorology.